Search for long-lived charginos based on a disappearing track signature in pp collisions at $\sqrt{s}$ = 13 TeV with the full Run-2 ATLAS data

重心系エネルギー 13TeV の陽子-陽子衝突における ATLAS Run-2 全データを用いた消失飛跡を残す長寿命チャージーノの探索

February, 2023

Toshiaki KAJI
加地　俊瑛

Search for long-lived charginos based on a disappearing track signature in pp collisions at $\sqrt{s}$ = 13 TeV with the full Run-2 ATLAS data

重心系エネルギー 13TeV の陽子-陽子衝突における ATLAS Run-2 全データを用いた消失飛跡を残す長寿命チャージーノの探索

February, 2023

Waseda University
Graduate School of Advanced Science and Engineering

Department of Pure and Applied Physics
Research on Experimental Particle Physics

Toshiaki KAJI
加地　俊瑛

Abstract

Supersymmetry (SUSY) is one of the most attractive concepts of the standard model extension. The lightest SUSY particle (LSP) is a good candidate for dark matter. The pure-wino or -higgsino LSP scenario is particularly motivated well by the relic density measurement and the pMSSM scan result. Under these scenarios, the masses of the lightest chargino and neutralino highly degenerate, and the chargino can have a long lifetime.

This thesis presents the search results for long-lived charginos using a disappearing track comprising four innermost pixel layer hits in pp collisions at $\sqrt{s}$ = 13 TeV with the full Run-2 ATLAS data. In this analysis, the production of the $\tilde{\chi}_1^{\pm}$-$\tilde{\chi}_1^0$ or $\tilde{\chi}_1^+$-$\tilde{\chi}_1^-$ pair with an initial state radiation jet (EWK channel) and the production of a gluino pair with cascade decay into the chargino (strong channel) are considered as the signal production processes. The search is performed for the pure-wino and -higgsino LSP scenarios in the electroweak channel and the pure-wino LSP scenario in the strong channel. Unfortunately, no significant excess existed above the background predictions in both channels; hence, new exclusion limits at 95% CL were calculated for each signal model. The observed limit in the EWK channel excluded chargino masses up to 660 GeV/c^2 on the theoretical prediction line for the pure-wino LSP scenario and 210 GeV/c^2 for the pure-higgsino LSP scenario. The maximum reach in the strong channel was 1.4 (1.8 TeV/c^2) and 2.1 (2.18 TeV/c^2) TeV/c^2 on the chargino and gluino masses, respectively, with $\tau_{\tilde{\chi}_1^{\pm}}$ = 0.2 ns (1.0 ns).

The search results are compared to those of other analyses and discussed. Several ideas for improving sensitivities for future disappearing track searches are also introduced. The expected sensitivity using various track lengths is shown. Finally, assuming that the long-lived chargino is already discovered, the chargino mass reconstruction method and its accuracy are explained.

Contents

1 Introduction

What is the universe made of, and how does it work? Answering these questions is an essential task for elementary particle physics. The higgs boson was discovered on 4 July 2012, and all elementary particles in the Standard Model (SM) are finally found and the model is completed. However, it is known that the SM is not perfect because it can not explain some existing phenomena like gravity and dark matter. Therefore, a new framework beyond the Standard Model (BSM) is necessary, and the discovery of the BSM particles is an essential key to constructing the framework.

A supersymmetric extension of the SM is one of the most attractive theories for BSM physics. Supersymmetry (SUSY) is a symmetry between fermions and bosons. It can solve the hierarchy problem, and it is also known that the gauge coupling constants are unified at the grand unification theory (GUT) scale with SUSY. Furthermore, the lightest SUSY particle (LSP) can be a candidate for a dark matter particle. From the observation of the cosmic microwave background (CMB), the relic density of dark matter has been measured as $\Omega_{\mathrm{DM}}h^2 = 0.120$ [1]. According to the measured relic density, phase spaces of the pure-bino LSP scenario are largely excluded, while it is predicted that the dark matter mass is below 3 TeV[1] for the pure-wino LSP scenario or below 1 TeV for the pure-higgsino LSP scenario.

The Large Hadron Collider (LHC) is the world's largest accelerator located at CERN. It is operated at the center-of-mass energy of 13 TeV in Run-2 (2015-2018). ATLAS experiment is one of the four major experiments at LHC for precise measurement of the SM and discovery of new physics at TeV scale. Various new particle searches were performed at the ATLAS experiment, however, there is yet no sign of new particle after the discovery of the higgs boson. There might be some possible reasons for the absence of the new signal. One possibility is a lack of center-of-mass energy or statistics of physics data. It means further effort for the accelerator is required. The other one is somehow overlooked or uncovered yet due to difficulty in analysis. In general SUSY particles searches, such as gluinos or squarks so-called strong SUSY, analysis is performed by using high-p_{T} multi-jets and large missing E_{T} because these processes include multiple quarks and LSPs in the final state. Mass limits for gluinos and squarks have reached around 2 TeV by inclusive searches. In contrast, a search for winos or higgsinos so-called electroweak (EWK) SUSY is more difficult because their production cross-section is relatively small and there is no hard object in the final state. Therefore, a search for EWK SUSY is performed by using leptons and missing E_{T} in general. However, if the LSP is the pure-wino or the pure-higgsino, masses of the lightest chargino and neutralino are highly degenerated, and then leptons are suppressed as decay products. The mass difference and the lifetime are typically about 160 MeV and 0.2 ns for the pure-wino scenario and about 300 MeV and 0.04 ns for the pure-higgsino scenario. In these cases,

[1] In this thesis, the speed of light $c = 1$ is used. Therefore, both a unit of mass [eV/c^2] and a unit of momentum [eV/c] are expressed as [eV].

chargino decays after a few cm flights to neutralino and charged pion. The neutralino is observed as a missing E_{T} and the pion is also unreconstructed due to a large radius production vertex and very low momentum, the only reconstructed observable in this signal is so-called "disappearing track" due to the chargino. Although the standard track reconstruction algorithm in the ATLAS assumes a long track (> 1 m), if the short track of charginos can be reconstructed, an important compressed mass region of EWK SUSY becomes accessible. In this thesis, the result of the search for long-lived charginos by using a disappearing track consisting of four innermost pixel layer hits in pp collisions at $\sqrt{s}$ = 13 TeV with the full Run-2 ATLAS data is reported.

In addition to this introductory chapter, this thesis consists of the following chapters. Chapter 2 describes a brief overview of SM and SUSY and then summarizes the constraint on SUSY particles from collider experiments. Finally, the motivation for disappearing track analysis and its phenomena are described. Chapter 3 introduces the LHC and the ATLAS experiment and then describes each detector component. Chapter 4 summarizes definitions of physics objects used in this analysis. In the ATLAS experiment, standard tracking reconstructs tracks typically longer than 1 m. Therefore, short track reconstruction by using only leftover hits after standard tracking with loosening requirements is developed for the disappearing track analysis. Pixel-track is a key of this analysis and its features and performances are summarized in Chapter 5. Chapter 6 is the main part of this thesis and the search for long-lived charginos by using the disappearing track signature with the full Run-2 data is summarized. Chapter 7 discusses the results of this analysis and compares them to other analysis results. Then new ideas for improvement of the sensitivity are introduced for future search. For the improvement of signal acceptance, the search with various track lengths should be useful. As a further background reduction, improvement of momentum resolution by using vertex information and use of $\mathrm{d}E/\mathrm{d}x$ information are considered. Furthermore, measurement of the dark matter mass becomes important after the discovery, so chargino mass reconstruction with two disappearing track signatures is also considered in high statistics environment. Chapter 8 summarizes the contents and conclusions of this thesis.

2 Theoretical Overview

This chapter starts with a brief overview of SM and then introduces some SUSY models as a candidate for the BSM framework. Dark matter plays an important role in the BSM framework, so the results of current dark matter searches are summarized. Finally, the disappearing track signature which is motivated by the pure-wino LSP or pure-higgsino LSP scenario is introduced.

2.1 Problems in The Standard Model

The SM is the most basic theoretical framework in the current elementary particle physics. It explains almost all the experimental results and predicts many phenomena. Figure 1 shows all elementary particle species in the SM. With the discovery of the higgs boson, all particles appearing in the SM were found.

However, it is known that the SM is not a perfect theory because the SM does not have solutions to the following questions. Despite the existence of dark matter that has been proved by observation of rotational speeds of galaxies, or separation of ordinary matter and dark matter clouds after a collision of two galaxies, and so on, there is no candidate for dark matter in the SM. Baryon density has been measured by Planck Collaboration[1] as 4.9 %[3], so the SM can explain only a small fraction of the

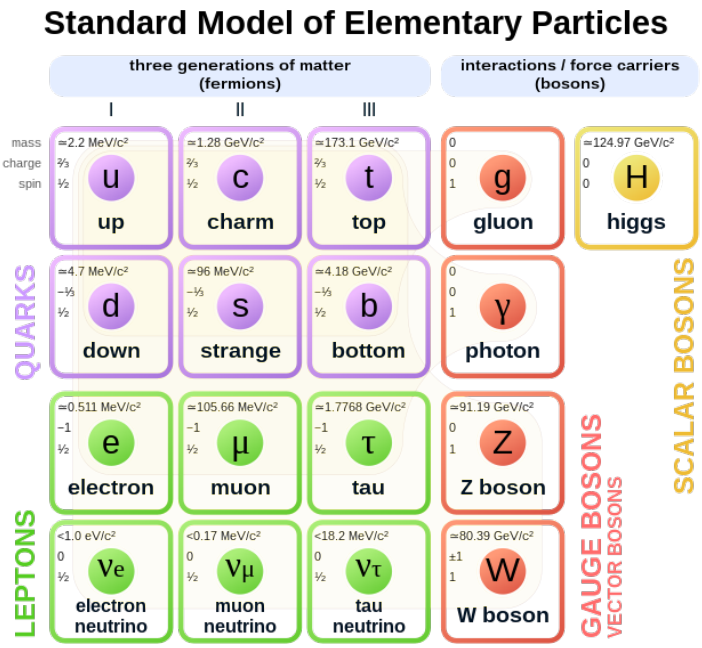

Figure 1: Elementary particles in the Standard Model [2]

universe. The current universe is dominated by matter, not antimatter, but there is no mechanism to explain the current matter-antimatter asymmetry in the SM. Gravity is well known in classical physics, but it is not included in the SM. The expansion velocity of the universe is increasing, but the SM can not explain this acceleration. This vacuum energy which may explain the accelerating expansion of the universe is so-called "dark energy". While neutrinos are massless particles in the SM, neutrino oscillation experiments indicate neutrinos have mass. However, it is not easy to explain the observational result within the framework of the SM.

These facts are only part of aspects in the SM. Therefore, a new framework taken place beyond the SM is necessary. The next new particle to be discovered should be a BSM particle and it will open a new paradigm.

2.2 Hierarchy Problem and Supersymmetry

Supersymmetry (SUSY) is a concept introduced to solve multiple problems, especially the hierarchy problem, in the SM. Figure 2(a) shows the Feynman diagram of one-loop correction to the higgs mass from a fermion, such as quarks or leptons. The correction from the fermion is given by

$$\Delta m_{H,f}^2 \simeq -\frac{|\lambda_f|^2}{8\pi^2}\Lambda^2 + O(\ln \Lambda), \tag{1}$$

where λ_f is the Yukawa coupling and Λ is the cut-off energy scale at which the SM becomes not valid. For quarks, Eq.(1) is multiplied by 3 to account for the color charge degree of freedom. The largest correction comes from the top quark because the Yukawa coupling is proportional to the fermion mass and the top quark is the heaviest fermion in the SM. The quantum corrections to the higgs boson mass are quadratically divergent with Λ. Hence, at the Planck scale $\Lambda \sim 10^{19}$ GeV, an extreme fine-tuning would be necessary between the observed mass of 125 GeV and the correction at an order of 10^{36} $(\text{GeV})^2$. This fact is un-natural. Furthermore, this problem is specific to scalar bosons. The quantum corrections to fermion and gauge boson masses are suppressed by the particle masses themselves and do not have the quadratic divergence term. However, since the quarks, leptons, and the electroweak gauge bosons obtain masses from the higgs field, it implies all non-massless particles in the SM are quadratically sensitive to the Planck scale. This problem is called the hierarchy problem.

One of the simplest solutions is to remove the quadratic divergence term. If there is a complex scalar particle coupled to the higgs, it also has the loop as shown in Figure 2(b) and contributes the correction with the opposite sign as

$$\Delta m_{H,S}^2 \simeq +\frac{\lambda_S}{16\pi^2}\Lambda^2 + O(\ln \Lambda). \tag{2}$$

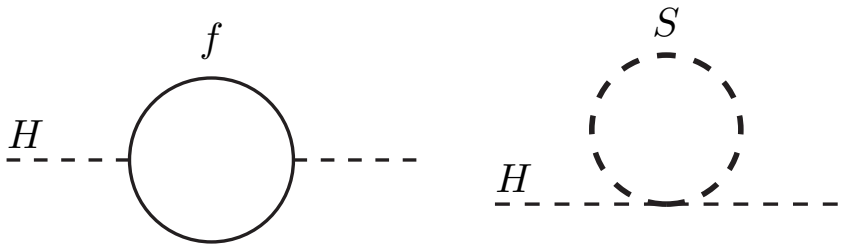

(a) Fermion loop (b) Scalar loop

Figure 2: Feynman diagrams of 1-loop correction to the higgs mass

So if there are two complex scalars for every fermion in the SM and $\lambda_S = \lambda_f^2$, the quadratic terms automatically cancel out. This is the main motivation to introduce SUSY which is symmetry relating between fermions and bosons. An operator that transforms between fermionic and bosonic states is also introduced as follows :

$$Q\,|\text{Fermion}\rangle = |\text{Boson}\rangle, \quad Q\,|\text{Boson}\rangle = |\text{Fermion}\rangle, \tag{3}$$

where Q is complex and anticommuting Weyl spinor. Weyl spinors Q_α ($\alpha = 1, 2$) are left-handed while their hermitian conjugates $Q^\dagger_{\dot{\alpha}}$ ($\dot{\alpha} = 1, 2$) are right-handed. The Q_α and $Q^\dagger_{\dot{\alpha}}$ must satisfy the following relation :

$$\{Q_\alpha, Q^\dagger_{\dot{\alpha}}\} = -2\sigma^\mu_{\alpha\dot{\alpha}} P_\mu, \tag{4}$$

where $\sigma^\mu_{\alpha\dot{\alpha}} = (1, \sigma^i)$ and σ^i are the Pauli matrices, and P_μ is the four-momentum generator of spacetime translations [4]. This relation implies the applying SUSY operator twice is equivalent to a spacetime translation. SUSY merges spacetime and internal symmetries at the level of algebra.

2.3 Minimal Supersymmetric Standard Model

Theoretical models including SUSY have a vast phase space because SUSY itself is just a concept and does not indicate a specific scenario. In this sub-section, the Minimal Supersymmetric Standard Model (MSSM) is introduced as a minimal extension model of the SM. The MSSM is based on the gauge symmetry $\mathrm{SU(3)_C \times SU(2)_L \times U(1)_Y}$, where C stands for color, L stands for the left-handed chiral group, and Y stands for hypercharge as in the SM. SUSY partners of gauge bosons are gluino $\tilde{g}$, wino $\tilde{W}$, and bino $\tilde{B}$, these are collectively called gauginos. There are also SUSY partners of quarks and leptons called squarks and sleptons, respectively. As a minimum extension, two higgs doublets are required for

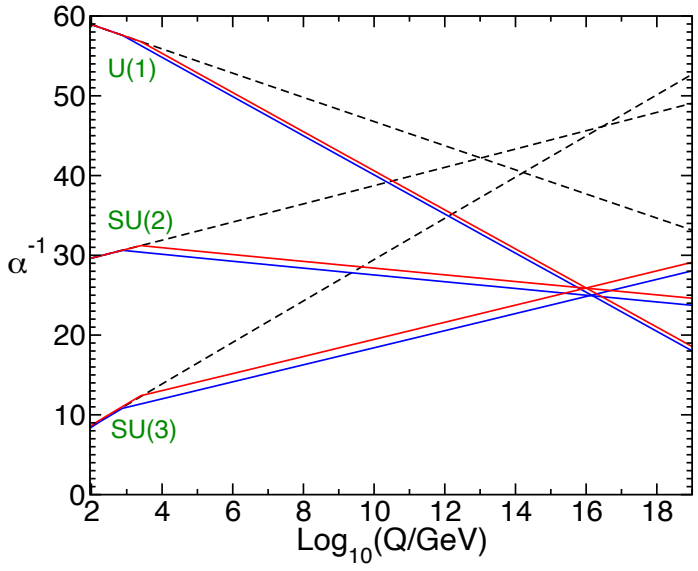

Figure 3: Two-loop renormalization group evolution of the inverse gauge couplings in the SM (dashed lines) and the MSSM (solid lines) with the masses of the SUSY particles between 750 GeV (blue color) and 2.5 TeV (red color) [4]

the cancellation of chiral anomalies :

$$H_u = \begin{pmatrix} H_u^+ \\ H_u^0 \end{pmatrix}, \quad H_d = \begin{pmatrix} H_d^0 \\ H_d^- \end{pmatrix} \tag{5}$$

where u and d stand for up and down, and each provides the masses for up-type fermions or down-type fermions respectively. So the corresponding fermions are called higgsinos. The higgsinos, winos, and bino are mixed to give the mass eigenstates called the charginos $\tilde{\chi}^{\pm}_{1,2}$ and neutralinos $\tilde{\chi}^0_{1,2,3,4}$, where the numbers are in ascending order of the masses. To enforce lepton and baryon number conservation, the new quantum number, the R-parity is defined as :

$$R = (-1)^{3(B-L)+2S} \tag{6}$$

where L and B are the lepton and baryon numbers, and S is the spin of the particle. All SM particles have $R = +1$, while all SUSY particles have $R = -1$. Under the conservation of the R-parity, the SUSY particles are always produced in pairs and their decay products include an odd number of SUSY particles. Therefore, the lightest SUSY particle (LSP) is absolutely stable and a good candidate for dark matter. Furthermore, as shown in Figure 3, it is known that the gauge couplings of strong, weak, and electromagnetic interaction are unified at the GUT scale of 1.5×10^{16} GeV in the MSSM. These features explain why SUSY scenarios are attractive.

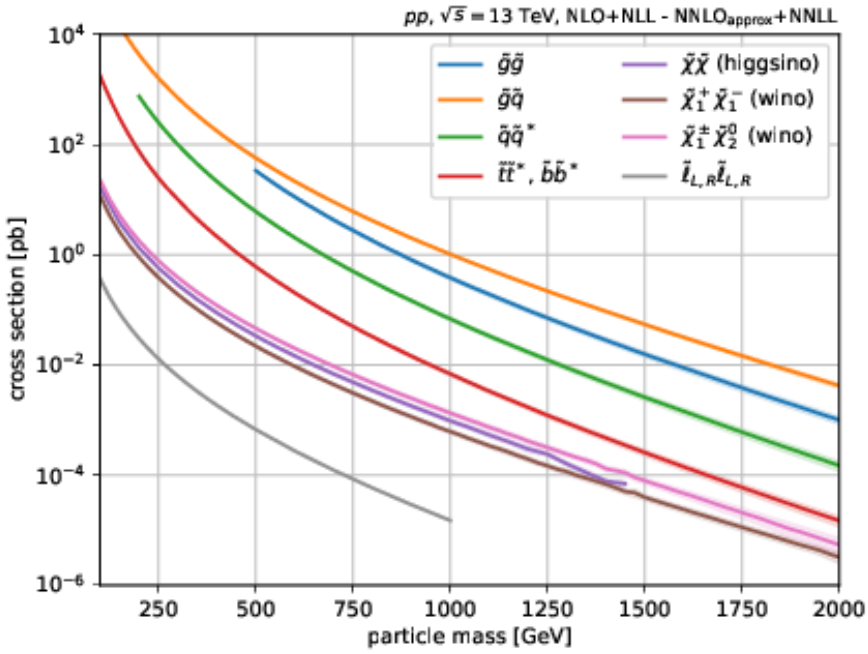

Figure 4: Production cross-section of SUSY particles at $\sqrt{s}$ = 13TeV [5] [6] [7] [8] [9] [10] [11] [12]

2.4 Constraints on SUSY

While various SUSY searches had been performed in collider experiments, especially the ATLAS and the CMS experiments for the recent, there is no evidence for the signal. Figure 4 shows the production cross-section of SUSY particles at the LHC. Gluinos and squarks like stops (SUSY partners of top quarks) so-called strong SUSY have higher cross-sections than wino, higgsino, and sleptons, so-called electroweak (EWK) SUSY. A search for strong SUSY is performed by using high-p_{T} multi-jets and large missing E_{T} because these processes include multiple quarks and LSPs in the final state. Figure 5 and Figure 6 show summary plots of the search for gluino-pair and stop-pair production processes, respectively at the ATLAS. A maximum excluded mass reaches around 2.2 TeV for gluino and 1.2 TeV for stop with the lightest neutralino mass of $O(100)$GeV.

In contrast, a search for EWK SUSY is performed by using leptons and missing E_{T} in general with an assumption of the bino-LSP/wino-NLSP scenario. Figure 7 shows the summary plot of the EWK gaugino search at the ATLAS in March 2022. The production cross-section is for pure wino. A maximum excluded mass reach is relatively lower than strong SUSY particles, especially for the LSP mass and in the compressed mass spectra region which is the upper-left region in the figure. The mass reach is only about 400 GeV for the LSP mass and about 250 GeV for the compressed region.

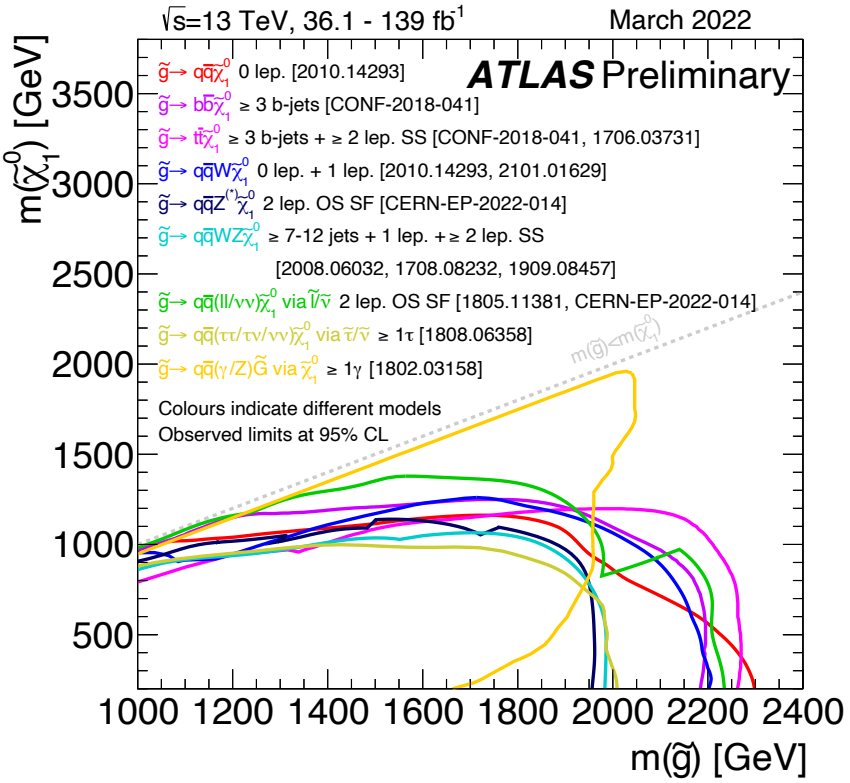

Figure 5: Summary plots of the strong SUSY search in gluino-pair production at the ATLAS. (March 2022) [13]

A search for the wino-LSP or higgsino-LSP scenario needs special treatment because the masses of the lightest chargino and the lightest neutralino are expected to be highly degenerated, resulting in suppression of leptons in the decay products. In addition to the low production cross-section, absence of hard objects in the final state makes it difficult to catch these signals. However, despite the difficulty, these compressed LSP-NLSP mass scenarios are highly motivated.

Figure 8(a) shows the result of the pMSSM scan and it indicates which type of LSP is favored as a function of mass. The pMSSM stands for the phenomenological MSSM, and it assumes several experimental constraints to reduce the number of parameters in MSSM to 19. In the pMSSM, there is no CP violation in the sparticle sector, there is no flavor changing neutral current, and the first two generations of sfermions degenerate in mass. The remaining 19 parameters are listed in Table 1. In the pMSSM scan, these parameters are randomly scanned to reveal uncovered phase spaces. The measured relic density from the Planck 2015 is overlayed in Figure 8(a), and it indicates the dark matter mass around 1.3 TeV for the higgsino-LSP and around 2.7 TeV for the wino-LSP scenario. Figure 8(b) shows the mass difference between the LSP and the NLSP with the constraint of the upper and lower relic density bounds. From the point of the relic density, the bino-LSP scenario tends to have large relic

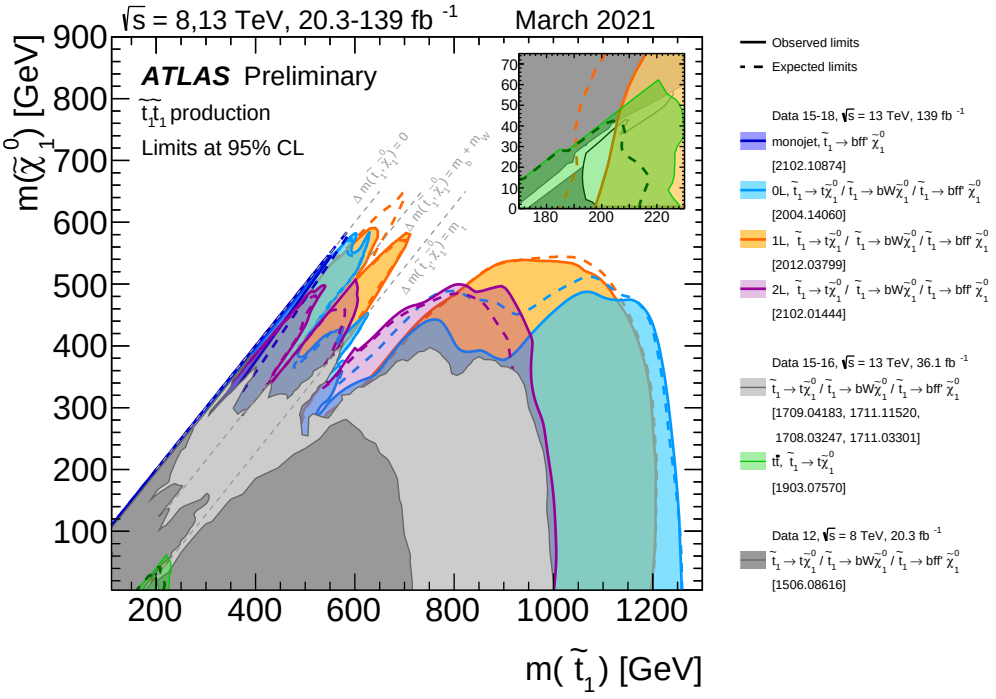

Figure 6: Summary plots of the strong SUSY search in stop-pair production at the ATLAS. (March 2021) [13]

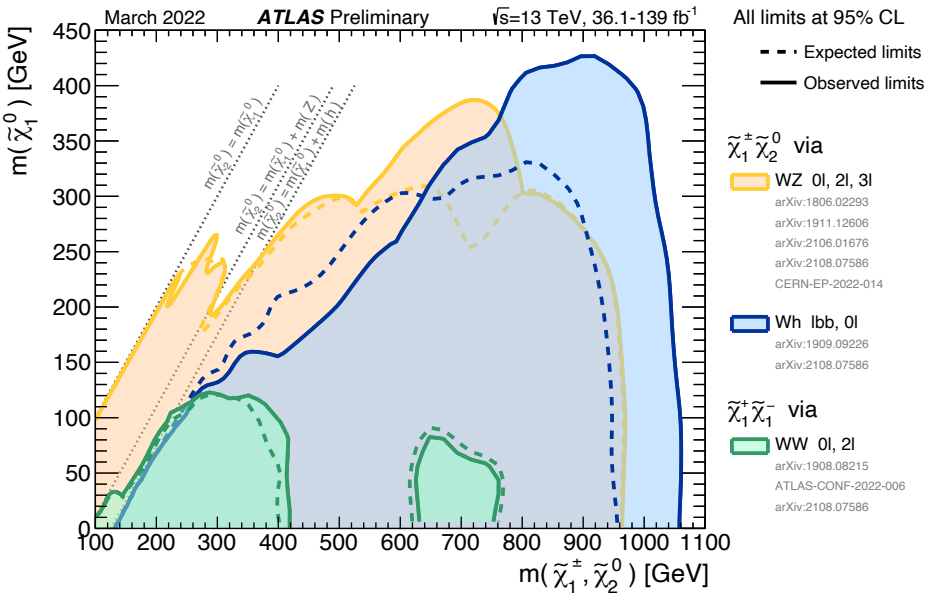

Figure 7: Summary plot of the EWK gaugino search at the ATLAS. (March 2022) [13]

Table 1: Parameters of the pMSSM scan

Parameter	Description
$\tan\beta$	The ratio of two higgs vacuum expectation values
μ	Higgsino mass parameter
M_A	Pseudoscalar higgs boson mass
M_1, M_2, M_3	Mass parameters of bino, wino, and gluino
A_t, A_b, A_τ	Trilinear couplings of the top, bottom, and τ
$M_{\tilde{q}_{1L}}$, $M_{\tilde{u}_R}$, $M_{\tilde{d}_R}$, $M_{\tilde{e}_L}$, $M_{\tilde{e}_R}$	Masses of the first/second generation sfermions
$M_{\tilde{q}_{3L}}$, $M_{\tilde{t}_R}$, $M_{\tilde{b}_R}$, $M_{\tilde{\tau}_L}$, $M_{\tilde{\tau}_R}$	Masses of the third generation sfermions

densities, and the constraint is satisfied in a special case, so a strong co-annihilation mechanism is necessary. On the other hand, the wino-LSP or the higgsino-LSP scenarios naturally satisfy the upper limit of the relic density constraint. Furthermore, most accepted points require small mass splitting. Therefore a search for the compressed LSP-NLSP mass spectra scenario is important.

2.5 Disappearing Track

Anomaly mediated supersymmetry breaking (AMSB) model is well known as a representative model of the wino-LSP scenario. If SUSY exists, it must be broken at low energy scale because no SUSY particles have been observed at the same mass scale of the SM. The AMSB model induces the soft

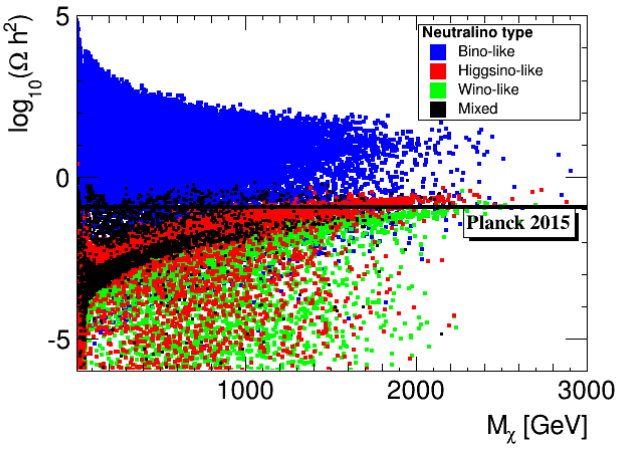

(a) Relic density vs the lightest neutralino mass

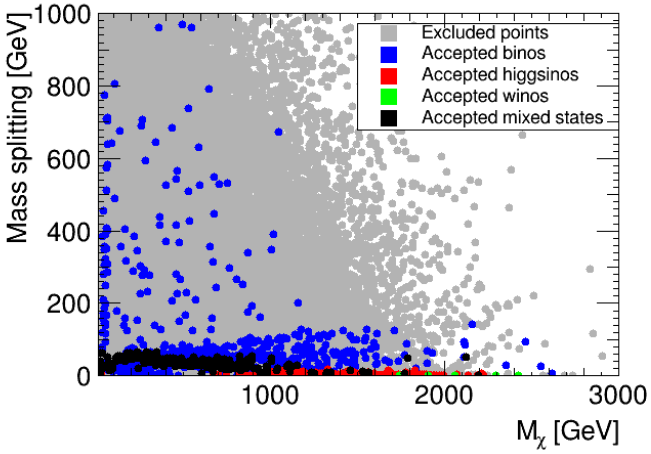

(b) Mass splitting vs the lightest neutralino mass with the constraint of the relic density measured by the Planck 2015

Figure 8: Results of the pMSSM scan. [14]

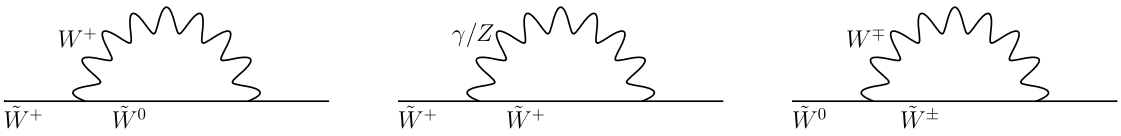

Figure 9: One-loop diagrams contributing the masses of wino-like chargino and neutralino

mass parameters for the observable sector from the superconformal anomaly. However, in the simplest AMSB model, the sleptons have negative squared masses. To avoid tachyonic sleptons, a square of a common scalar mass parameter m_0^2 is added to all squared scalar masses. This scenario is called the minimal AMSB (mAMSB) and is characterized by four parameters: the gravitino mass ($m_{3/2}$), the common scalar mass (m_0), the $\tan\beta$, and the sign of the higgsino mass term sign(μ). The gaugino masses are proportional to the $m_{3/2}$ as :

$$M_i = \frac{b_i g_i^2}{16\pi^2} m_{3/2}, \tag{7}$$

where g_i is the coupling constant and b_i is the beta function in the MSSM for the corresponding gauge group U(1), SU(2), and SU(3). The coefficients are (b_1, b_2, b_3) = ($\frac{33}{5}$, 1, -3), and the ratios of the gaugino masses are (M_1 : M_2 : M_3) = (3:1:7) at NLO. In this thesis, the wino is assumed as LSP in the mAMSB model because the wino is LSP over most of the MSSM parameter spaces. The tree-level mass splitting between the lightest chargino and the lightest neutralino with $|\mu| \gg M_1, M_2, m_W$ is highly suppressed, while the dominant contribution comes from the one-loop correction involving EWK gauge bosons as shown in Figure 9. Figure 10 shows the mass splitting at the two-loop level as a function

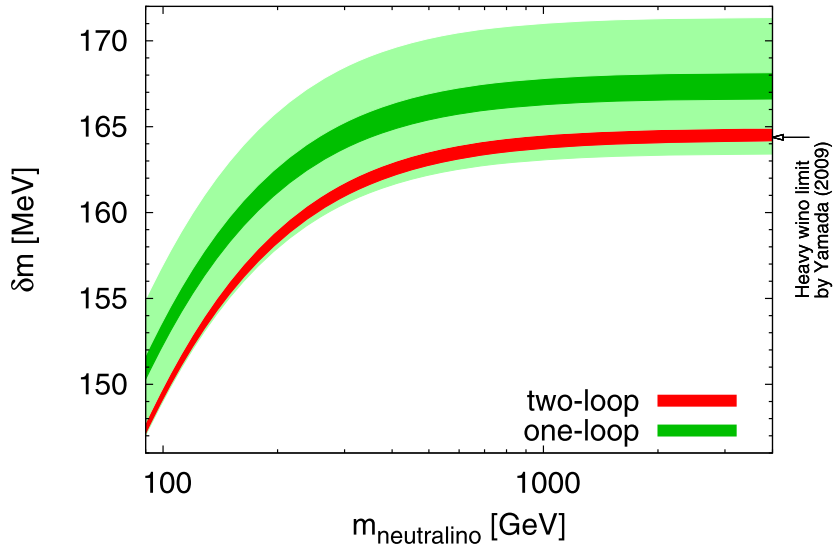

Figure 10: Mass splitting of wino-like chargino and neutralino at two-loop level [15]

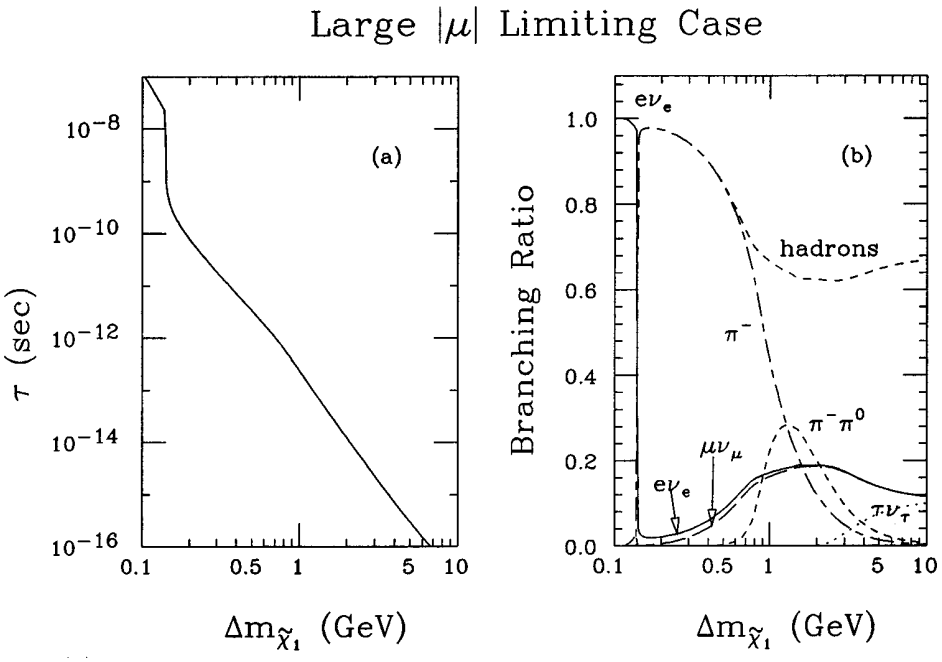

Figure 11: Lifetime and branching ratio of the lightest chargino [16]

of the LSP mass, and it is almost flat around 160 MeV. It is expected that the mass difference becomes the maximum at 164 MeV. The phenomenology of the chargino with compressed mass spectra is summarized in Figure 11(a) and Figure 11(b), a lifetime and branching ratio of the lightest chargino as a function of $\Delta m_{\tilde{\chi}_1}(= m_{\tilde{\chi}_1^\pm} - m_{\tilde{\chi}_1^0})$ respectively. At the $\Delta m_{\tilde{\chi}_1} = 160$ MeV, the chargino has a considerably long lifetime ($\tau_{\tilde{\chi}_1^\pm} \sim 0.2$ns) and the dominant decay process is $\tilde{\chi}_1^\pm \to \tilde{\chi}_1^0 \pi^\pm$. The decay width into the charged pion is given as :

$$\Gamma\left(\tilde{\chi}_1^\pm \to \tilde{\chi}_1^0 \pi^\pm\right) = \frac{2G_F^2}{\pi} \cos^2\theta_c f_\pi^2 \Delta m_{\tilde{\chi}_1}^3 \left(1 - \frac{m_\pi^2}{\Delta m_{\tilde{\chi}_1}^2}\right)^{\frac{1}{2}}, \tag{8}$$

where G_F, θ_c, f_π and m_π are the Fermi coupling constant, the Cabibbo angle, the pion decay constant ($\simeq 130$ MeV) and the pion mass respectively. The corresponding decay lifetime in terms of the $c\tau$-value is

$$c\tau[\text{mm}] \sim 31 \times \left[\left(\frac{\Delta m_{\tilde{\chi}_1}}{164\,\text{MeV}}\right)^3 \sqrt{1 - \frac{m_\pi^2}{\Delta m_{\tilde{\chi}_1}^2}}\right]^{-1}. \tag{9}$$

For example, in the case of $\Delta m_{\tilde{\chi}_1} = 164$ MeV and $m_\pi = 140$ MeV, the $c\tau$ becomes about 60 mm. As a result, chargino decays after a few cm flights to neutralino and charged pion so that a fraction of charginos leave hits on tracking detectors at collider experiments. If these short tracks of the charginos can be detected, an important compressed mass region of EWK SUSY becomes accessible. The neutralino is un-detectable and the pion is also un-reconstructed due to a large radius production vertex and very

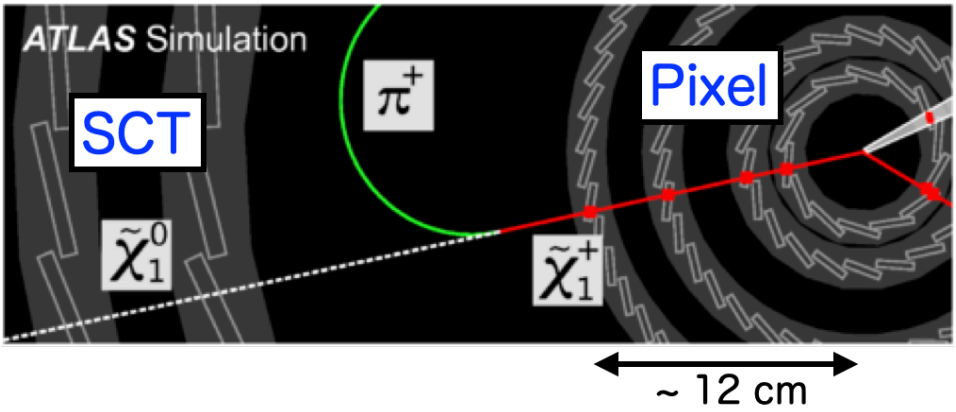

Figure 12: Disappearing track signature at the ATLAS detector [17]

low momentum, so the short track of the chargino seems to be disappeared. Hence, this signature is called a disappearing track or kinked track. Figure 12 shows a typical disappearing track signature in the ATLAS experiment.

The higgsino-LSP scenario is also motivated by naturalness. Because SUSY is introduced to solve the hierarchy problem, the masses of the SUSY particles with the closest ties to the higgs field should be small. This principle is called naturalness. In natural SUSY, the higgsinos should not be too heavy because their mass is controlled by the parameter μ. The stop and gluino also should not be too heavy because these are contributing to $m_{H_u}^2$ at one-loop and two-loop order respectively. The properties of charginos and neutralinos in the higgsino-LSP scenario are almost the same as in the wino-LSP scenario

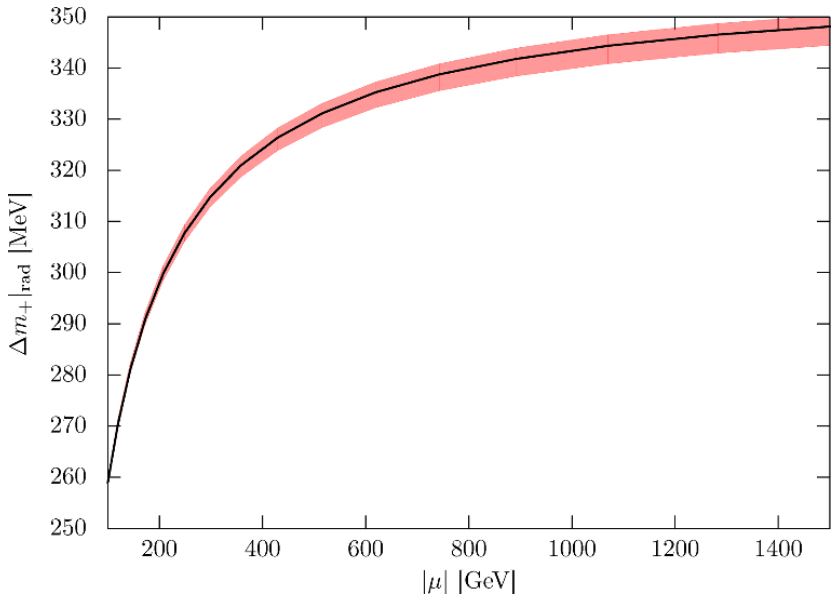

Figure 13: Mass splitting of higgsino-like chargino and neutralino at one-loop level [18]

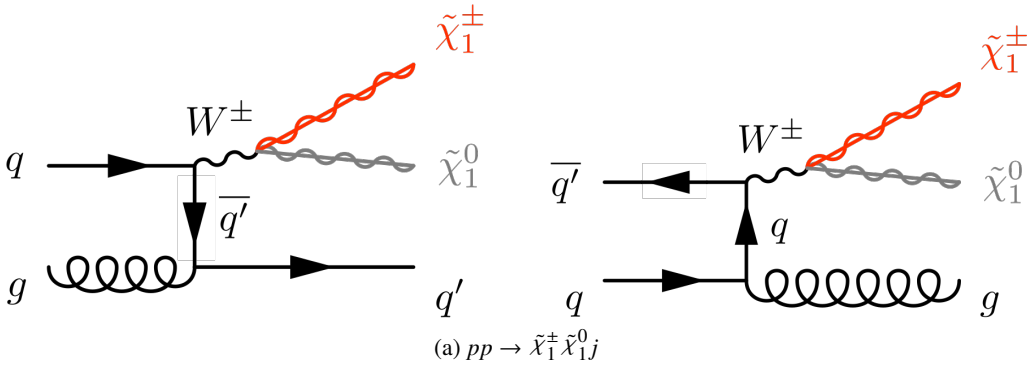

(a) $pp \to \tilde{\chi}_1^{\pm}\tilde{\chi}_1^0 j$

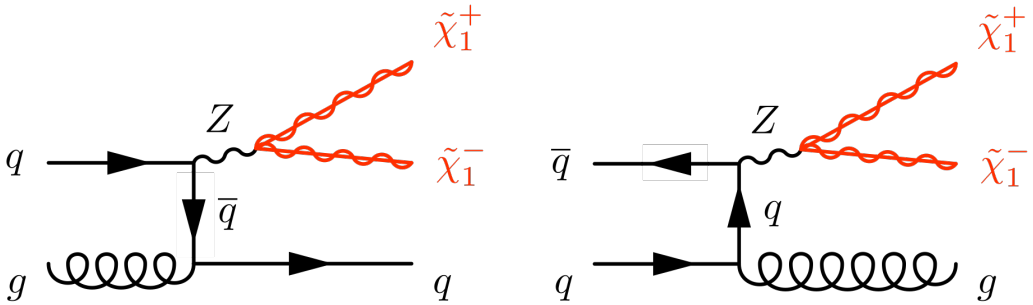

(b) $pp \to \tilde{\chi}_1^{+}\tilde{\chi}_1^{-} j$

Figure 14: Feynman diagrams of direct EWK production processes.

except for the mass difference and the lifetime.

Figure 13 shows the mass difference as a function of the higgsino mass parameter $|\mu|$. The mass difference is around 340 MeV, and it is slightly higher than the wino-LSP scenario. Therefore, the lifetime of the chargino is shorter than the wino-LSP scenario as follows :

$$c\tau[\text{mm}] \sim 7 \times \left[\left(\frac{\Delta m_{\tilde{\chi}_1}}{340\,\text{MeV}} \right)^3 \sqrt{1 - \frac{m_\pi^2}{\Delta m_{\tilde{\chi}_1}^2}} \right]^{-1}, \tag{10}$$

Due to the short path length, detection of the higgsino-like chargino is much more difficult.

Figure 14 shows the production processes of the $\tilde{\chi}_1^{\pm} - \tilde{\chi}_1^0$ or $\tilde{\chi}_1^{+} - \tilde{\chi}_1^{-}$ pair. These are produced directly via electroweak boson. In this analysis, Initial State Radiation (ISR) jet is required to trigger events by missing E_{T}. Without this jet, missing E_{T} from the $\tilde{\chi}_1^0$ is balanced and the signal events can not be triggered.

Gluino pair production with cascade decay into the chargino is also considered for the wino-LSP scenario because the production cross-section is larger than direct EWK production. Figure 15 shows Feynman diagrams. In this production, multiple quarks are included in a final state, so it is relatively easy to trigger events.

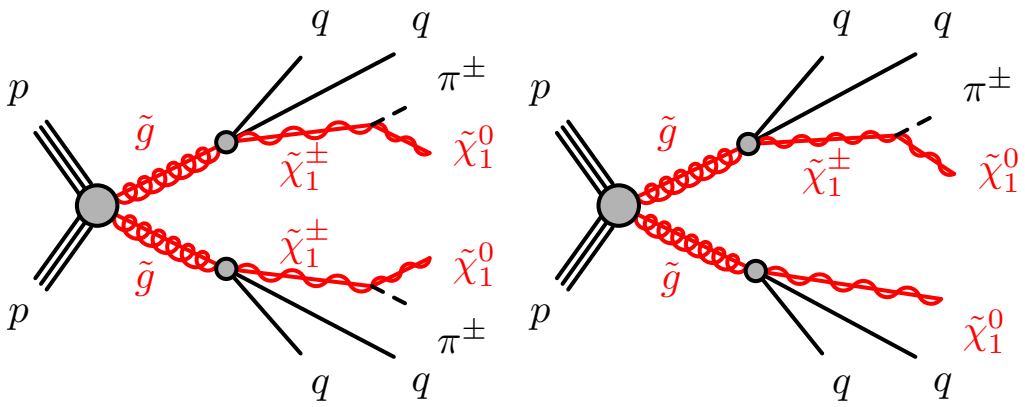

(a) $pp \to \tilde{g}\tilde{g} \to qqqq\tilde{\chi}_1^{\pm}\tilde{\chi}_1^{\pm}$ (b) $pp \to \tilde{g}\tilde{g} \to qqqq\tilde{\chi}_1^{\pm}\tilde{\chi}_1^0$

Figure 15: Feynman diagrams of gluino pair production

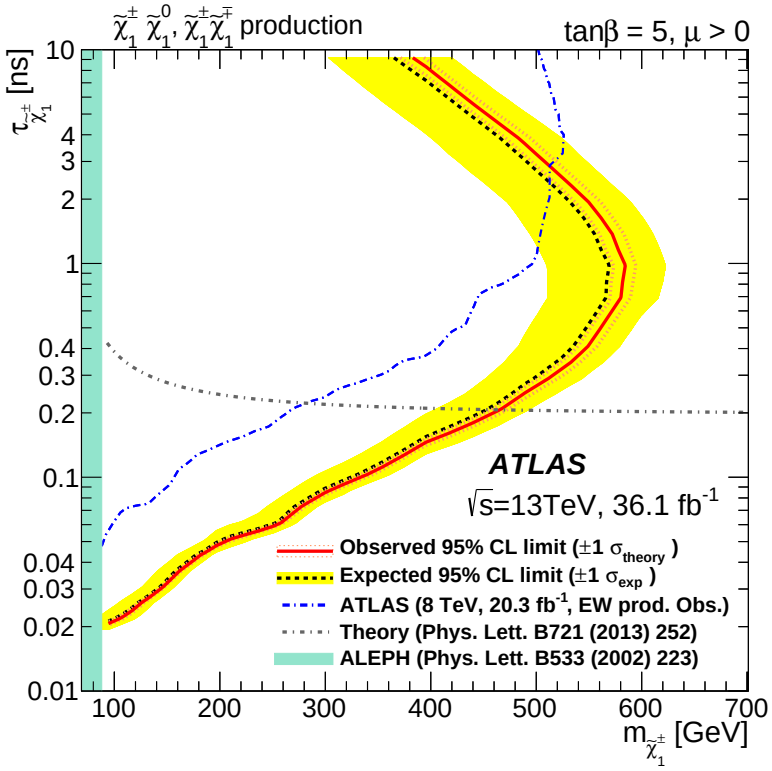

Figure 16: The constraint on the $\tau_{\tilde{\chi}_1^{\pm}}$–$m_{\tilde{\chi}_1^{\pm}}$ space from the previous disappearing track search at the ATLAS [17]. The black dashed line shows the expected limits at 95% CL, with the surrounding yellow shaded bands indicating the 1σ excursions due to experimental uncertainties. Observed limits are indicated by red solid bold contour representing the nominal limit and the dotted lines on either side are obtained by varying the cross-section by the theoretical scale and PDF uncertainties.

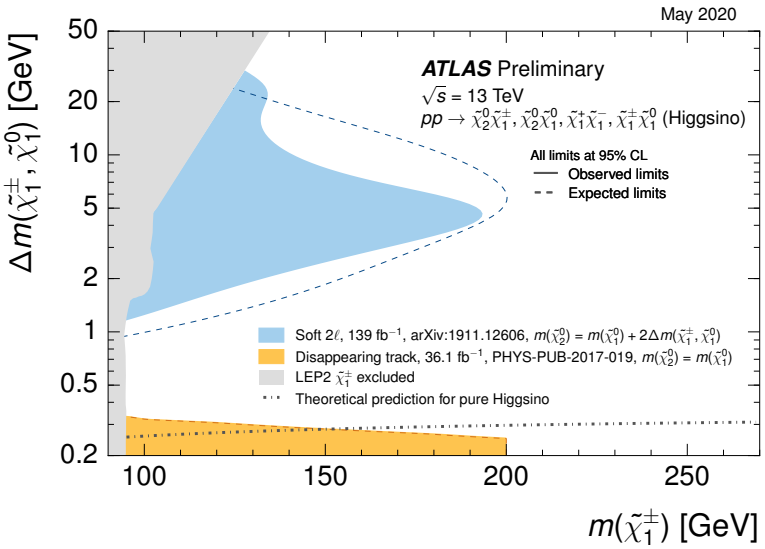

Figure 17: Summary of higgsino searches at the ATLAS (May 2020) [19]

The previous disappearing track search at the ATLAS was performed by using the four-layer tracks with 36.1 fb^{-1} at $\sqrt{s}$ = 13 TeV. Figure 16 shows the result of the previous search for the EWK wino and Figure 17 shows the summary of the higgsino search at the ATLAS. The disappearing track analysis improved the limit of the pure higgsino for the first time in 20 years since the LEP experiment. Figure 18 shows the result of the previous search for the strong channel. Compared to the general SUSY search, there is an advantage to searching for the diagonal region where the activity of jets is soft.

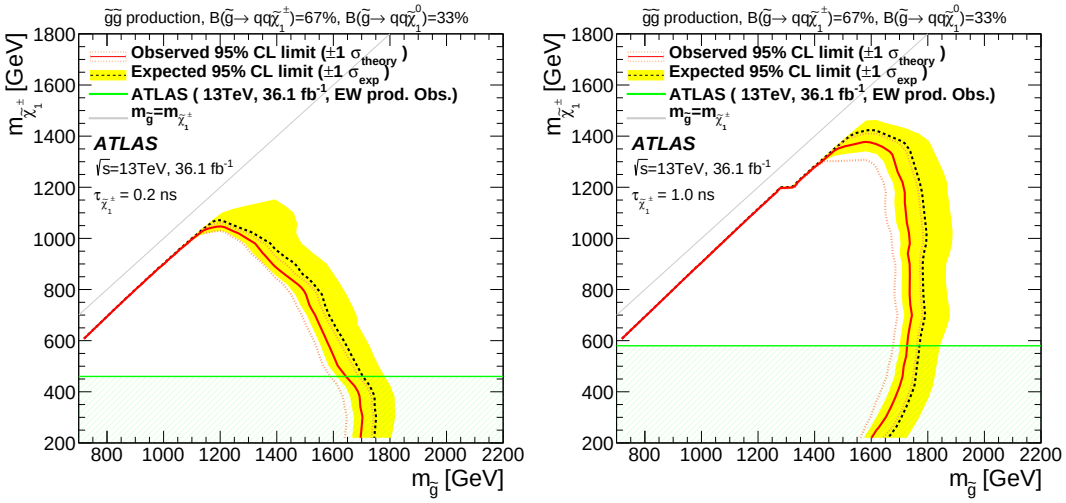

(a) $\tau_{\tilde{\chi}_1^\pm}$ = 0.2 ns

(b) $\tau_{\tilde{\chi}_1^\pm}$ = 1.0 ns

Figure 18: Results of the previous disappearing track search in strong channel [17]

3 LHC and ATLAS detector

ATLAS experiment is one of the four major experiments at LHC. The purposes of ATLAS experiment are precise tests of the standard model and discovery of new physics. In this section, the introduction of LHC is described at first and followed by an overview of the ATLAS detector, and the details of each detector component are described.

3.1 Large Hadron Collider

The Large Hadron Collider (LHC) is the highest energetic particle collider in the world with a circumference of 27 km. It is constructed at 100 m underground of CERN, the European Organization for Nuclear Research, near Geneva in Switzerland. Figure 19 shows the composition of accelerator rings at CERN. The LHC ring is the latest and the largest ring colored with a grey line, and other rings are used as a pre-accelerator or as a beam source for experiments at lower energies. Although the LHC is designed to accelerate protons or heavy ions such as Pb ions, the only proton beam is considered in this paper.

A seed of a proton beam is produced by stripping electrons from hydrogen gas with a duoplasmatron. These protons are extracted by the electric field to a radio frequency quadrupole which provides a transverse focusing of the beam and acceleration, and sent to the linear accelerator (LINAC2[2]) and accelerated up to 50 MeV. Then protons are sequentially accelerated by the Proton Synchrotron Booster (PSB) to 1.4 GeV, by the Proton Synchrotron (PS) to 25 GeV, and by the Super Proton Synchrotron (SPS) to 450 GeV, and finally transferred to the LHC. The LHC has two beam pipes and accelerates protons up to 6.5 TeV for each at Run-2, resulting in a 13 TeV collision.

The LHC repeats a shutdown as a detector upgrade period and a physics run alternately. The past and the post schedule of the LHC and the basic properties for each run are summarized in Table 2[20]. The Higgs boson was discovered at 2012 with Run-1 data by both the ATLAS and the CMS experiments. The main analysis in this thesis is performed by using full Run-2 dataset. In the future, it is planned to collect the total integrated luminosity of 3000 fb^{-1} at $\sqrt{s} = 14$ TeV by the run called high-luminosity LHC (HL-LHC).

[2] LINAC2 has been replaced by the new linear accelerator, LINAC4 which can accelerate protons to 160 MeV, in 2020.

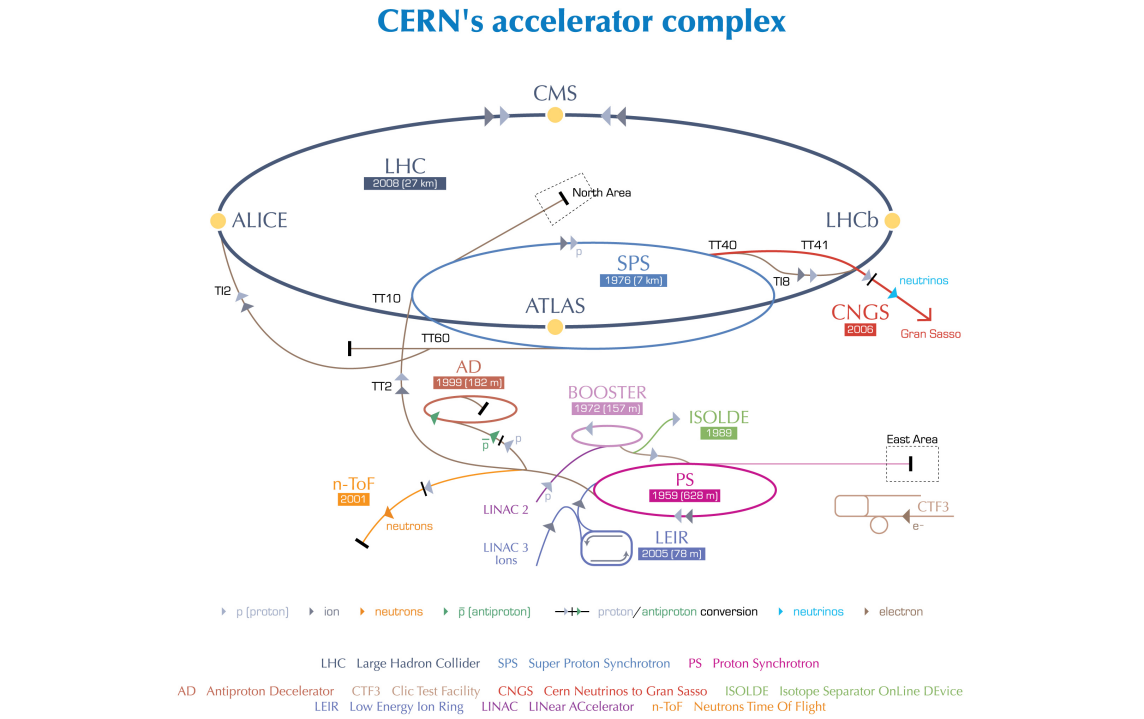

Figure 19: Composition of accelerator rings at CERN

Parameter	Design	Run-1	Run-2	Run-3	HL-LHC
Data taking year		2010 - 2012	2015 - 2018	2022 - 2025	2029 - 2040
Energy [TeV]	14	7/8	13	13.6	14
Integrated luminosity [fb^{-1}]		5/21	140	300	3000
Bunch spacing [ns]	25	50	25	25	25
# of protons per bunch [10^{11}]	1.15	1.6	1.2	1.8	2.2
# of bunches per proton beam	2800	1400	2500	2800	2800
Transverse emittance μm	3.5	2.2	2.2	2.5	2.5
β^*[cm]	55	80	25	25	15
Peak luminosity [$10^{34}cm^{-2}s^{-1}$]	1.0	0.8	2.1	2.0	5.0
Peak pileup	25	45	60	55	150

Table 2: Summary of the LHC properties. The numbers of Run-3 and HL-LHC are expected values.

3.2 ATLAS detector

The layout of the ATLAS detector is shown in figure 20. The ATLAS detector consists of an inner detector, electromagnetic and hadron calorimeters, muon detectors and magnets. The details of each detector are described in the following sub-sections. The proton-proton collisions occur in the center of the detector, so the ATLAS detector covers almost full range in solid angle. The ATLAS detector is forward-backward symmetric around the interaction point and composed of the barrel region and the end-cap regions. Detectors are aligned cylindrically around the beam axis in the barrel region, while aligned perpendicular to the beam axis in the end-cap regions.

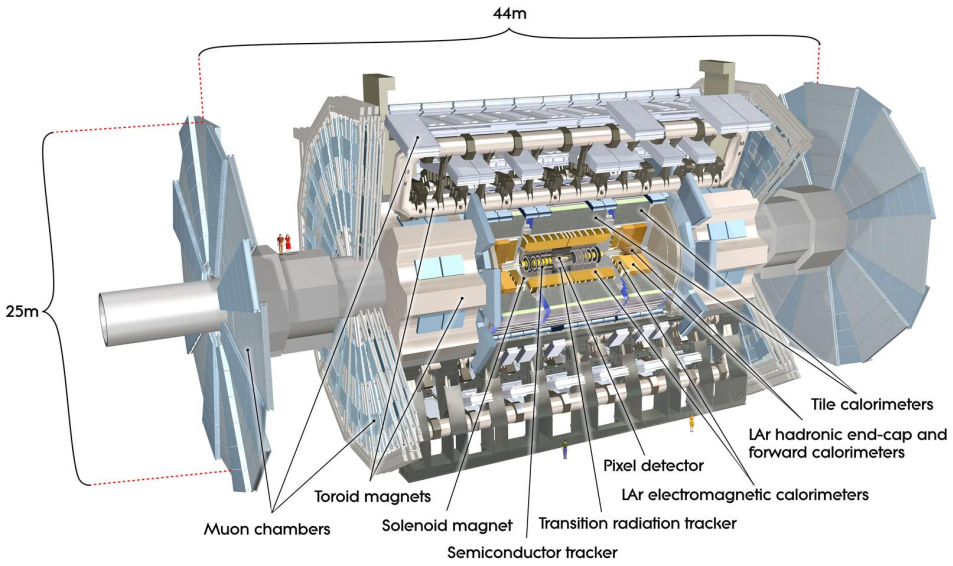

Figure 20: The overview of the ATLAS detector [21]

3.2.1 Coordinate System

Figure 21 shows the coordinate system of the ATLAS experiment. The origin of the global coordinate is the center of the detector. The direction of the positive x-axis is pointing towards the center of the LHC-ring and the positive y-axis is pointing upwards. The z-axis is along with the beam pipe, and the positive z-axis side is called side A and the negative z-axis side is called side C. The azimuthal angle is measured from the x-axis in the x-y plane. The pseudorapidity defined as $\eta = -\ln\tan(\theta/2)$, where θ is the polar angle from the positive z-axis, is used to describe the angle of a particle relative to the beam axis. Angular distance is defined as $\Delta R = \sqrt{(\Delta\eta)^2 + (\Delta\phi)^2}$ and used to calculate closeness between objects. A cylindrical coordinate system (r, ϕ) is used in the x-y plane. Transverse momentum and

energy are defined as $p_{\mathrm{T}} = p \sin\theta$ and $E_T = E \sin\theta$, respectively. The closest point in the transverse plane on a track from the origin is used to calculate the impact parameter in the transverse plane d_0, in the longitudinal plane z_0, and other track parameters. The impact parameters are often referring to the primary vertex instead of the origin. In this case, impact parameters are referred as d_0^{PV} and z_0^{PV} in this thesis.

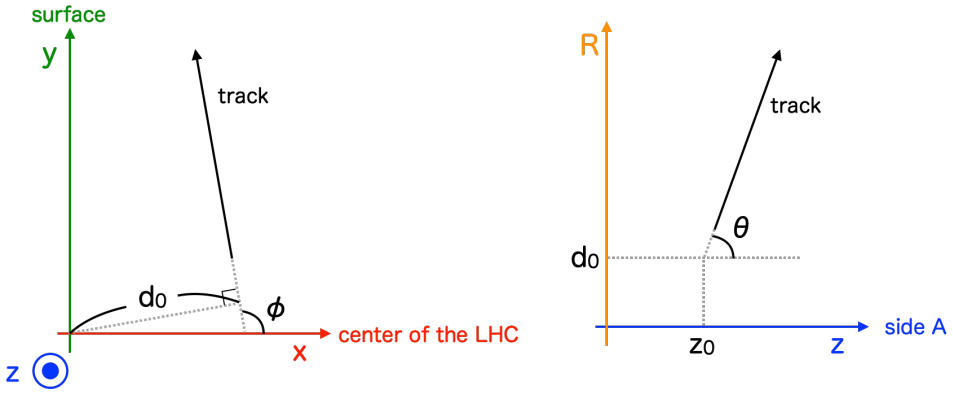

Figure 21: The coordinate system of the ATLAS

3.2.2 Magnet System

The ATLAS magnet system consists of four large superconducting magnets: central solenoid, barrel toroid, and two end-cap toroids. Figure 22 shows the layout of the magnet system. The central solenoid covers the inner detector and provides a uniform 2 T magnetic field for momentum measurement. Figure 23 shows measured axial and radial magnetic fields at several radii as a function of z in the inner detector. The purpose of toroid magnets is to determine muon momentum with high precision. The barrel toroid covers $|\eta| < 1.4$ and the end-cap toroids cover $1.6 < |\eta| < 2.7$. The region in $1.4 < |\eta| < 1.6$ is the transition region and affected by both barrel and end-cap fields. The magnetic field of the toroid system is not uniform, so the bending power is characterized by the integrated magnetic field $\int \mathrm{B} \cdot \mathrm{dl}$. Figure 24 shows the predicted field integral as a function of $|\eta|$ between the innermost and outermost muon chambers. Depend on the radius and azimuth angle, the field varies from 0.15 T to 2.5 T with an average value of 0.5 T in the barrel region, and from 0.2 T to 3.5 T in the end-cap region.

3.2.3 Luminosity Detector

The per-bunch instantaneous luminosity can be expressed as

$$\mathcal{L}_b = f_{\mathrm{LHC}} \frac{\mu}{\sigma_{\mathrm{inel}}} = f_{\mathrm{LHC}} \frac{\mu^{\mathrm{vis}}}{\sigma^{\mathrm{vis}}} \tag{11}$$

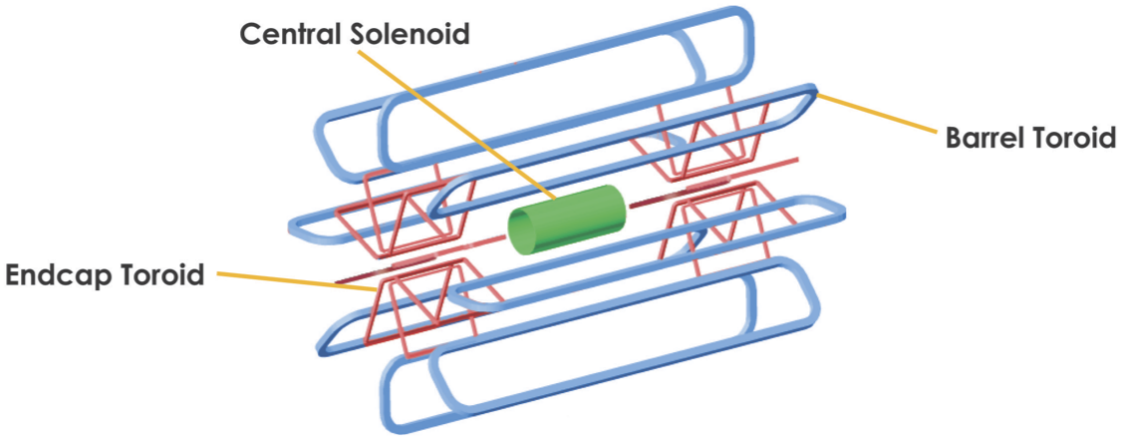

Figure 22: Magnet system [22]

where f_{LHC} is the LHC revolution frequency, σ_{inel} is the total inelastic cross-section, μ is the average number of inelastic interactions per bunch crossing, σ^{vis} and μ^{vis} are the visible cross-section and the visible number of interactions respectively. ATLAS has a dedicated luminosity detector to measure bunch-by-bunch μ^{vis} called LUCID(LUminosity Cherenkov Integrating Detector)-2 in Run-2. LUCID-2 is placed symmetrically around the beam pipe at 17 m from the interaction point and covering both side-A and side-C in $5.6 < |\eta| < 6.0$. It consists of 20+20 photomultipliers with quartz windows or fibers as the Cherenkov medium. The absolute luminosity calibration, which is corresponding to the measurement of σ^{vis}, is performed by the *van der Meer* (vdM) scan [24] only a few times per year in a low-μ environment. During the vdM scan, the beams are separated from the nominal collision point alternately vertically and horizontally, and interaction rates are measured as a function of beam shift. Then the vdM result is transferred to a high-μ environment.

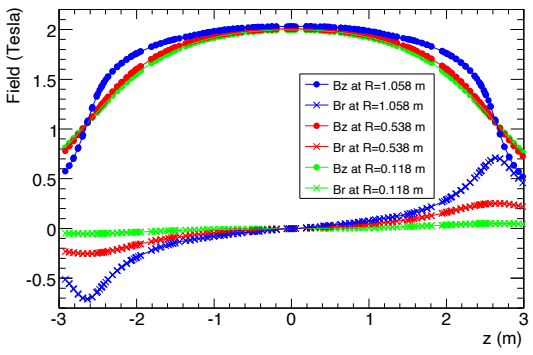

Figure 23: Magnetic field of the solenoid in the inner detector [23]

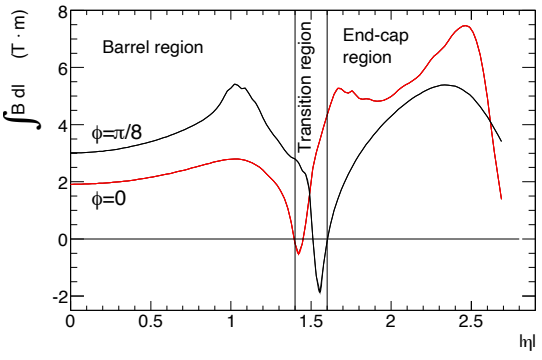

Figure 24: Predicted integral magnetic filed of the toroid [23]

3.2.4 Inner Detector

The ATLAS inner detector is designed to reconstruct tracks of charged particles in $|\eta| < 2.5$ with p_{T} higher than 0.5 GeV as standard configuration. It consists of three sub-detectors: Pixel detector, SemiConductor Tracker (SCT), and Transition Radiation Tracker (TRT) as shown in figure 25.

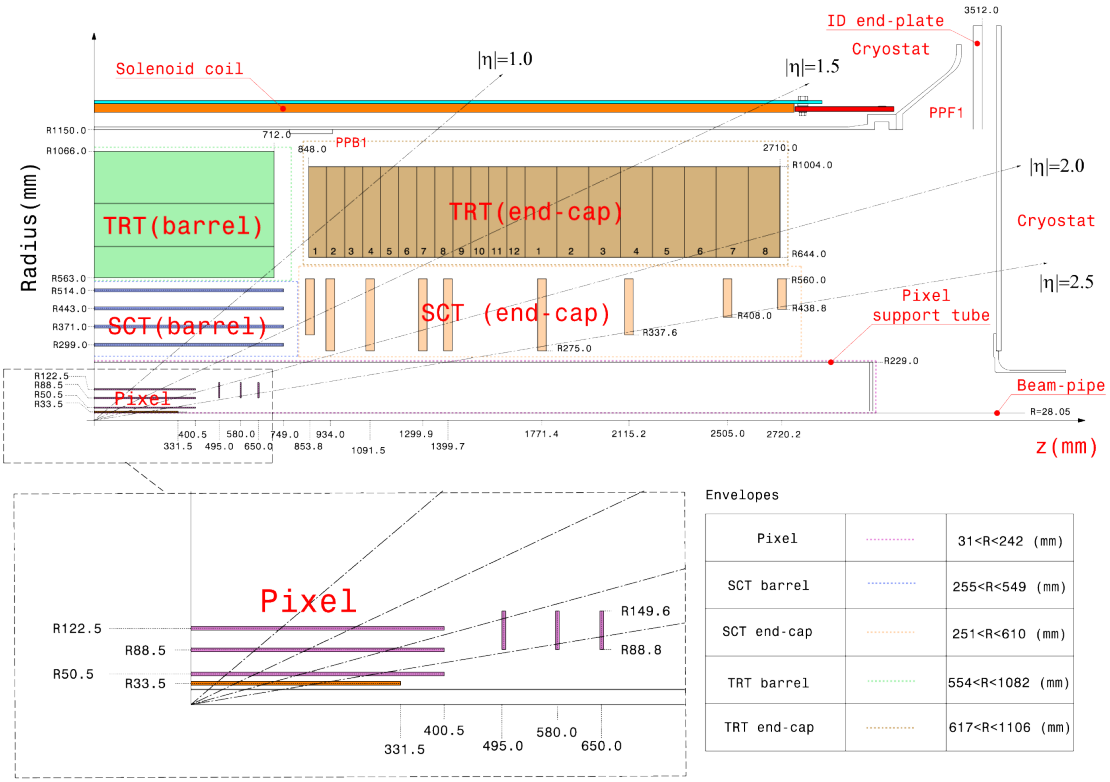

Figure 25: The layout of the ATLAS inner detector [25]

Pixel

The Pixel detector is the innermost part of the inner detector system and is composed of 2D readout silicon sensors. It consists of four-barrel layers and two end-caps each with three disk layers. The innermost barrel layer is called IBL (Insertable B-Layer) and it was installed from Run-2. The pixel size is 50×250 $\mu\mathrm{m}^2$ (ϕ, z) for IBL and 50×400 $\mu\mathrm{m}^2$ (ϕ, z) for other pixel layers. Barrel modules are aligned with a tilt angle of 14 degrees for IBL and 20 degrees for pixel detectors. Barrel modules have an overlap region in ϕ, while there is a small gap between neighboring modules in η. An energy deposit on sensors is stored as a ToT (Time over Threshold) with an accuracy of 4-bit in the IBL readout electronics (FE-I4) and 8-bit in the other pixel layers (FE-I3), so the $\mathrm{d}E/\mathrm{d}x$ of the reconstructed track can be calculated from the pixel detectors.

Since the Pixel detector is the most important detector in this analysis, some detailed variables are introduced below. Each pixel module is consisting of 16 (2 rows x 8 columns) readout chips which are connected to a silicon sensor. But sensor regions between adjacent chips are not covered because some spaces are required between neighboring chips. To recover these uncovered areas, the connection between a pixel in the uncovered region and a pixel on the chip is created. These pixels which are connected to two sensor regions are called *ganged pixels* [26]. Ganged pixels have ambiguity on the hit position because it creates two candidates. Ganged pixel hits that are identified as fake are labeled as *GangedFlaggedFakeHits*. As another quality variable, a cluster of hits with a large error on the hit position normally due to noise is labeled as *SpoiltHits*. During the track reconstruction, a hit that is very close to the track candidate but including the hit makes the track fit quality worse, that hit is labeled as *Outliers*. Hit quality variables SpoiltHits and Outliers are not specific for the Pixel detector.

SCT

The SCT detector consists of four-barrel layers and two end-caps each with nine disk layers. Each SCT module consists of two pairs of single-sided strip sensors glued back-to-back with a 40 mrad angle between them to provide space points. Each strip sensor has 768 active strips with a constant pitch of 80 μm for barrel modules while with various pitches for end-cap modules. Barrel modules are aligned with a tilt angle of 11 degrees and have an overlap region in ϕ. Barrel modules are aligned with a slightly different R position to the neighboring modules in η to have an overlap region also in η. But there is an insensitive region in the center of modules where is a joint section of two sensors.

TRT

The TRT consists of drift tubes with a diameter of 4 mm that are made from wound Kapton and reinforced with thin carbon fibers, with a 0.03 mm diameter gold-plated tungsten wire in the center. The tubes are filled with an Ar-based active gas mixture in Run-2. A Xe-based gas mixture was used at the beginning of the ATLAS operation, however large gas leaks were found then decided to use an Ar-based gas alternatively from the point of cost. The TRT barrel region covers $0.0 < |\eta| < 1.0$ and the end-cap region covers $1.0 < |\eta| < 2.0$. The intrinsic single-point resolution of 120 μm is larger than the silicon trackers, while the number of hits per track is typically more than 30. Electrons emit large transition radiation due to their light mass, so the TRT is also useful for particle identification.

3.2.5 Calorimeter

Calorimeters are designed to measure the energy of particles. The ATLAS calorimeter system consists of the Electromagnetic (EM) calorimeter, the Tile Calorimeter (TileCal), the Hadronic Endcap Calorimeter

(HEC), and the Forward Calorimeter (FCal). Figure 26 shows the structure of the ATLAS calorimeter system.

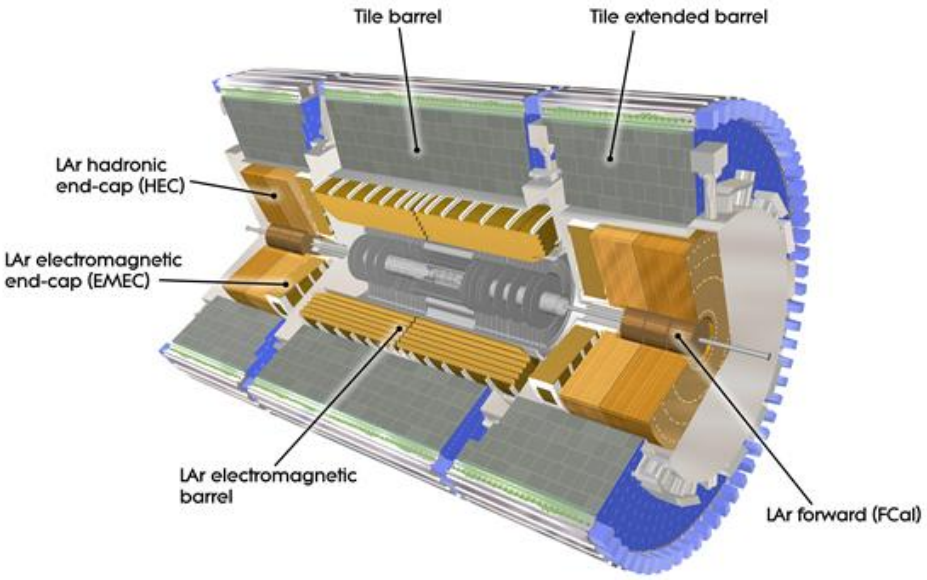

Figure 26: The ATLAS calorimeter system [21]

The EM calorimeter covers $|\eta| < 1.475$ in the barrel region and $1.375 < |\eta| < 3.2$ in the end-cap region. The targets of the EM calorimeters are electrons, positrons, and photons. The dominant processes of an energy loss of these high energy particles in materials are bremsstrahlung for electrons and positrons, and electron-positron production for photons, so they form a cascade of particles. An energy loss of these processes is characterized by a radiation length X_0, which is both mean distance of an electron loses 1/e of their initial energy by bremsstrahlung, and 7/9 of mean free path of a photon for pair production. The X_0 is proportional to $A/(Z(Z+1))$, where A and Z are the mass number and the atomic number of the nucleus respectively, so a lead (Z=82) is used as a passive absorber with liquid argon as an active medium. Figure 27 shows the granularity and structure of the EM barrel calorimeter. The total thickness of the EM calorimeter is $X_0 > 22$ in the barrel region and $X_0 > 24$ in the end-cap region.

The TileCal covers $|\eta| < 1.7$ in the barrel region and it consists of steel as absorber and plastic scintillator as an active medium. Figure 28 shows the structure and the performances of the TileCal. Each TileCal partition consists of 64 modules of equal azimuthal width $\Delta\phi = 0.1$. The scintillators are read out by wavelength shifting fibres on the tile edges to PMTs. The jet energy resolution is better than 10% at momentum above 100 GeV during Run-2.

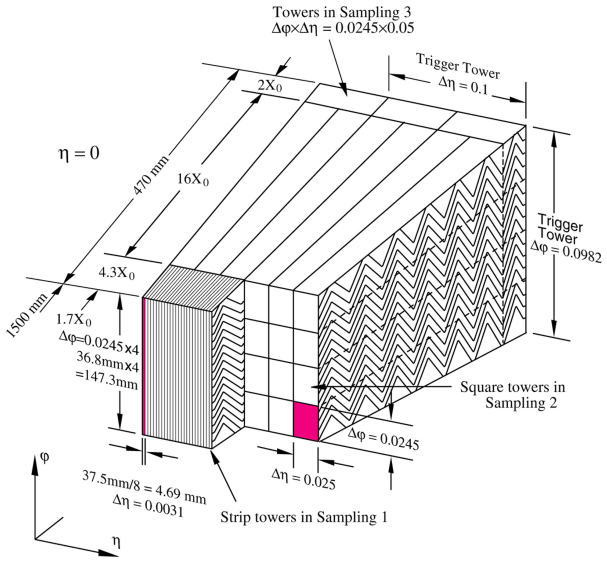

Figure 27: The structure of the EM barrel calorimeter [21]

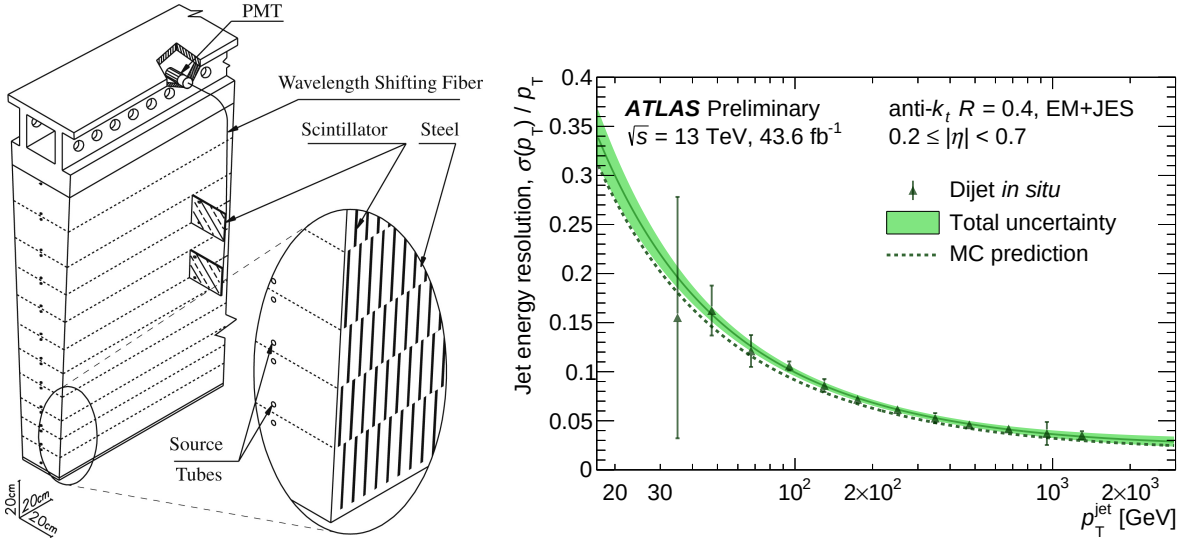

(a) The structure

(b) Run-2 performance

Figure 28: The structure (left) and the performances (right) of the TileCal [21] [27]

The HEC is located outside the EM barrel and covers $1.5 < |\eta| < 3.2$ in the end-cap region and it consists of copper as an absorber and liquid argon as an active medium. The granularity is $\Delta\eta \times \Delta\phi = 0.1 \times 0.1$ in $1.5 < |\eta| < 2.5$ and 0.2×0.2 in $2.5 < |\eta| < 3.2$.

The FCal covers $3.1 < |\eta| < 4.9$ and it consists of three modules. The first module is optimized for electromagnetic measurements and made of copper with liquid argon. Other modules are optimized for hadronic interactions and made of tungsten with liquid argon. The FCal performs an important role in the measurement of missing transverse energy.

Collected calorimeter cell signals are reconstructed as three-dimensional topological clusters [28] so that can have shape and location information by the following algorithm. First, the cell signal significance $\varsigma^{\mathrm{EM}}_{\mathrm{cell}}$ is defined as the ratio of the cell signal $E^{\mathrm{EM}}_{\mathrm{cell}}$ to the expected noise σ_{noise} as below,

$$\varsigma^{\mathrm{EM}}_{\mathrm{cell}} = \frac{E^{\mathrm{EM}}_{\mathrm{cell}}}{\sigma_{\mathrm{noise}}}. \tag{12}$$

Both the cell signal and noise are measured on the electromagnetic (EM) energy scale. This scale reconstructs the energy deposit by electrons and photons correctly but the hadron energies are underestimated, typically about 70% of the energy. All cells with a large significance, typically $|\varsigma^{\mathrm{EM}}_{\mathrm{cell}}| > 4$, can be seeds of the topo-clusters. Then neighboring cells which are directly adjacent in the same layer or which are having at least partial overlap in the (η, ϕ) plane are collected to the seed. The cluster direction is calculated with the absolute energy weights of cells $E^{\mathrm{EM}}_{\mathrm{cell}}$. The direction of each cell is calculated from its location with respect to the center of the ATLAS detector. Each topo-cluster is interpreted as a massless pseudo-particle so that the energy and momentum are calculated as below,

$$\mathrm{P}^{\mathrm{EM}}_{\mathrm{clus}} = E^{\mathrm{EM}}_{\mathrm{clus}} \cdot (1, \sin\theta_{\mathrm{clus}} \cos\phi_{\mathrm{clus}}, \sin\theta_{\mathrm{clus}} \sin\phi_{\mathrm{clus}}, \cos\theta_{\mathrm{clus}}) = \left(E^{\mathrm{EM}}_{\mathrm{clus}}, \vec{p}^{\,\mathrm{EM}}_{\mathrm{clus}}\right). \tag{13}$$

Isolation variable E_T^{coneXX} ($E_T^{\mathrm{topoclusXX}}$) is defined as the scalar sum of calorimeter cell energies (topo-cluster energies) inside a cone of a radius ΔR =0.XX around the object.

3.2.6 Muon Spectrometer

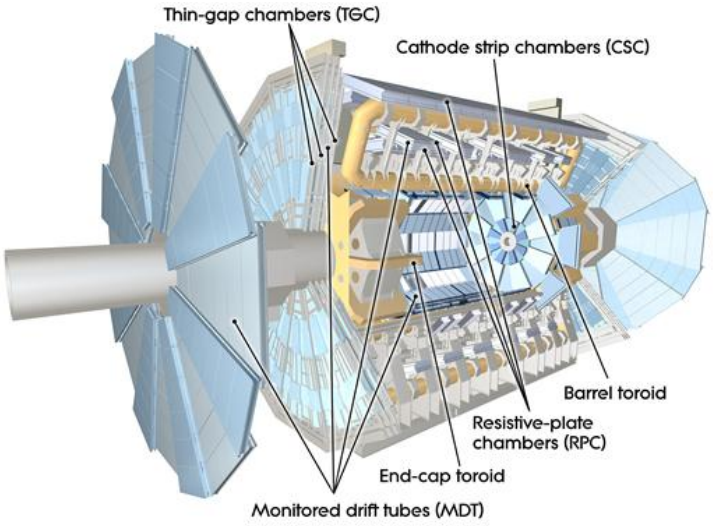

Figure 29: The overview of the muon spectrometer [23]

The muon spectrometer is the outermost detector in the ATLAS and consists of Thin Gap Chambers (TGC), Resistive Plate Chambers (RPC), Monitored Drift Tubes (MDT), and Cathode Strip Chambers (CSC). Figure 29 shows the overview of the muon system. The precision momentum measurement is mainly performed by the MDT chambers in $|\eta| < 2.7$. These chambers consist of three to eight layers of drift tubes and achieve an average resolution of 35 μm per chamber. The innermost end-cap layer of the MDT in $2.0 < |\eta| < 2.7$ is replaced by the CSC due to their higher rate capability and time resolution. The resolution of the CSC is 40 μm in the bending plane and about 5 mm in the transverse plane. The RPC and TGC are used for triggering in the barrel ($|\eta| < 1.05$) and end-cap ($1.05 < |\eta| < 2.4$) regions, respectively. The trigger chambers are also able to measure both coordinates of the track in the bending (η) plane and the non-bending (ϕ) plane. Matching between the MDT and trigger chamber hits is performed in the bending plane and then the trigger chamber's coordinate in the non-bending plane is adopted as the second coordinate of the MDT measurement.

3.2.7 Trigger and Data Acquisition System

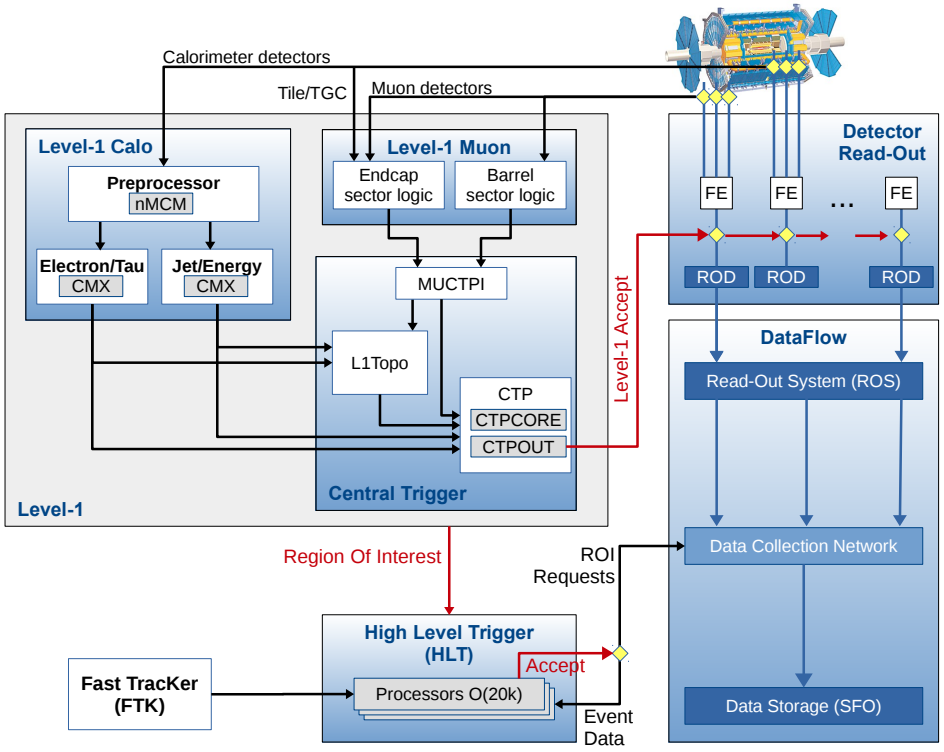

Figure 30: The ATLAS trigger system [29]

The Trigger and Data Acquisition (collectively TDAQ) system is important to select and store interest events in offline analysis. Figure 30 shows the stream of the ATLAS TDAQ system. The trigger system in Run-2 consists of a hardware-based Level-1 (L1) trigger and a software-based high-level trigger (HLT). The L1 trigger accepts events up to 100 kHz from the bunch crossing rate of 40 MHz based on information with a reduced granularity from the calorimeter and muon detectors. The HLT received Regions-of-Interest (RoI) from the L1 triggers and more complex algorithms operate with full granularity detector information in either the RoI or the whole event. The HLT reduces the rate to a few kHz within a processing time of about 200 ms. Once an event is accepted by the HLT, the Sub-Farm Output (SFO) sends the data to permanent storage and then exports it to the Tier-0 facility [30] at CERN's computing center.

3.2.8 Datasets

Data sample

The raw data samples used for this thesis were recorded by the ATLAS detector from 2015 to 2018

(Run-2) in pp collisions at the center-of-mass energy $\sqrt{s}$ = 13 TeV. The peak instantaneous luminosity at the start of fills reached 2.1×10^{34} cm^{-2}s^{-1}. Figure 31 shows the evolution of the total integrated luminosity during Run-2. The total integrated luminosity after data quality selections is 136 fb^{-1}with an uncertainty of 1.7 %. Figure 32 shows the distribution of the average number of interactions per bunch crossing for each data-taking year. The mean number of interactions per bunch crossing distributes from approximately 20 to 60.

Simulated sample

Simulated Monte Carlo (MC) events were used to develop the analysis and estimate the experimental sensitivity to given models. All samples were generated at $\sqrt{s}$ = 13 TeV with a single configuration of the detector and were simulated through GEANT4. Every sample with pile-up used in this thesis was overlaid during digitisation with additional minimum-bias events. Minimum-bias events were generated with Pythia 8.235 and EvtGen v.1.6.0, the A14 tune and the leading order parton distribution function (PDF) set `NNPDF23LO`.

The signal MC samples were generated using MadGraph5 v2.6.2 interfaced to Pythia8 v8.230 and EvtGen v.1.6.0 with A14 NNPDF23LO PDF. Charginos ($\tau_{\tilde{\chi}_1^\pm}$) were forced to decay into $\tilde{\chi}_1^0 + \pi^\pm$ in the Geant4 simulation based on their lifetime $\tau_{\tilde{\chi}_1^\pm}$ in the rest frame. For the wino search in EWK channel, the signal MC samples with the lifetime $\tau_{\tilde{\chi}_1^\pm}$ = 0.2, 1.0, 4.0 and 10.0 ns were generated in the mass range from 91 GeV to 1000 GeV approximately every 100 GeV. For the higgsino search in EWK channel, the signal MC samples with the lifetime $\tau_{\tilde{\chi}_1^\pm}$ = 0.2, 1.0, 4.0 and 10.0 ns were generated at the masses of 120 GeV, 160 GeV, and 240 GeV, and wino samples are used for other mass points to save computing resources. The basic properties of charginos and neutralino in the pure higgsino-LSP scenario are the same as in the pure wino LSP scenario except for the p_{T} of charged pion. But this effect is negligible in this analysis because the typical pion p_{T} of 340 MeV in the pure higgsino LSP scenario is still too low

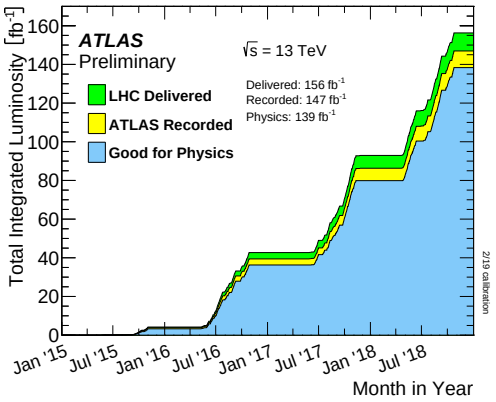

Figure 31: Evolution of total integrated luminosity at Run-2. [31]

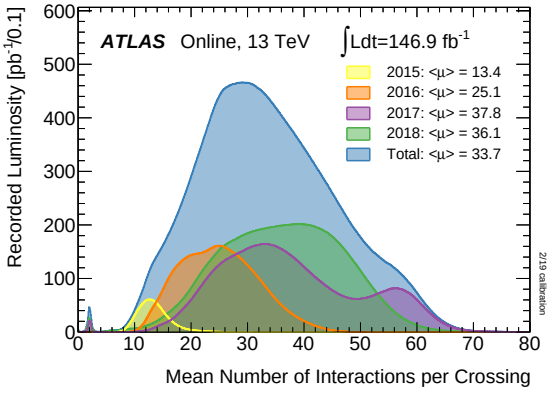

Figure 32: Number of interactions per bunch crossing. [31]

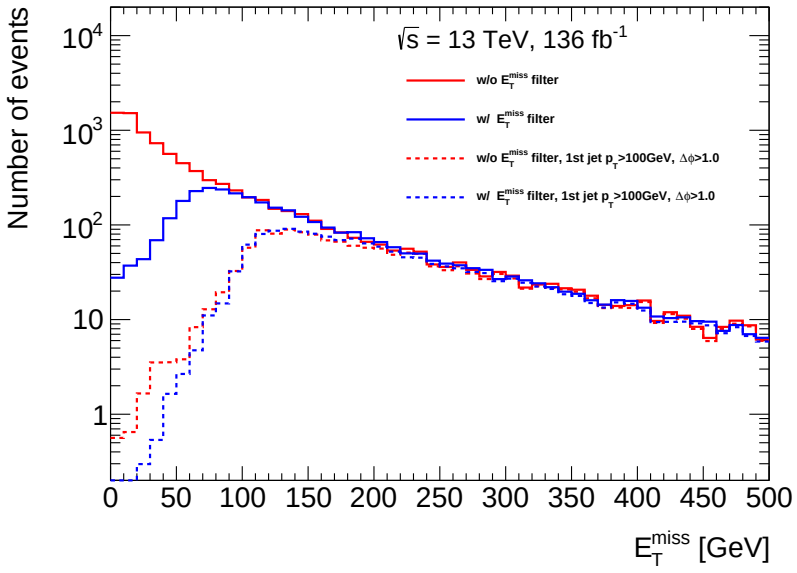

Figure 33: $E_{\mathrm{T}}^{\mathrm{miss}}$ distribution with and without $E_{\mathrm{T}}^{\mathrm{miss}}$ filter. Chargino mass is 500 GeV. Truth $E_{\mathrm{T}}^{\mathrm{miss}}$ filter reduce low $E_{\mathrm{T}}^{\mathrm{miss}}$ region especially $E_{\mathrm{T}}^{\mathrm{miss}} < 100$ GeV. When leading jet p_{T} cut is applied, the difference becomes very small.

to be reconstructed as a track. Validation of using wino samples for the higgsino search is summarized in Appendix A.

Signal MC samples with different mean lifetimes are obtained by applying event weights so that the distribution of the proper lifetime follows that for a given value of the mean lifetime. The event weight w is given by

$$w(\tau_{\tilde{\chi}_1^\pm}) = \prod_i^{n_{\tilde{\chi}_1^\pm}} \frac{\tau_0}{\tau_{\tilde{\chi}_1^\pm}} \exp\left[-t_i\left(\frac{1}{\tau_{\tilde{\chi}_1^\pm}} - \frac{1}{\tau_0}\right)\right], \tag{14}$$

where $n_{\tilde{\chi}_1^\pm}$, τ_0 and t_i are the number of charginos in the event, the chargino mean lifetime set in the simulation and the proper lifetime of i–th chargino, respectively. Validation of the lifetime reweighting procedure is summarized in Appendix B.

In this thesis, generator-level information is called truth. Signal samples were generated by requiring $E_{\mathrm{T}}^{\mathrm{miss}} > 60$ GeV at truth level to save storage. Here truth $E_{\mathrm{T}}^{\mathrm{miss}}$ is defined as the sum of the momenta of non-interacting particles at detector-level. Figure 33 shows the $E_{\mathrm{T}}^{\mathrm{miss}}$ distribution with and without $E_{\mathrm{T}}^{\mathrm{miss}}$ filter. There is no difference above $E_{\mathrm{T}}^{\mathrm{miss}} > 100$ GeV. For the wino samples in the EWK channel, all the signal parameters in the AMSB model, corresponding chargino masses ($m_{\tilde{\chi}_1^\pm}$) and cross sections are summarised in Table 3. For the higgsino samples in the EWK channel, chargino masses and cross sections are summarized in Table 4.

$m_{3/2}$[TeV]	$m_{\tilde{\chi}_1^\pm}$[GeV]	Lifetimes [nsec]	Cross section (C1C1, C1N1) [pb]
31.4	90.7	0.2, 1.0, 10.0	15.815, 31.317
68.0	199.7	0.2, 1.0, 10.0	0.883338,1.77743
102.4	299.8	0.2, 1.0, 10.0	0.186804, 0.381311
137.4	400.3	0.2, 1.0, 4.0, 10.0	0.0567824,0.117921
172.6	500.2	0.2, 1.0, 4.0, 10.0	0.0212685,0.0446763
208.0	599.9	0.2, 1.0, 4.0, 10.0	0.00911829, 0.0193666
243.8	700.1	0.2, 1.0, 4.0, 10.0	0.00418792, 0.00901699
279.6	799.9	0.2, 1.0, 4.0, 10.0	0.00207723, 0.00449871
315.6	899.8	0.2, 1.0, 4.0, 10.0	0.00108363, 0.00233598
351.8	1000.1	0.2, 1.0, 4.0, 10.0	0.00057336, 0.00124413

Table 3: Summary of AMSB signal parameters, chargino masses, lifetime and their NLO cross sections at $\sqrt{s}$ = 13 TeV with m_0 = 5000 GeV, tan β = 5 and $\mu > 0$.

$m_{\tilde{\chi}_1^\pm}$[GeV]	Lifetimes [nsec]	Cross section (C1C1, C1N1) [pb]
91	0.2, 1.0, 10.0	4.5937780, 8.7963320
120	0.2, 1.0, 4.0, 10.0	1.6287660, 2.9496620
160	0.2, 1.0, 4.0, 10.0	0.5725636, 1.0065236
200	0.2, 1.0, 10.0	0.2443210, 0.4241660
240	0.2, 1.0, 4.0, 10.0	0.1270172, 0.2195998
300	0.2, 1.0, 10.0	0.0525690, 0.0908167
400	0.2, 1.0, 4.0, 10.0	0.0163405, 0.0284230
500	0.2, 1.0, 4.0, 10.0	0.00621625, 0.01088650
600	0.2, 1.0, 4.0, 10.0	0.00268388, 0.00473741
700	0.2, 1.0, 4.0, 10.0	0.00125981, 0.00223385
800	0.2, 1.0, 4.0, 10.0	0.000630966, 0.001123920
900	0.2, 1.0, 4.0, 10.0	0.000328529, 0.000586950
1000	0.2, 1.0, 4.0, 10.0	0.000182305, 0.000311324

Table 4: Summary of the cross-section for higgsino signal samples.

For the strong production, a simplified model was used assuming branching ratios of gluino decay are 1/3 for $\tilde{g} \to qq\tilde{\chi}^0$, $\tilde{g} \to qq\tilde{\chi}^-$ and $\tilde{g} \to qq\tilde{\chi}^+$, respectively. Only four flavours of quarks were considered: d, u, c and s. The mean lifetime of the chargino ($\tau_{\tilde{\chi}_1^\pm}$) was set to 1.0 ns for most of the samples; the chargino lifetime follows exponential decay with 1 ns in the rest frame. A sample with a lifetime of 0.2 ns was also produced for validating the lifetime re-weighting procedure. Samples were generated for the signal points over chargino masses from 100 GeV to 2150 GeV and gluino masses from 700 GeV to 2400 GeV. The samples are listed in Table 5.

$m_{\tilde{g}}$[TeV]	$m_{\tilde{\chi}_1^\pm}$[GeV]	Cross section [pb]
0.7	600, 650	4.32
0.8	600, 700, 750	1.81
1.0	100, 300, 500, 700, 900, 950	0.385
1.2	100, 300, 500, 700, 900, 1100, 1150	0.0985
1.4	100, 300, 500, 700, 900, 1100, 1300, 1350	0.0284
1.6	100, 300, 500, 700, 900, 1100, 1300, 1500, 1550	0.00887
1.8	100, 300, 500, 700, 900, 1100, 1300, 1500, 1700, 1750	0.00293
2.0	100, 300, 500, 700, 900, 1100, 1300, 1500, 1700, 1900, 1950	0.00101
2.2	100, 300, 500, 700, 900, 1100, 1300, 1500, 1700, 1900, 2100, 2150	0.000356
2.4	100, 300, 700, 1100, 1500, 1900	0.000128

Table 5: Summary of gluino mass, chargino masses and their cross sections at $\sqrt{s}$ = 13TeV for strong production.

4 Physics Object Definitions

The object definitions used in the analysis are summarised in this section. First, the reconstruction algorithm and the definition of standard tracks which are common track objects for analyses at the ATLAS are described. Next, the definition of the pixel-track which is the specific object for this analysis is introduced. Detailed performances of the pixel-track are shown in the next chapter. Then definitions of other objects used in this analysis are described. Since jets, muons, and electrons are reconstructed independently, there might be an overlap between these objects. Hence the procedure of the overlap removal is summarized after object definitions. Finally, several event-level cleaning criteria are introduced.

4.1 Standard Tracks

Charged particles create hits in pixel and strip sensors, and the hits are grouped into clusters. From these clusters, three-dimensional measurements referred to as space points are created. For the SCT, clusters from both sides of layers must be combined to obtain space points. The inner detector tracking covers two sequences, the main inside-out track reconstruction and a consecutive outside-in tracking.

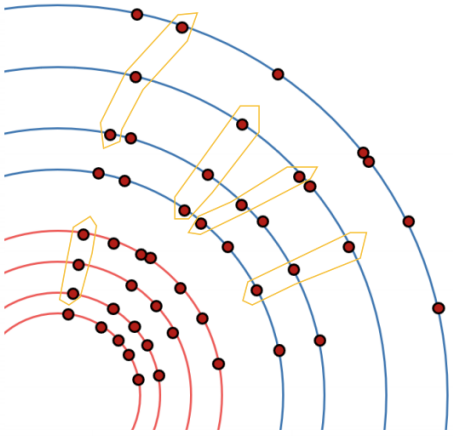

Figure 34: Space points seeds finding [32]

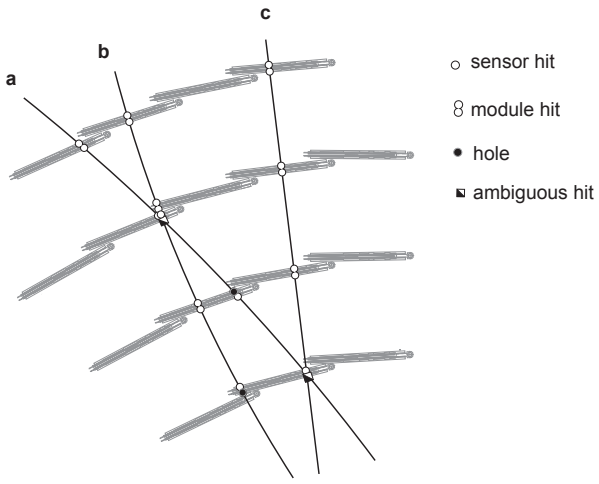

Figure 35: Track scoring in the SCT barrel [33]

Inside-out sequence

The primary track reconstruction starts by forming seeds of triplets of space points in either the Pixel or SCT layers as shown in figure 34. These track seeds are pre-selected by imposing a minimum requirement on the momentum or maximum requirement on the impact parameters to

save computing resources. Once the space points seeds are found, the road windows are built according to the seed direction. Then any hits within the road window are collected and track candidates are built using a combinatorial Kalman filter. Track candidates usually contain fake tracks or overlapping track segments with shared hits. So the ambiguity solving is performed by scoring track candidates based on associated hits. Figure 35 shows an example in the SCT barrel layers. Hits in an overlap region like track **b** are particularly highly scored, while holes on track lead to a penalty in the track score. Finally, an extension of the track into the TRT detector is attempted. The tracks with TRT hits are refitted with the global χ^2 fitter, and TRT hits are added to the tracks if the score is improved, otherwise silicon-only tracks are kept.

Outside-in sequence

The primary reconstruction sequence is optimized to reconstruct particles produced in the primary pp interactions. To recover tracks from secondary decay vertices or photon conversions, the secondary reconstruction sequence starts with the segments of TRT hits. Since the TRT drift tubes can not create 3D space points, the global pattern recognition has to be done in projective planes, i.e. the $r-\phi$ plane in the TRT barrel region, and the $r-z$ plane in the TRT end-cap region, respectively. So the Hough transform is used to find the hit pattern by transforming the projection plane into the straight line. Then the backtracking of the TRT segments into the silicon detectors is performed to find small track segments of silicon hits.

Tracks reconstructed with the above algorithms are called *standard tracks*. These standard tracks satisfy the following requirements :

- $p_{\mathrm{T}} > 500$ MeV
- $|\eta| < 2.5$
- $N^{\mathrm{Si}}_{\mathrm{Hits}} \geq 7$
- $(N^{\mathrm{Pixel}}_{\mathrm{SharedHits}} + N^{\mathrm{SCT}}_{\mathrm{SharedHits}}/2) \leq 1$
- $N^{\mathrm{Si}}_{\mathrm{MissingHits}} \leq 2$
- $N^{\mathrm{Pixel}}_{\mathrm{MissingHits}} \leq 1$

Due to the requirement of the silicon hits, standard tracks typically tend to be longer than 37 cm in the transverse plane.

4.2 Pixel-Track

A dedicated reconstruction is developed to target the short chargino tracks, herein referred to as *pixel-track*. The pixel-track reconstruction runs after the standard tracks reconstruction as a second-pass tracking. The algorithm is based on the standard reconstruction, however, it only uses unused hits not associated with any standard tracks, and only pixel hits are used for the seed finding. Track seeds from combinations of three space points are extended into the remaining pixel and SCT layers, and at least four hits are required for the track to be accepted. The requirement of the number of hits is loosened, however, missing hits or shared hits in the trajectory are not allowed. The $p_{\mathrm{T}} > 5$ GeV and $|\eta| < 2.2$ are required during the reconstruction, and the following requirements are applied in the offline analysis:

(1) $p_{\mathrm{T}} > 20$ GeV.

(2) $0.1 < |\eta| < 1.9$.

(3) pixel-track consists of only four-pixel barrel layers (no SCT hits).

(4) $N^{\mathrm{Pixel}}_{\mathrm{GangedFlaggedFakeHits}} = 0$, $N^{\mathrm{Pixel}}_{\mathrm{SpoiltHits}} = 0$, $N^{\mathrm{Pixel}}_{\mathrm{Outliers}} = 0$.

(5) The pixel-track should have a good χ^2-probability of the fit $P(\chi^2, \mathrm{NDF}) = 1-\gamma(\mathrm{NDF}/2, \chi^2/2) > 0.1$, where $\gamma(\mathrm{NDF}/2, \chi^2/2)$ is the incomplete gamma function.

(6) $|d_0/\mathrm{err}(d_0)| < 1.5$ and $|z_0 \sin\theta| < 0.5$ mm.

(7) The pixel-track should be isolated; $p_{\mathrm{T}}^{\mathrm{cone40}}/p_{\mathrm{T}} < 0.04$, where $p_{\mathrm{T}}^{\mathrm{cone40}}$ is the scalar sum of the p_{T} of all standard tracks with $p_{\mathrm{T}} > 1$ GeV in a cone of $\Delta R < 0.4$ around the pixel-track, where $\Delta R = \sqrt{\Delta\phi^2 + \Delta\eta^2}$. In addition (and new from the previous analysis), calorimeter isolation is used and applied as $\mathrm{E}_{\mathrm{T}}^{\mathrm{topoclus20}} < 5.0$ GeV. More details are presented in Section 6.3.4.

(8) The pixel-track should be the highest momentum pixel-track among isolated pixel-tracks in the event.

(9) Overlap removal between the pixel-track and other objects in the event is applied. For signal, the pixel-track should be isolated from jets, electrons, muons and muon spectrometer tracks. The distance between the pixel-track and any jets with $p_{\mathrm{T}} > 50$ GeV, and electrons, muons and muon spectrometer tracks with $p_{\mathrm{T}} > 10$ GeV should be greater than 0.4 in the η–ϕ space.

The requirements for η are necessary to reduce SM particle tracks because the muon detector is inactive at small $|\eta|$ and the background rates increase significantly in high $|\eta|$. In this analysis, only disappearing tracks consisting of four layers are considered, so no SCT hits are required as a disappearing track condition. The requirements (4), (5) and (6) are useful to reduce fake tracks. Most high-p_{T} background

events have bad tracking properties and tend to have large impact parameters. The requirements (7), (8) and (9) are useful to reduce standard particle originated background pixel-tracks. Since scattered muons might be possible to propagate into the muon system but these fail to associate inner detector tracks. Therefore overlap removal of tracks for both muons and muon spectrometer tracks is applied.

4.3 Jets

Jets are reconstructed using the anti-k_t algorithm [34] with a radius parameter $R = 0.4$. The inputs to the jet reconstruction algorithm are topological calorimeter clusters [35] which attempt to reconstruct the three-dimensional shower topology of each particle entering the calorimeters. The transverse momenta of jets are corrected by application of a jet energy scale (JES) calibration derived from simulation and by in situ corrections obtained from 13 TeV data. The details of the jet calibration procedure are given in Ref. [36]. In the analysis, the acceptance cuts of $p_{\mathrm{T}} > 20$ GeV and $|\eta| < 2.8$ are applied. In order to reduce contributions from pile-up jets, all jets with $|\eta| < 2.5$ and $p_{\mathrm{T}} < 60$ GeV are required to satisfy the jet-to-vertex tagger (JVT) requirements. The efficiency of the tagger is about 92% to identify jets from the hard-scatter vertex.

4.4 Muons

Muon candidates are identified by two algorithms. One is an algorithm that combines a track reconstructed in the muon spectrometer with a track in the inner detector or an ID track seeded algorithm [21, 37]. The other is an algorithm that reconstructs a muon by using the muon spectrometer only. Muons are selected with "Medium" quality criteria [38]. They are also required to have $p_{\mathrm{T}} > 10$ GeV, $|\eta| < 2.7$, $|d_0/\mathrm{err}(d_0)| < 3.0$, and $|z_0 \sin\theta| < 0.5$ mm. Not only the prompt production such as the decay of W and Z, but muons can also arise from sequential processes such as semileptonic decays of heavy quarks. Such background muons typically have a large activity around the object. Therefore, to select the muons from the prompt production (referred as *signal muons*), both track-based and calorimeter-based isolation cuts are applied. The relative energy fraction within a cone around the muon candidate is required to be less than 0.15 and 0.30 compared to the muon p_{T} for track-based and calorimeter-based isolation criteria respectively. The cone size is $\Delta R = 0.2$ for calorimeter-based isolation, while it is defined by the following formula for track-based isolation.

$$\Delta R = \min\left(\frac{10\ \mathrm{GeV}}{p_{\mathrm{T}}\ [\mathrm{GeV}]},\ 0.3\right). \tag{15}$$

4.5 Electrons

Electrons are selected by using a likelihood based on tracking and calorimeter information with "LooseAndBLayerLLH" quality criteria [39]. They are also required to have $p_{\mathrm{T}} > 10$ GeV, $|\eta| < 2.47$, $|d_0/\mathrm{err}(d_0)| < 5.0$, and $|z_0 \sin\theta| < 0.5$ mm. Same as the muons, not only the prompt production such as the decay of W and Z, but electrons can also arise from sequential processes such as semileptonic decays of heavy quarks and photons conversion into electron-positron pairs. Such background electrons typically have a large activity around the object. Therefore, to select the electrons from the prompt production (referred as *signal electrons*), both track-based and calorimeter-based isolation cuts are applied. The relative energy fraction within a cone around the electron candidate is required to be less than 0.15 and 0.20 compared to the electron p_{T} for track-based and calorimeter-based isolation criteria respectively. The cone size is $\Delta R = 0.2$ for calorimeter-based isolation, while it is defined by the following formula for track-based isolation.

$$\Delta R = \min\left(\frac{10\ \mathrm{GeV}}{p_{\mathrm{T}}\ [\mathrm{GeV}]},\ 0.2\right). \tag{16}$$

4.6 Missing Transverse Momentum

The missing transverse momentum is calculated based on the transverse momenta of selected jets, lepton candidates described above, and soft-tracks which are not associated to such objects,

$$\vec{p}_{\mathrm{T}}^{\,\mathrm{miss}} = -\sum \vec{p}_{\mathrm{T}}^{\,\mathrm{jet}} - \sum \vec{p}_{\mathrm{T}}^{\,\mathrm{electon}} - \sum \vec{p}_{\mathrm{T}}^{\,\mathrm{muon}} - \sum \vec{p}_{\mathrm{T}}^{\,\mathrm{soft-track}} \tag{17}$$

The magnitude of $\vec{p}_{\mathrm{T}}^{\,\mathrm{miss}}$ is represented as $E_{\mathrm{T}}^{\mathrm{miss}}$. Soft tracks are defined as following :

- $N_{\mathrm{Hits}}^{\mathrm{Si}} \geq 9$ for $|\eta| \leq 1.65$, or $N_{\mathrm{Hits}}^{\mathrm{Si}} \geq 11$ for $|\eta| > 1.65$
- $(N_{\mathrm{Hits}}^{\mathrm{InnermostPixel}} + N_{\mathrm{Hits}}^{\mathrm{SecondInnermostPixel}}) > 0$
- $N_{\mathrm{MissingHits}}^{\mathrm{Pixel}} = 0$
- $|d_0| < 2.0$ mm
- $|z_0 \sin\theta| < 3.0$ mm
- if the track has high p_{T} ($p_{\mathrm{T}} > 200$ GeV for $|\eta| < 1.5$, or $p_{\mathrm{T}} > 120$ GeV for $|\eta| \geq 1.5$), the following requirements need to be satisfied:

  for isolated track ($p_{\mathrm{T}}^{\mathrm{cone20}}/p_{\mathrm{T}} < 0.1$), either a), b), or c) is satisfied :

a). $|\sigma(q/p)/(q/p)| < 0.05$

b). $E_T^{\text{cone10}}/p_{\text{T}} < 0.1$ and $|\sigma(q/p)/(q/p)| < 0.1$

c). $E_T^{\text{cone10}}/p_{\text{T}} > 0.65$ and $|\sigma(q/p)/(q/p)| < 0.4$

for non-isolated track ($p_{\text{T}}^{\text{cone20}}/p_{\text{T}} \geq 0.1$), either a) or b) is satisfied :

a). $E_T^{\text{cone10}}/(p_{\text{T}} + p_{\text{T}}^{\text{cone20}}) > 0.6$

b). $p_{\text{T}}/(p_{\text{T}} + p_{\text{T}}^{\text{cone20}}) < 0.6$

Pixel-tracks are not included in $E_{\text{T}}^{\text{miss}}$ soft-track term. Due to the small mass splittings and the two body decay of a heavy chargino to a light pion and heavy neutralino, the momentum of the neutralino will be very close to that of the decaying chargino, thus if the pixel-tracks were included into the $E_{\text{T}}^{\text{miss}}$ calculation the event would be balanced and there would be no $E_{\text{T}}^{\text{miss}}$ in the event for $\tilde{\chi}_1^+\tilde{\chi}_1^-$ production modes. In addition, the p_{T} resolution of the pixel-tracks is extremely poor compared to standard tracks.

4.7 Overlap Removal

When the physics objects defined in Section 4 overlap each other, one of the overlapping objects is removed based on the following order:

1. If an electron candidate and a muon candidate share the same ID track, the muon candidate is removed if the muon is a calo-muon, and the electron candidate is removed if the muon is not a calo-muon.

2. If an electron candidate and a jet are found within $\Delta R < 0.2$, they are classified as an electron and the jet is removed.

3. If an electron candidate and a jet are found within $\Delta R < 0.4$, they are classified as a jet and the electron is removed.

4. If a muon candidate and a jet are ghost-associated or found within $\Delta R < 0.2$, they are classified as a muon and the jet is removed as long as the number of tracks with $p_{\text{T}} > 500$ MeV associated to the jet is less than three.

5. If a muon candidate and a jet are found within $\Delta R < 0.4$, they are classified as a jet and the muon is removed.

4.8 Event Cleaning

For the physics analysis, only the data which has enough qualities in all detector subsystems can be used. In this sub-section, all event-level cleanings are described.

Good Runs List (GRL) Each of the recorded datasets is called *run* and assigned a unique six-digit run number. Each run is further divided into luminosity blocks (LBs) and each LB corresponds to a period of 60 s. The datasets which passed basic data quality validations are summarized as a Good Runs List (GRL) which contain the list of LBs that are available for the physics analysis[40]. In this analysis, a special GRL rejecting further SCT defects in addition to the normal GRL is used and resulting in a data loss of about 3 fb^{-1}.

Detector-error veto Rejection of bad or corrupted events due to detector error is an ATLAS-wide recommendation :

- LAr noise bursts and data corruption
- a handful of Tile-corrupted events
- events affected by the recovery procedure for single event upsets in the SCT
- events incomplete after TTC restart

Bad jet cleaning First, if there are any jets that do not pass loose jet cleaning("LooseBad"), the events are removed. Second, if there is a leading jet that does not pass tight jet cleaning("TightBad") or whose $|\eta|$ is more than 2.4, the events are removed. The second criterion is to reduce non-collision background.

Bad-muon-event veto Badly reconstructed muons can affect the $E_{\text{T}}^{\text{miss}}$ calculation, especially in the tail region. If a baseline muon before overlap removal which has $\sigma(q/p)/|q/p| > 0.4$, is found, the event is rejected.

Bad-muon $\boldsymbol{E}_{\mathbf{T}}^{\mathbf{miss}}$ cleaning To reject events whose $E_{\mathrm{T}}^{\mathrm{miss}}$ is affected by badly reconstructed muons even after the bad-muon event veto mentioned above, events satisfying the following criteria are rejected:

$$\frac{E_{\mathrm{T}}^{\mathrm{miss,muon}}}{E_{\mathrm{T}}^{\mathrm{miss}}} \cos\left\{\phi(E_{\mathrm{T}}^{\mathrm{miss,muon}}) - \phi(E_{\mathrm{T}}^{\mathrm{miss}})\right\} > 0.5, \tag{18}$$

where $E_{\mathrm{T}}^{\mathrm{miss,muon}}$ is muon term of $E_{\mathrm{T}}^{\mathrm{miss}}$ (negative vector sum of muon $\vec{p}_{\mathrm{T}}$).

5 Pixel-Track Performance

In this section, the basic performances of the pixel-tracks are described. Section 5.1 focuses on the difference between data and MC on the track efficiency. Section 5.2 and Section 5.3 describe the track efficiency and resolutions of the track parameters, especially for the signal charginos. Finally, Section 5.4 describes measurements of the smearing functions, which play an important role in the analysis.

5.1 Pixel Dead Modules map

The modeling by MC method is not perfect, so the tracking efficiency and the resolutions of the track parameters are different from MC events to data. The main source of the efficiency difference is the mis-modeling of pixel dead module map which is especially related to the requirement of the four-pixel layers. To calculate correction factors, the track efficiency is measured in both data and MC by using Z$\rightarrow \mu\mu$ candidates. The event selection criteria to enhance $Z \rightarrow \mu\mu$ events are summarized below. The definition of tag and probe muons are described at Sec. 6.4.1.

- Trigger : The lowest unprescaled single muon triggers
- No identified electrons
- At least one tag muon
- At least one probe muon
- $|m_{tag,probe} - m_Z| < 10$ GeV

In addition to the above selection, standard tracks associated with probe muon should satisfy the following requirements.

- $p_T > 15$ GeV
- $N_{Hits}^{Pixel} >= 1$
- $N_{Hits}^{SCT} >= 6$
- $N_{Hits}^{TRT} >= 5$

Then calculate the efficiency that probe muon satisfies the number of pixel layers >= 4. Figure 36 shows the result for each data taken years. The ratio of data to MC will be applied to signal MC samples to take into account the differences in track efficiencies.

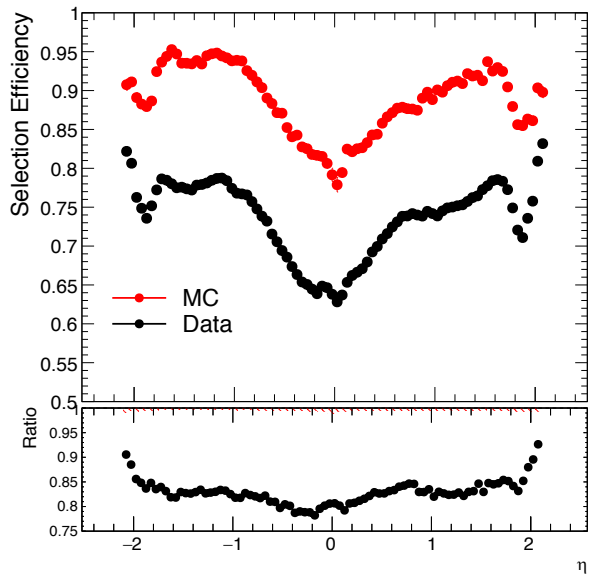

(a) 2015 + 2016 data vs MC

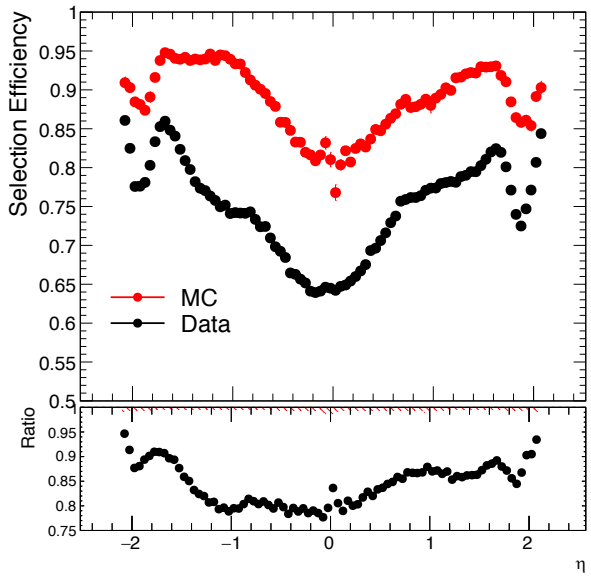

(b) 2017 data vs MC

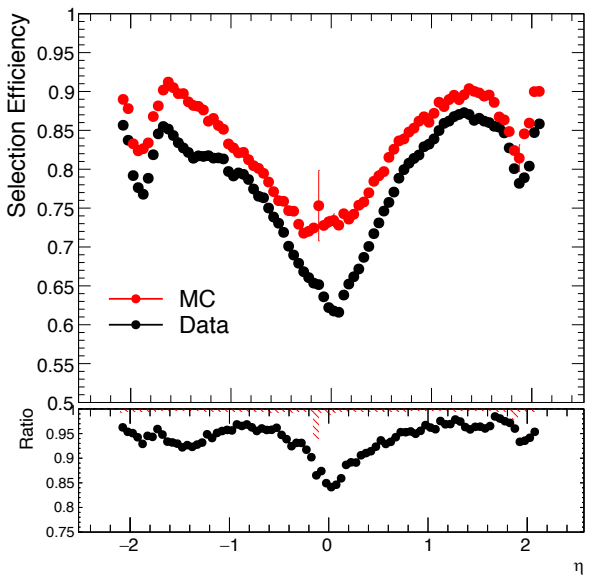

(c) 2018 data vs MC

Figure 36: The efficiency of (number of pixel layers >= 4) requirement

5.2 Pixel-Track Efficiency

Figure 37 shows the track efficiency for signal wino samples at ($m_{\tilde{\chi}_1^\pm}$, $\tau_{\tilde{\chi}_1^\pm}$) = (600 GeV, 1.0 ns) as a function of decay radius. Reconstructed tracks are applied with truth matching within $\Delta R < 0.10$ to truth charginos. To increase statistics, kinematics cut is not applied because it does not have a strong bias to the efficiency. Without any track selections, the overall efficiency in the fiducial volume is about 57%, and it decreases to 42% and 28% with four-layer selection, and all track selections including dead pixel modules respectively. As shown in figure 38, the pixel-track efficiency has lifetime dependence.

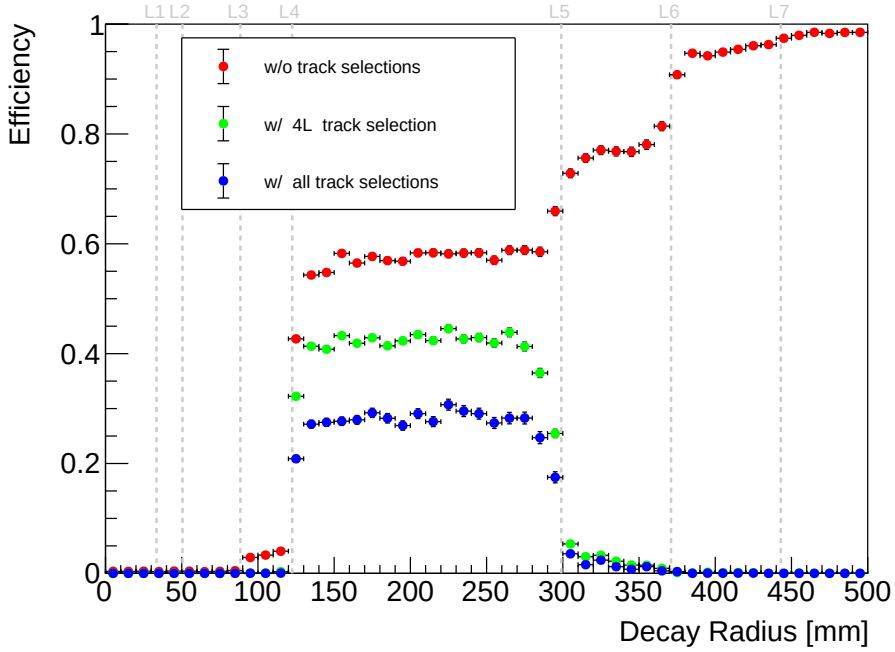

Figure 37: Pixel-track efficiency as a function of decay radius

Figure 39 shows the truth p_T of charginos which decay in the region of 122.5 mm < R < 299.0 mm. The fraction of charginos with p_T > 500 GeV is about 71%, 27%, 14% and 11% at $\tau_{\tilde{\chi}_1^\pm}$ = 0.2, 1.0, 4.0 and 10.0 ns, respectively. The charginos in the short lifetime region need to be much boosted to reach fiducial volume and tend to have higher p_T, so the efficiency of reconstructed objects becomes high. Figure 40 shows the decay radius distribution of charginos. The fraction of charginos that decay within the fiducial region between the 4th and 5th layers, and becomes the maximum around $\tau_{\tilde{\chi}_1^\pm}$ = 1.0ns. The overall acceptance times efficiency is a convolution of the decay radius distribution and the track efficiency. Actually, it becomes the maximum around $\tau_{\tilde{\chi}_1^\pm}$ = 1.0 ns.

Figure 41 shows the relative pixel-track efficiency normalized at $\langle\mu\rangle$ = 20. The denominator is the

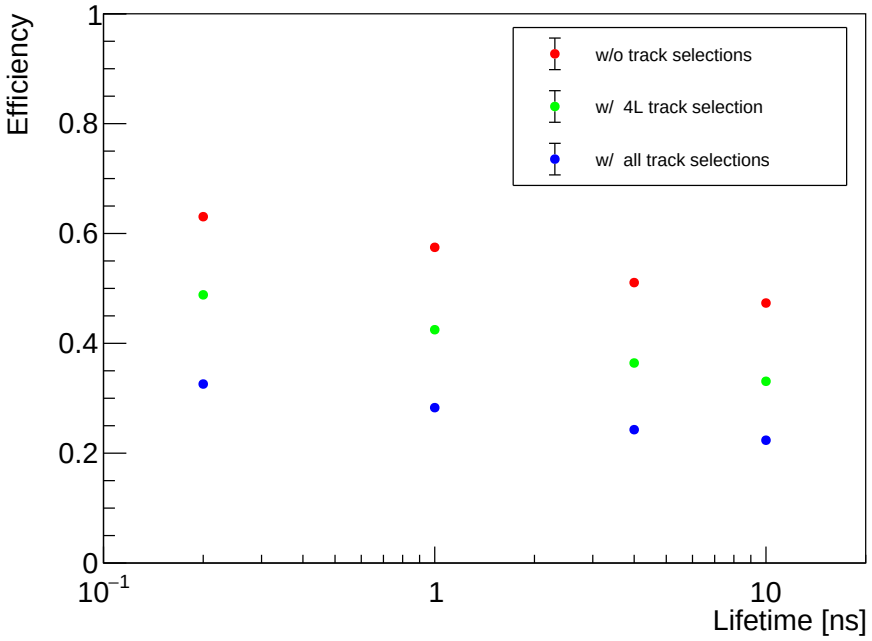

Figure 38: Lifetime dependence of pixel-track efficiency

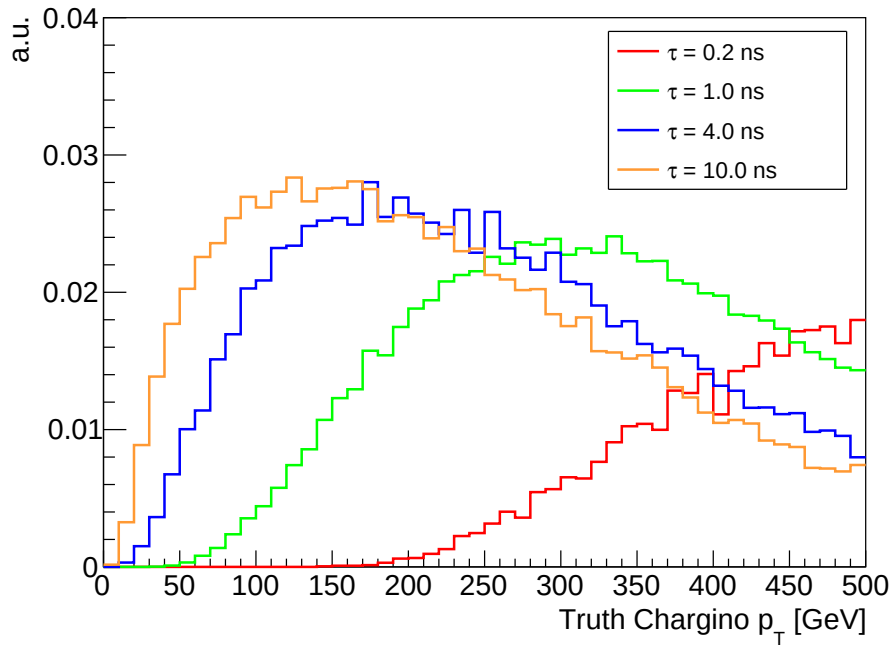

Figure 39: Truth p_{T} distribution of charginos in 122.5 mm < R < 299.0 mm

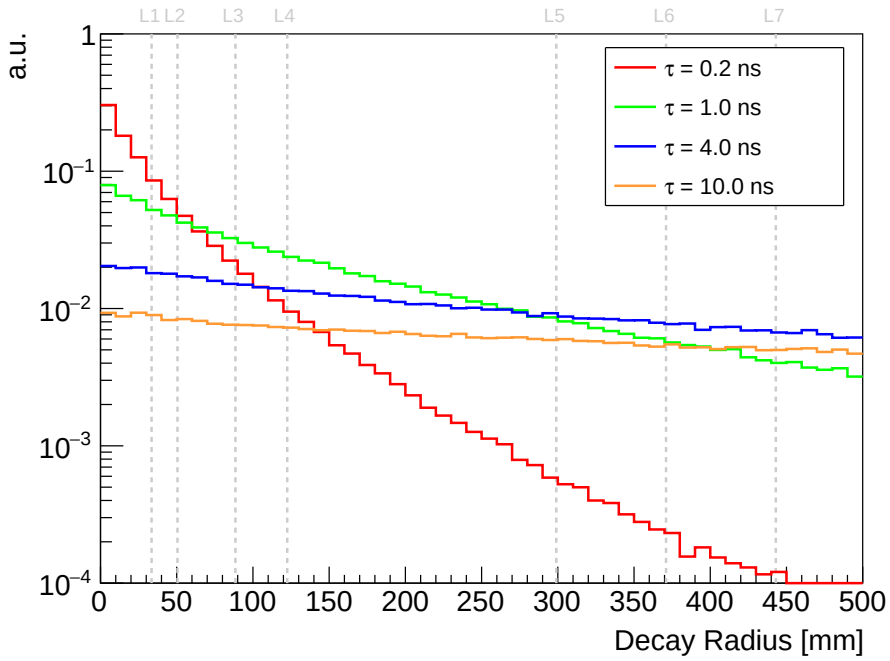

Figure 40: Decay radius distribution of charginos

pile-up distribution drawn with a grey histogram, and the numerator is the number of events in each category. No kinematical cut is applied to every category to increase statistics. Pixel-tracks basically satisfies all requirements described in Sec. 4.2. Only signals are simulated events while others are evaluated by data. For fake BG, $|d_0/\mathrm{err}(d_0)| > 10$ is required instead of $|d_0/\mathrm{err}(d_0)| < 1.5$. For low-$p_\mathrm{T}$ BG, $p_\mathrm{T} < 60$ GeV is applied and hadron or electron BG is dominant in this region. For chargino signals, track selections are completely same in the signal regions. According to this figure, the fraction of fake tracks tends to increase along with $\langle\mu\rangle$ while others decrease.

5.3 Pixel-Track Resolution in Signal MC

Figure 42 shows the distribution of residuals of q/p_T, η and ϕ for the truth charginos and reconstructed tracks with various track lengths. The *n-layer track* in the legends in the Figure 42 (a) - (c) means that the track consists of consecutive n barrel layers from the innermost layer. Any selections in both kinematics and track qualities are not applied. Although residuals of q/p_T and η depend on their absolute values, the overall distributions are shown. The main object of this analysis is the 4-layer track. It has a poor momentum resolution but has a good enough pointing resolution of $O(10^{-3})$ in η and ϕ. Resolutions of track parameters basically improve along with the track length, however, some of the 5-layer tracks have worse resolution than the 4-layer tracks. This is because some tracks that should be

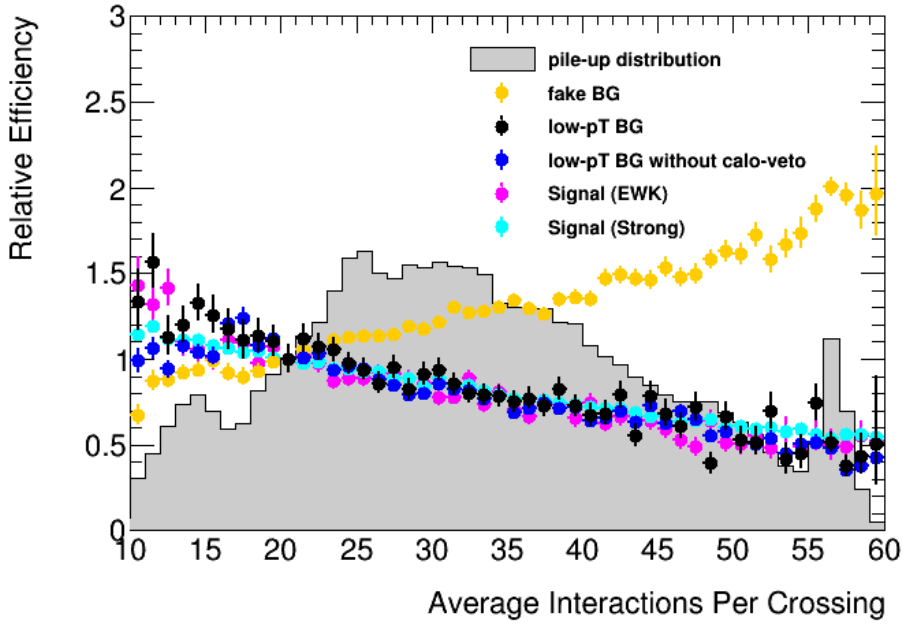

Figure 41: Relative pixel-track efficiency normalized at $\langle\mu\rangle = 20$ as a function of $\langle\mu\rangle$. Magenta and cyan points are signal MC for EWK and strong channels, respectively. Black and blue points are data in the low-p_{T} hadron background-rich region with and without the calorimeter veto requirement. Orange points are data in the fake background-rich region. Gray histogram shows pile-up distribution during Run-2 data taking.

reconstructed as 4-layer tracks are accidentally reconstructed as 5-layer tracks by associating spurious hits in the innermost SCT layer (i.e. 5th silicon layer). Figure 43 shows the distribution in $\Delta q/p_{\mathrm{T}}$ and decay radius plane of 5-layer tracks. Mis-reconstructed tracks make the tail in the distribution of residuals. This negative aspect affects this analysis only from the point of inefficiency.

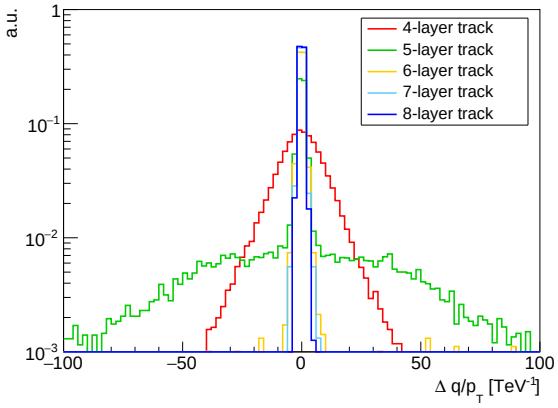

(a) $\Delta q/p_T$

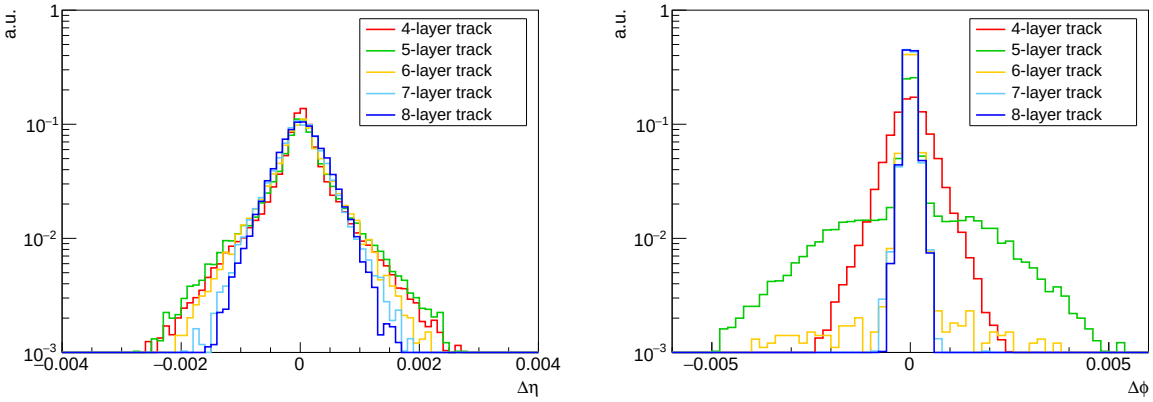

(b) $\Delta\eta$ (c) $\Delta\phi$

Figure 42: Residual of track parameters for each n-layer track

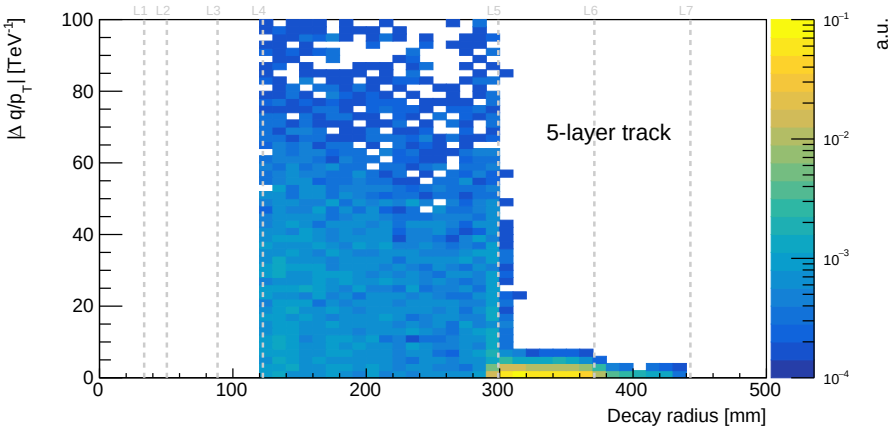

Figure 43: $\Delta q/p_T$ vs decay radius of 5-layer track

5.4 Pixel-Track Smearing Functions

Due to the resolution difference between data and MC, the reconstructed track p_{T} in signal MC needs some corrections. These are two ways to estimate the signal p_{T} spectrum:

1. Measure the resolution difference between data sample and corresponding MC events, and apply the smearing function to the reconstructed p_{T}.
2. Measure pixel-track p_{T} resolution in data and apply smearing function to the truth p_{T}.

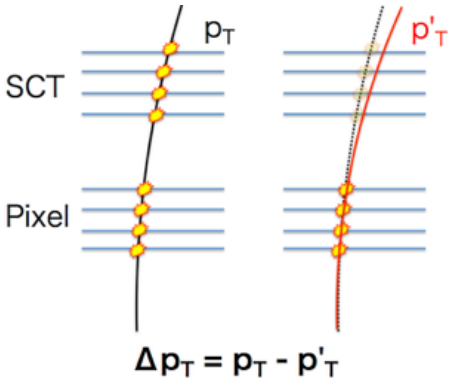

Figure 44: Re-tracking technique

The latter method is used as a primary method in this analysis because this is also useful to estimate the background pixel-track spectra in data from the standard tracks. The p_{T} resolution of the pixel-track is measured by comparing the p_{T} of the standard track and the artificial pixel-track which is obtained by re-tracking the standard track with only pixel hits as shown in Figure 44.

5.4.1 Event Selection

Since processing all events with re-tracking is computationally expensive, only part of the dataset is processed for the measurement of the smearing functions. The runs are chosen to sample different data-taking conditions across the various years : 284285 (2015), 302872 (2016), 340072 (2017), and 358395 (2018). To measure the smearing functions for muons and electrons, the $Z \to \mu\mu$ and $Z \to ee$ events are extracted by applying the following selections.

- Trigger : The lowest unprescaled single muon/electron triggers
- Require two same-flavour leptons and no different-flavour leptons
- Reconstructed di-lepton mass ($M_{\ell\ell}$) is within a range of 10 GeV from the Z boson mass
- Leading lepton p_{T} is larger than 25 GeV
- Sub-leading lepton $p_{\mathrm{T}} > 20$ GeV.

- Search for the artificial pixel-tracks corresponding to each lepton track by applying ΔR(pixel-track, lepton-track) < 0.2.

The pixel-tracks are required to pass the normal disappearing-track selections described in Section 4.2 except for the lepton veto. Finally, smearing functions are measured by comparing the p_{T} of the lepton-track and the p_{T} of the artificial pixel-track.

5.4.2 Fit Function

In tracking, q/p_T is a more elementary variable than p_{T}. So $\Delta q/p_T$ between artificial pixel-tracks and original tracks is measured. The $\Delta q/p_T$ distribution is fitted by the *ExpGaussExp* function [41]:

$$\begin{aligned} f(z) &= \begin{cases} \exp(\alpha(z+\alpha/2)) & (z < -\alpha) \\ \exp(-z^2/2) & (-\alpha < z < \alpha), \\ \exp(-\alpha(z-\alpha/2)) & (z > \alpha) \end{cases} \\ z &= \frac{\Delta(q/p_T) - \beta}{\sigma}, \end{aligned} \tag{19}$$

where α, β and σ are parameters representing the slope of the tail part, the mean of the core part and the resolution of the core part respectively. The smeared momentum is calculated as

$$p_T^{\mathrm{smeared}} = \left| \left(\frac{q}{p_T} \right)^{\mathrm{original}} + \mathrm{random}(f(z)) \right|^{-1}, \tag{20}$$

where random$(f(z))$ is a random number from the smearing function distribution. The fitting results to the data points in the individual p_{T} bins for muons and electrons are shown in Figures 45 and 46, respectively.

5.4.3 Various Dependencies

The smearing functions depend on particle types. Figure 47(a) shows the sigma measured in single particle MC for electron, muon, and pion. Since muons and pions have similar values, the smearing function for muons is also applied to pions. Figure 47(b) shows the $\Delta q/p_{\mathrm{T}}$ distribution for charginos and electrons in the high-p_{T} region. The signal charginos have a similar shape to the electron rather than the muon, so the smearing function for the electron is applied to the signal charginos. The smearing functions also depend on the p_{T}, so their parameters are measured in several p_{T} regions. Figure 48 shows the smearing parameters as a function of the p_{T}. The clear dependency has been observed in

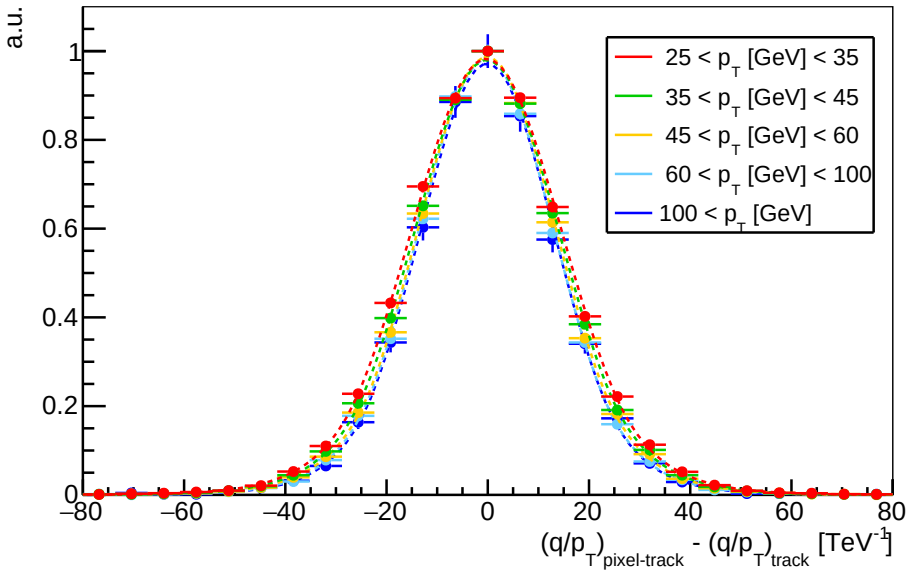

Figure 45: Fits in each of the individual p_{T} bins for the **muon** smearing function extraction. Data points are shown, as well as the resulting fit function super-imposed as a dotted line above the data points.

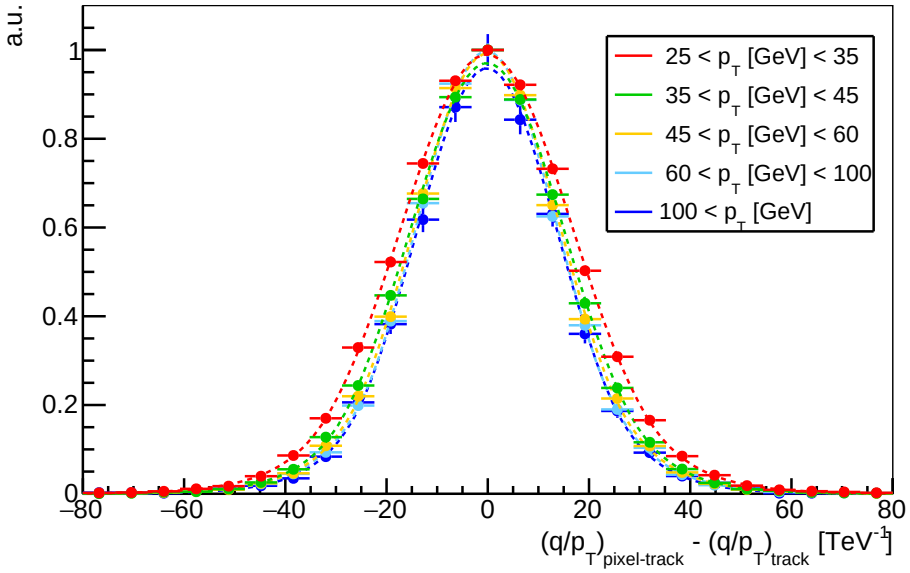

Figure 46: Fits in each of the individual p_{T} bins for the **electron** smearing function extraction. Data points are shown, as well as the resulting fit function super-imposed as a dotted line above the data points.

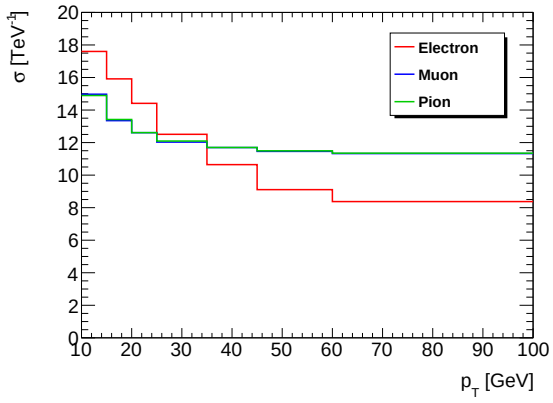

(a) Comparison between electrons, muons, and pions

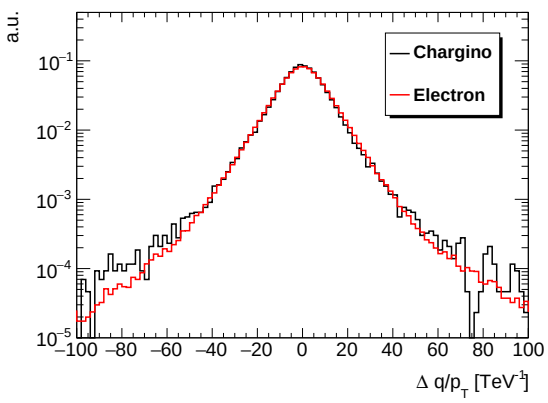

(b) Comparison between charginos and electrons

Figure 47: Particle type dependence of the smearing function.

the parameter σ. In high pile-up environments, hits from pile-up tracks could contaminate the pixel-track and lead to a degradation in momentum resolution, especially in the low-p_{T} region. Figure 49 shows the pile-up dependence of smearing parameters in the region of 25 GeV $< p_{\mathrm{T}} <$ 35 GeV. The resolution parameter σ grows as a function of the average number of interactions per bunch crossing. The smearing parameters are categorized into low pile-up and high pile-up conditions, and then half of the absolute differences between the high and low pile-up conditions are taken as uncertainties on the inclusive parameters.

5.4.4 Extrapolation to Low-p_{T} Region

The parameter σ has p_{T} dependence, and function parameters are measured in data for $p_{\mathrm{T}} > 25$ GeV. The smearing function will be applied for track $p_{\mathrm{T}} > 10$ GeV, so σ is estimated from single-particle MC in the low-p_{T} region. Figure 50 shows σ as a function of the track p_{T}. The σ in the low-p_{T} region is estimated by assuming that the data value is a square root of the sum of squares of the MC value and correction term.

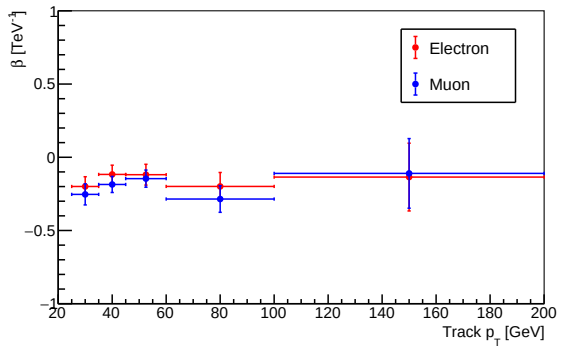

(a) β

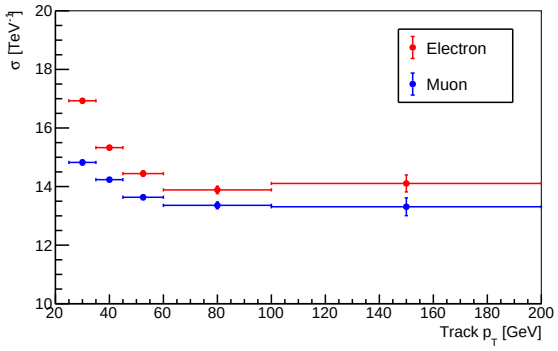

(b) σ

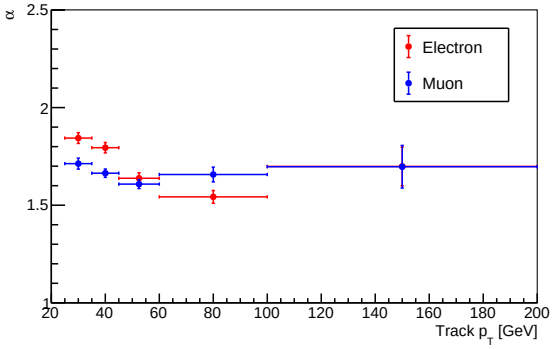

(c) α

Figure 48: The p_T dependence of smearing parameters as a function of the p_{T}. The red line shows the electron and the blue line shows the muon.

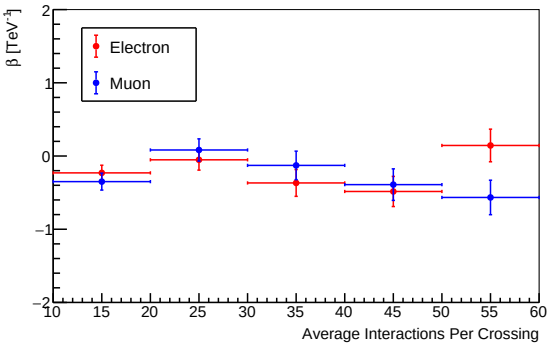

(a) β

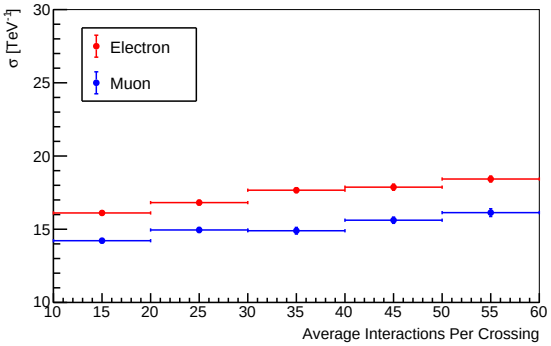

(b) σ

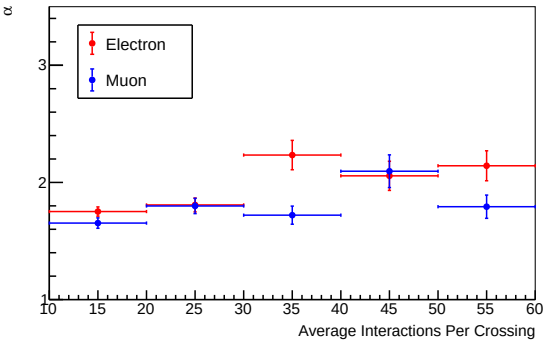

(c) α

Figure 49: The pile-up dependence of smearing parameters. (25 GeV $< p_{\mathrm{T}} <$ 35 GeV)

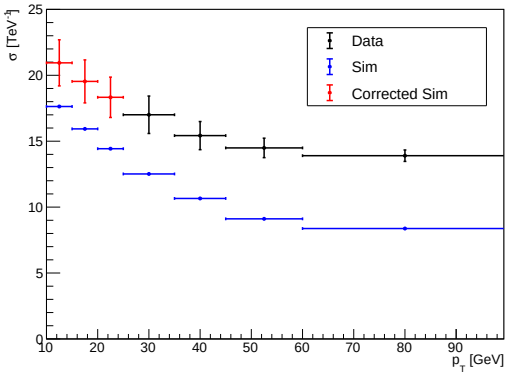

(a) **Electrons**

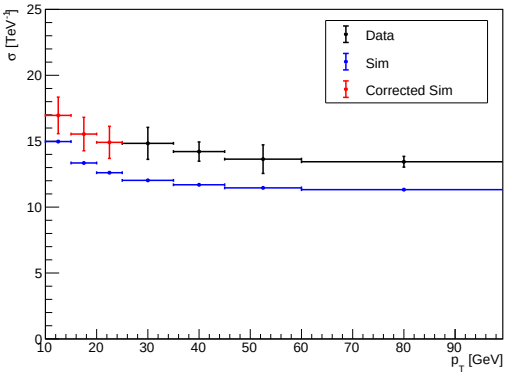

(b) **Muons**

Figure 50: The parameter σ as a function of the track p_{T}. Black points show measured values in data and blue points show MC. Red points show corrected MC values normalized to data in the $p_{\mathrm{T}} > 25$ GeV region by adding correction factors.

6 Search for Long-Lived Charginos with the Full Run-2 Data

In this chapter, a result of search for long-lived charginos based on a disappearing track signature with full Run-2 dataset is reported. First, the characteristics of the target signals and possible background sources are described. Next, the definition of the signal region and the selection efficiency of signal and background events for each event selection are summarized. Then, an overview of the overall analysis is given, followed by an estimation of each background components in the signal region. Finally, details of the fitting, which is the key to background event estimation, and systematic uncertainties are described. The actual fitting results and the results of the search for long-lived charginos calculated based on the fitting results are shown.

6.1 Signal and Background

6.1.1 Signature of the Signal

In this analysis, two production processes of charginos are considered: electroweak (EWK) production and strong production. Figure 51 shows schematic example diagrams for both production processes. In the EWK production, a chargino-chargino or chargino-neutralino pair is produced directly via electroweak boson. A high-momentum jet from initial-state radiation (ISR) is required so that events can be triggered by $E_{\mathrm{T}}^{\mathrm{miss}}$. Therefore the signature of the signal is a single large jet from ISR, a large $E_{\mathrm{T}}^{\mathrm{miss}}$ due to neutralinos, and a disappearing track candidate derived from chargino. In the strong production, the gluino pair is produced and then each gluino decays into two quarks and a chargino or neutralino.

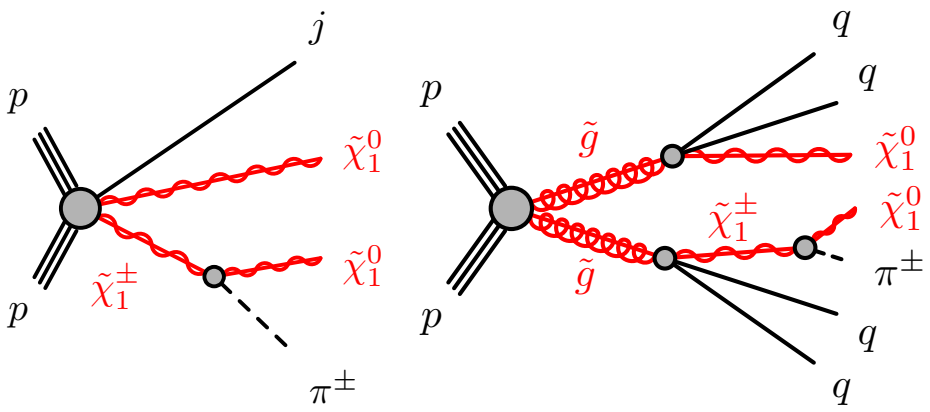

(a) EWK production (b) Strong production

Figure 51: Example diagrams of the two signal models

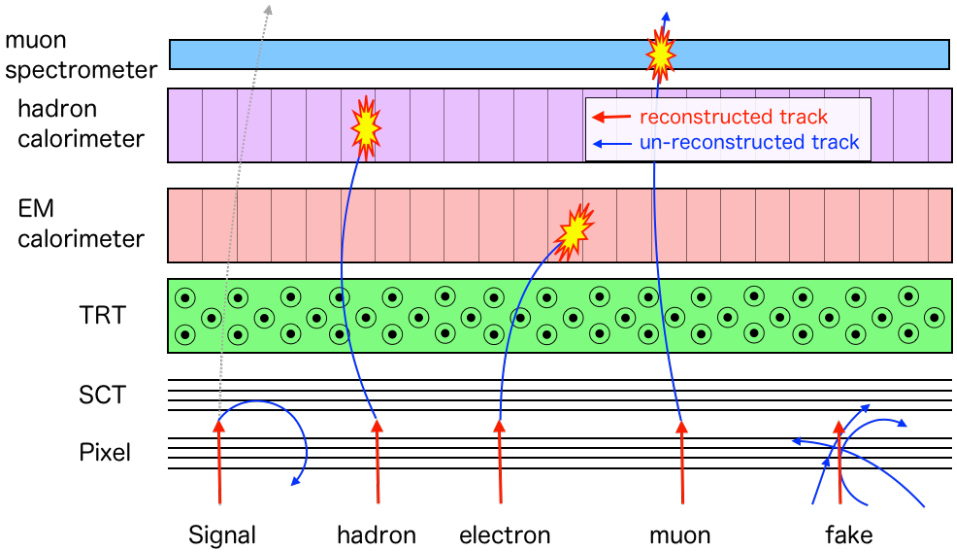

Figure 52: Components of pixel-tracks

So the signature of the signal is multi-jets from quarks or gluons, a large $E_{\mathrm{T}}^{\mathrm{miss}}$ from neutralinos, and a disappearing track candidate derived from the chargino.

6.1.2 Background Components

The backgrounds contributing to this analysis can be categorized into real charged-particle backgrounds and fake backgrounds. Figure 52 illustrates how the signals and backgrounds are reconstructed as a pixel-track. The charged particle backgrounds arise from scattering by interacting with materials or emitting bremsstrahlung after passing through four-pixel layers. Muon originated background can be suppressed by muon spectrometer veto. Electron or hadron originated background can also be suppressed by calorimeter veto requirements. Fake backgrounds arise from wrongly reconstructed random combinations of pixel hits. Since fake background has an unreal track that is not associated with any other objects, it is hard to reduce by isolation cuts. The dominant SM process is $W \to \ell\nu$ for the charged particle backgrounds and $Z \to \nu\nu$ for the fake backgrounds.

6.1.3 Signal Region Definitions

Signal candidate events are required to pass the $E_{\mathrm{T}}^{\mathrm{miss}}$ triggers for both the EWK and the strong channels. Events are also required to have neither muons nor electrons candidates (i.e. lepton-veto) to suppress the backgrounds from the top-pair and W/Z + jets production processes. In addition to the requirements of high-$E_{\mathrm{T}}^{\mathrm{miss}}$ and high-p_{T} jets, the minimum $\Delta\phi^{\mathrm{jet}-E_{\mathrm{T}}^{\mathrm{miss}}}$ cut is also applied to reduce the QCD backgrounds.

Table 6: Signal region selection summary

SR	Electroweak production	Strong production
Trigger	$E_{\mathrm{T}}^{\mathrm{miss}}$	
$\mathrm{N}_{\mathrm{lepton}}$	$= 0$	
$\mathrm{N}_{\mathrm{disap.-track}}$	≥ 1	
$E_{\mathrm{T}}^{\mathrm{miss}}$ [GeV]	> 200	> 250
Leading jet p_{T} [GeV]	> 100	> 100
Second and third jet p_{T} [GeV]	—	> 20
$\Delta\phi_{\mathrm{min}}^{\mathrm{jet}-E_{\mathrm{T}}^{\mathrm{miss}}}$ [radian]	> 1.0	> 0.4

Finally, at least one pixel-track that satisfies all selections in Section 4.2 is required. In cases that more than one such pixel-track exist, the one with the highest p_{T} among isolated pixel-tracks is chosen. The selections for the EWK channel and the strong channel are not exclusive, so there might be overlap events. It does not matter because the analysis is performed individually in each channel, and the results are not planned to be combined. Selections of the signal region are summarized in Table 6.

6.2 Analysis Overview

Signatures of the signals and possible background components are summarized in Section 6.1, and the event selection for the signal region is defined in the previous subsection. As shown in Figure 39, the signal charginos tend to have high-p_{T}, while background tracks typically have low-p_{T}. Therefore, the p_{T} of the pixel-track becomes the final discriminant variable. After the event selections, observed p_{T} distributions are fitted with expected background shapes to estimate number of background events in the signal region. In this section, an overview of analysis strategy, especially how to estimate the p_{T} spectra of the signals and each background component in the signal region, is summarized. Detail information on individual items follows in later sections.

Figure 53 illustrates how to estimate the p_{T} spectra in the signal region. Control Region (CR) is a region with low signal contamination and high purity for specific background, therefore it is useful to estimate background properties. Events in CRs basically satisfy both kinematics and track selections except for specific requirements. Definitions of each background CR are summarized in Table 7.

For the signal events, smearing function measured in data is applied to emulate realistic detector resolution. The nominal normalization is fixed, but the signal can scale with the signal strength μ_s during the fitting with the signal model. For the muon, electron, and hadron backgrounds, the CRs are

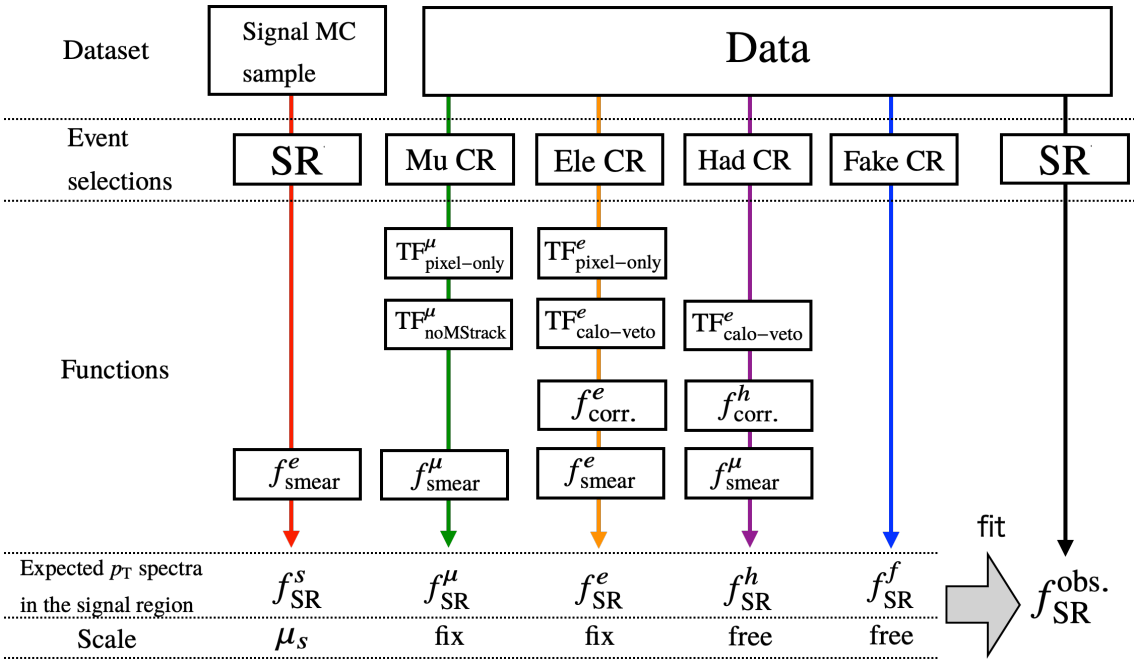

Figure 53: Analysis strategy

defined by requiring each background object instead of a disappearing pixel-track. Therefore, transfer factors (TFs) which are the ratio of a disappearing track to the background object are applied to obtain mother spectra of disappearing tracks derived from each background component. For the electron and hadron backgrounds, correction factors for the TF are required to correct the difference between electrons and hadrons, and also standard tracks and pixel-tracks. These correction factors are calculated by using single particle MC samples. Details are described in Section 6.4.2. Then smearing functions measured in Section 5.4 are applied to the background events to emulate the p_{T} resolution of pixel-tracks from standard tracks. Impacts on the p_{T} shapes are dominant from the events in the CR and smearing function, while impacts on the normalizations are dominant from the original events in the CR and TFs. For the fake background, the p_{T} shape is nearly independent of d_0 significance, so the p_{T} spectra in the signal region is directly estimated from the Fake CR. Once the p_{T} spectra of each background component are obtained, the amount of each background event in the signal region is estimated by fitting observed p_{T} distribution. Normalizations of the hadron and fake backgrounds are free parameters in

Region name	$E_{\mathrm{T}}^{\mathrm{miss}}$	Alternative object to a disappearing track
Ele CR	e-subtracted $E_{\mathrm{T}}^{\mathrm{miss}}$	electron
Mu CR	μ-subtracted $E_{\mathrm{T}}^{\mathrm{miss}}$	muon
Had CR	standard $E_{\mathrm{T}}^{\mathrm{miss}}$	hadron like track
Fake CR	no $E_{\mathrm{T}}^{\mathrm{miss}}$ requirement	pixel-track with $\lvert d_0/\mathrm{err}(d_0)\rvert > 10$

Table 7: Definition of CRs

the fitting. Details of the fitting procedure is described in Section 6.5.

6.3 Event Selection Summary

In this section, write out each event selection and show how the signal and background events look like. For convenience, the definitions of some specific requirements and regions are summarized in Table 8. Signal events tend to have high-p_{T} and high-$E_{\mathrm{T}}^{\mathrm{miss}}$. Therefore, events in the low-p_{T} region are background dominant even in the high-$E_{\mathrm{T}}^{\mathrm{miss}}$ region. Events in the low-$E_{\mathrm{T}}^{\mathrm{miss}}$ region are also background dominant even in the high-p_{T} region. The fraction of the fake background among background components is relatively low in the low-p_{T} region, while it is high in the high-p_{T} region. The very low-$E_{\mathrm{T}}^{\mathrm{miss}}$ region is included only in the Fake-CR. The middle-$E_{\mathrm{T}}^{\mathrm{miss}}$ and calo-sideband regions are used for the validation of the fitting method.

6.3.1 Trigger

The trigger efficiency might be different between data and simulation due to mismodeling of trigger simulation. To estimate the number of signal events correctly, it is important to measure the trigger efficiency in data and apply it to the signal MC events. Three types of triggers are used for this analysis: the $E_{\mathrm{T}}^{\mathrm{miss}}$ triggers, single-muon triggers, and single-electron triggers. The $E_{\mathrm{T}}^{\mathrm{miss}}$ triggers are the main trigger, while the single-muon triggers and the single-electron triggers are only used to calculate $E_{\mathrm{T}}^{\mathrm{miss}}$ trigger efficiencies and to estimate transfer factors. Due to changing pile-up conditions across the data-taking periods, the algorithm or the threshold of triggers are also modified to keep the trigger rates acceptable. The threshold of p_{T} for muons and electrons at the HLT is varying from 20 GeV to 26 GeV

Region name	Requirements
low-p_{T}	20 GeV $< p_{\mathrm{T}} <$ 60 GeV
high-p_{T}	60 GeV $< p_{\mathrm{T}}$
very low-$E_{\mathrm{T}}^{\mathrm{miss}}$	$E_{\mathrm{T}}^{\mathrm{miss}} <$ 100 GeV
low-$E_{\mathrm{T}}^{\mathrm{miss}}$	100 GeV $< E_{\mathrm{T}}^{\mathrm{miss}} <$ 150 GeV
middle-$E_{\mathrm{T}}^{\mathrm{miss}}$	150 GeV $< E_{\mathrm{T}}^{\mathrm{miss}} <$ 200 GeV
high-$E_{\mathrm{T}}^{\mathrm{miss}}$	200 GeV $< E_{\mathrm{T}}^{\mathrm{miss}}$ for the EWK channel 250 GeV $< E_{\mathrm{T}}^{\mathrm{miss}}$ for the strong channel
calo-veto	$E_{\mathrm{T}}^{\mathrm{topoclus20}} <$ 5 GeV
calo-sideband	5 GeV $< E_{\mathrm{T}}^{\mathrm{topoclus20}} <$ 10 GeV

Table 8: Definition of specific requirements

Data Period	Run Number	Trigger Name
2015 D–J	[276262, 284484]	HLT_xe70_mht
2016 A3–D3	[297730, 302872]	HLT_xe90_mht_L1XE50
2016 D4–F1	[302919, 303892]	HLT_xe100_mht_L1XE50
2016 F2–L11	[303943, 311481]	HLT_xe110_mht_L1XE50
2017 B1–D5	[325713, 331975]	HLT_xe110_pufit_L1XE55
2017 D6–K6	[332303, 340453]	HLT_xe110_pufit_L1XE50
2018 B–C5	[348885, 350013]	HLT_xe110_pufit_xe70_L1XE50
2018 C5–Q2	[350067, 364292]	HLT_xe110_pufit_xe65_L1XE50

Table 9: The list of $E_{\mathrm{T}}^{\mathrm{miss}}$ triggers

for muons, and 24 GeV to 26 GeV for electrons, respectively. Since only the $E_{\mathrm{T}}^{\mathrm{miss}}$ trigger is important for this analysis, it is focused on the $E_{\mathrm{T}}^{\mathrm{miss}}$ trigger in this sub-section.

The $E_{\mathrm{T}}^{\mathrm{miss}}$ trigger chains of each data-taking period are summarized in Table 9. In this analysis, the $E_{\mathrm{T}}^{\mathrm{miss}}$ trigger efficiency is estimated using real data and applied to the signal MC events. Hence $W \to \mu\nu$ candidates are used to measure the trigger efficiency for the signal-like events in data. The following selections criteria are required to extract nearly pure $W \to \mu\nu$ events. The contribution of the muon to the $E_{\mathrm{T}}^{\mathrm{miss}}$ is subtracted so that events have a similar topology to the signal events.

- The muon triggers
- No identified electrons
- Exactly one reconstructed muon with $p_{\mathrm{T}} > 27$ GeV
- 30 GeV $< m_{\mathrm{T}} <$ 100 GeV, where m_{T} is defined as

$$m_{\mathrm{T}} = \sqrt{2\, p_{\mathrm{T}}^{\mu}\, E_{\mathrm{T}}^{\mathrm{miss}} \left[1 - \cos\Delta\phi(\mu, E_{\mathrm{T}}^{\mathrm{miss}})\right]} \tag{21}$$

- Same requirements for jet p_{T} and $\Delta\phi_{\mathrm{min}}^{\mathrm{jet},E_{\mathrm{T}}^{\mathrm{miss}}}$ as in the signal region described in Section 6.1.3

Then the trigger efficiency is calculated by the fraction of events passing the $E_{\mathrm{T}}^{\mathrm{miss}}$ trigger among the selected events as a function of the $E_{\mathrm{T}}^{\mathrm{miss}}$ and the leading jet p_{T}. Figure 54 shows the projection of the $E_{\mathrm{T}}^{\mathrm{miss}}$ trigger efficiencies to the $E_{\mathrm{T}}^{\mathrm{miss}}$ with different $E_{\mathrm{T}}^{\mathrm{miss}}$ triggers in data. The EWK channel and the strong channel share events and the difference is only requirements for second and third jet p_{T} and $\Delta\phi_{\mathrm{min}}^{\mathrm{jet}-E_{\mathrm{T}}^{\mathrm{miss}}}$. The efficiency is almost 100% with $E_{\mathrm{T}}^{\mathrm{miss}} > 200$ GeV for any $E_{\mathrm{T}}^{\mathrm{miss}}$ triggers in both channels.

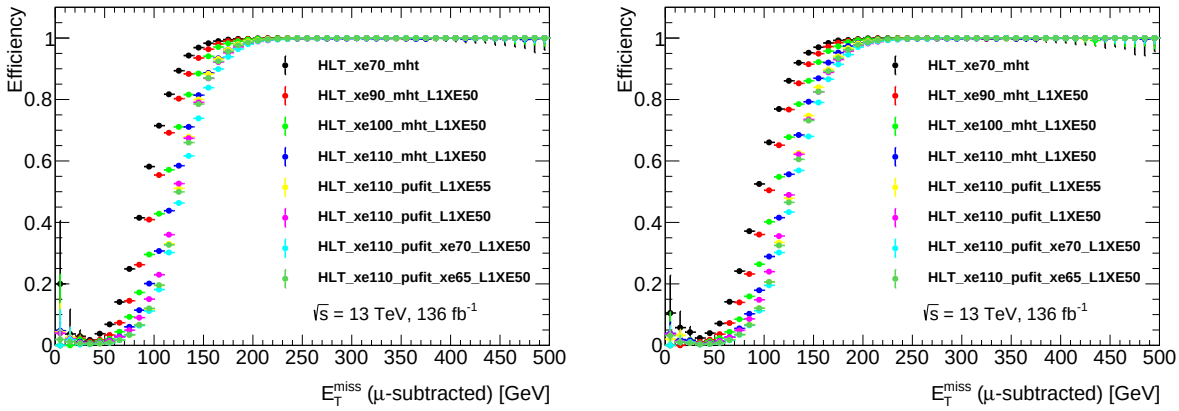

(a) Electroweak production

(b) Strong production

Figure 54: The $E_{\mathrm{T}}^{\mathrm{miss}}$ trigger efficiencies as a function of the $E_{\mathrm{T}}^{\mathrm{miss}}$ with different $E_{\mathrm{T}}^{\mathrm{miss}}$ triggers in data. In order to emulate the signal topology, the muon contribution is subtracted from $E_{\mathrm{T}}^{\mathrm{miss}}$.

6.3.2 Kinematic Distribution

Figure 55 and Figure 56 show kinematic distributions after all kinematical selections except for the target variable (N-1 plot). The di-jets MC samples have a large event weight and statistical error due to a lack of MC statistics, and the number of events is overestimated especially in the low-$E_{\mathrm{T}}^{\mathrm{miss}}$ region.

6.3.3 Cut-Flow Table

To clarify the meaning of each event selection, cut-flow tables for background events and signal events are shown in Table 10 and 11 for the electroweak channel, and Table 12 and Table 13 for the strong channel respectively. For the data and SM background MC, a low-p_{T} pixel-track is required to enhance charged particle backgrounds. Values in the tables show the number of remaining events after sequential event selections and relative selection efficiencies. The correction of the pixel dead module map described in Section 6.4.1 for MC samples is not applied because it will give bias to each selection.

6.3.4 Calorimeter VETO

The main improvement of this analysis is a huge background reduction thanks to a calorimeter veto requirement. A variable $E_{\mathrm{T}}^{\mathrm{topoclus20}}$ is the sum of energies of all topological clusters within $\Delta R < 0.2$ from the track. Figure 57 shows the $E_{\mathrm{T}}^{\mathrm{topoclus20}}$ distribution for the background data and the signal MC. The distribution for the fake background is obtained from the Fake CR, therefore no $E_{\mathrm{T}}^{\mathrm{miss}}$ cut is applied. Others are required with $E_{\mathrm{T}}^{\mathrm{miss}} > 100$ GeV. The distribution for the muon background is obtained from

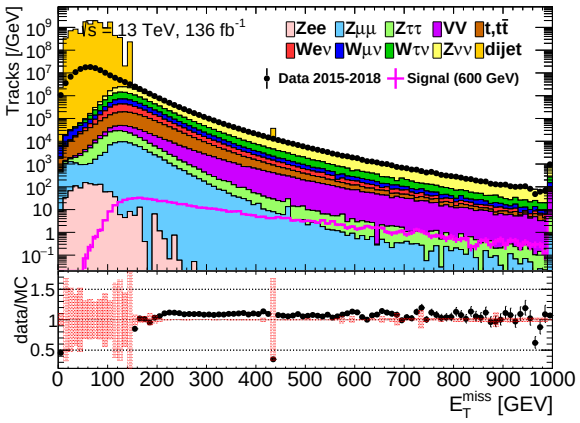

(a) $E_{\mathrm{T}}^{\mathrm{miss}}$

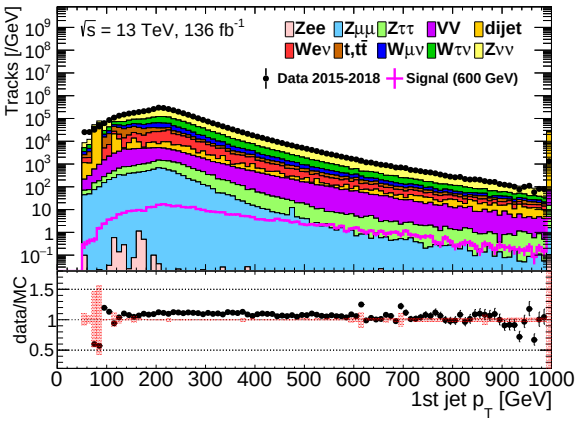

(b) 1st jet p_{T}

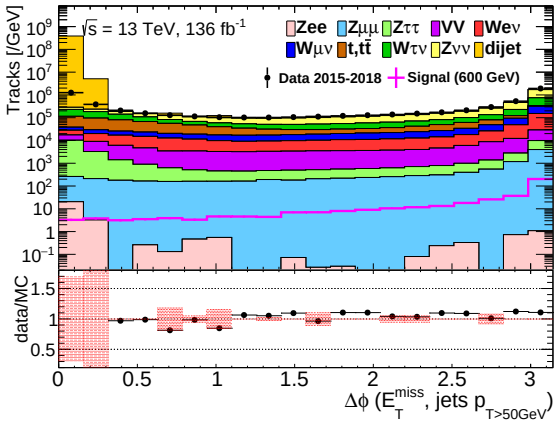

(c) $\Delta\phi_{\mathrm{min}}^{\mathrm{jet-E_T^{miss}}}$

Figure 55: Kinematic distributions after kinematics selections except on the target variable for the electroweak channel

the Mu CR, while the distribution for the electron/hadron background is obtained from the low-p_{T} CR. The signal track is isolated from calorimeter clusters, while the hadron and electron backgrounds tend to have energy deposits in calorimeters, typically correlated to their track p_{T}. So the requirement of a calorimeter veto can reduce these backgrounds drastically. The background components in the low-$E_{\mathrm{T}}^{\mathrm{topoclus20}}$ region are dominated by the fake background.

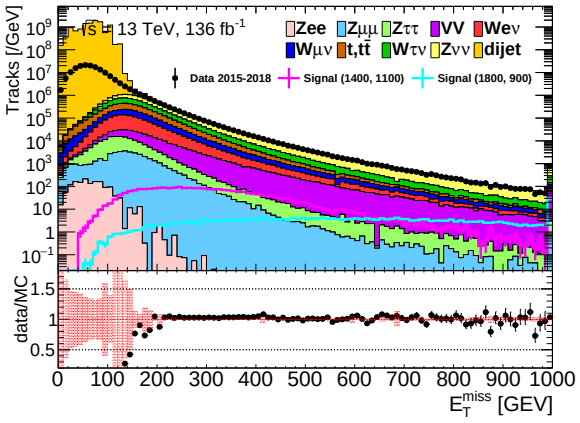

(a) $E_{\mathrm{T}}^{\mathrm{miss}}$

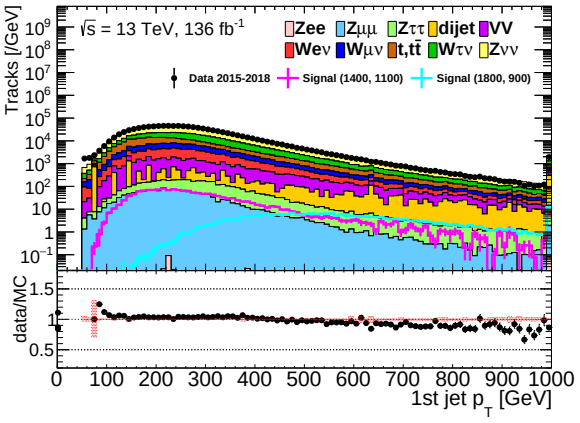

(b) 1st jet p_{T}

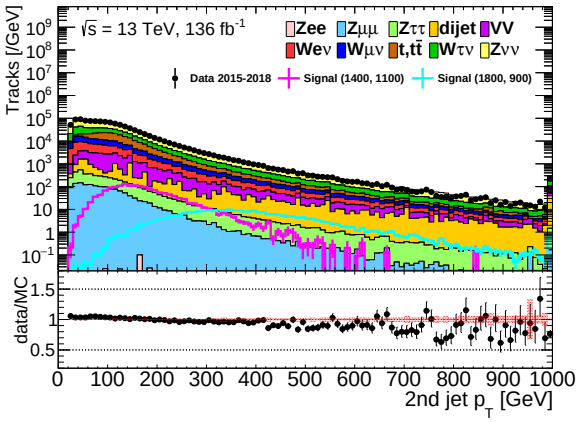

(c) 2nd jet p_{T}

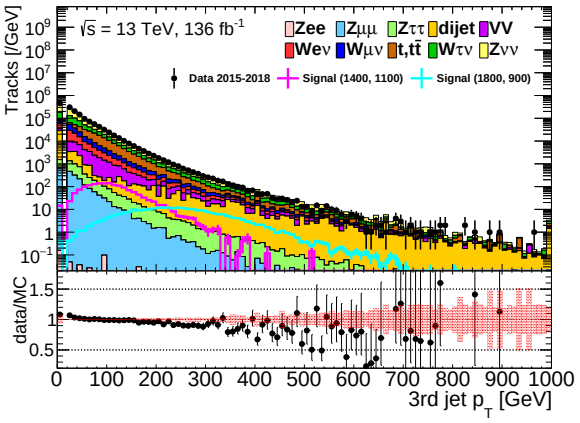

(d) 3rd jet p_{T}

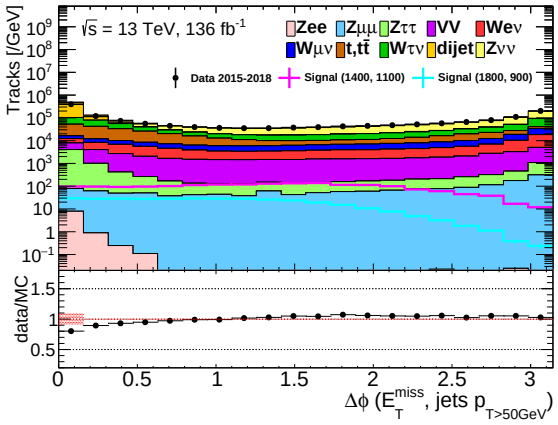

(e) $\Delta\phi_{\mathrm{min}}^{\mathrm{jet-E_T^{miss}}}$

Figure 56: Kinematic distributions after kinematics selections except on the target variable for the strong channel

	Observed (136.3 fb^{-1})		SM background (MC)	
Requirement	Events	Efficiency [%]	Events	Efficiency [%]
All events	4.50×10^9	-	$(1.86 \pm 0.02) \times 10^{12}$	-
GRL and event cleaning	2.05×10^9	46	$(1.13 \pm 0.01) \times 10^{12}$	61
$E_{\mathrm{T}}^{\mathrm{miss}}$ trigger	5.59×10^8	27	$(6.17 \pm 0.32) \times 10^{10}$	5
Lepton VETO	5.26×10^8	94	$(6.12 \pm 0.32) \times 10^{10}$	99
$E_{\mathrm{T}}^{\mathrm{miss}} > 200$ GeV	6.80×10^6	1	$(3.97 \pm 2.73) \times 10^8$	1
1st jet $p_{\mathrm{T}} > 100$ GeV	6.44×10^6	95	$(3.96 \pm 2.73) \times 10^8$	100
$\Delta\phi_{\mathrm{min}}^{\mathrm{jet-E_T^{miss}}} > 1.0$	4.16×10^6	65	$(3.83 \pm 0.03) \times 10^6$	1
low-p_T pixel-track	4.32×10^4	1	$(4.76 \pm 0.43) \times 10^4$	1
$N_{\mathrm{GangedFlaggedFakeHits}}^{\mathrm{Pixel}} = 0$	3.56×10^4	82	$(3.91 \pm 0.43) \times 10^4$	82
$N_{\mathrm{SpoiltHits}}^{\mathrm{Pixel}} = 0$	1.51×10^4	42	$(1.44 \pm 0.01) \times 10^4$	37
$N_{\mathrm{Outliers}}^{\mathrm{Pixel}} = 0$	1.51×10^4	100	$(1.43 \pm 0.01) \times 10^4$	99
$\lvert d_0\mathrm{significance}\rvert < 1.5$	5.05×10^3	34	$(5.94 \pm 0.09) \times 10^3$	42
$\lvert z_0 \sin\theta\rvert < 0.5$ mm	4.90×10^3	97	$(5.82 \pm 0.09) \times 10^3$	98
$p_{\mathrm{T}}^{\mathrm{cone40}}/p_{\mathrm{T}} < 0.04$	329	7	558 ± 25	10
Highest-p_{T} among isolated pixel-tracks	327	99	551 ± 25	99
ΔR(jets) > 0.4	326	100	539 ± 25	98
ΔR(MStrack) > 0.4	260	80	447 ± 21	83
Quality > 0.1	249	96	431 ± 21	96
$0.1 < \lvert\eta\rvert < 1.9$	223	90	362 ± 19	84
$E_{\mathrm{T}}^{\mathrm{topoclus20}} < 5.0$ GeV	11	5	8.0 ± 2.1	2

Table 10: Summary of event selection cuts for EWK production for the data and the SM background MC samples which are normalized to 136.3 fb^{-1}.

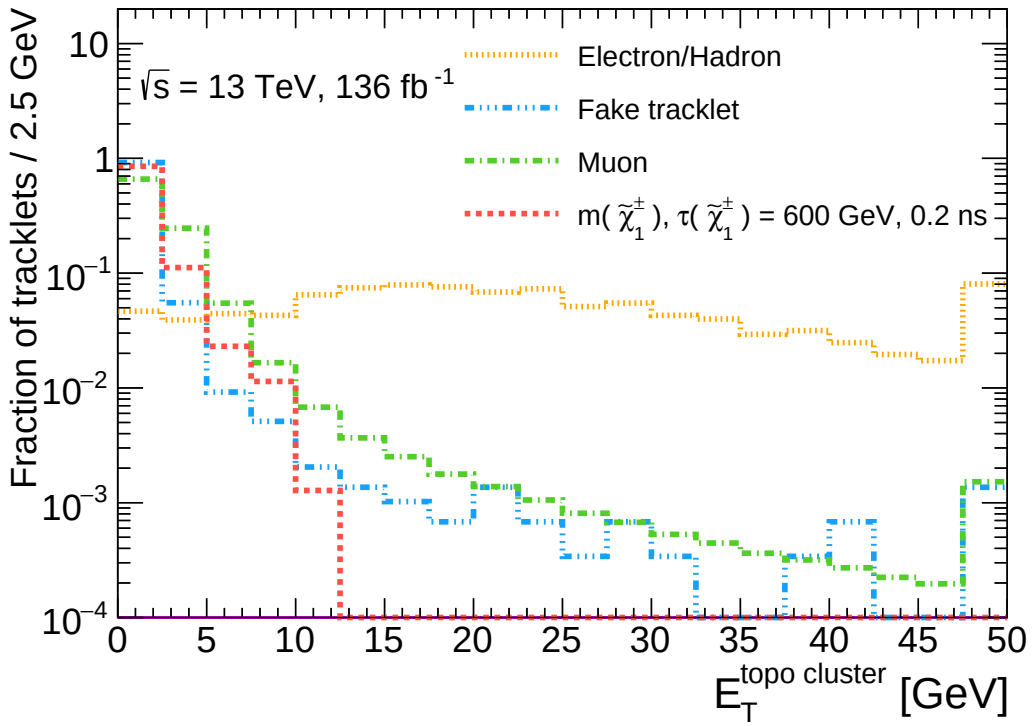

Figure 57: The $E_{\mathrm{T}}^{\mathrm{topoclus20}}$ distribution for each background component and the signal. Integrated entries of each histogram are normalized to 1. The last bin contains the overflow bin.

	Signal MC			
$(m_{\tilde{\chi}_1^\pm}, \tau_{\tilde{\chi}_1^\pm})$	(600 GeV, 0.2 ns)		(600 GeV , 1.0 ns)	
Requirement	Events at 136.3 fb^{-1}	(Efficiency [%])		
All events	1.57×10^3	(-)	1.58×10^3	(-)
GRL and event cleaning	1.38×10^3	(88)	1.40×10^3	(89)
$E_{\mathrm{T}}^{\mathrm{miss}}$ trigger	737	(53)	734	(52)
Lepton VETO	735	(100)	733	(100)
$E_{\mathrm{T}}^{\mathrm{miss}} > 200$ GeV	395	(54)	391	(53)
1st jet $p_{\mathrm{T}} > 100$ GeV	390	(99)	385	(99)
$\Delta\phi_{\mathrm{min}}^{\mathrm{jet-E_T^{miss}}} > 1.0$	367	(94)	362	(94)
pixel-track	20.8	(6)	56.8	(16)
$N_{\mathrm{GangedFlaggedFakeHits}}^{\mathrm{Pixel}} = 0$	19.5	(94)	56.2	(99)
$N_{\mathrm{SpoiltHits}}^{\mathrm{Pixel}} = 0$	17.6	(90)	53.0	(94)
$N_{\mathrm{Outliers}}^{\mathrm{Pixel}} = 0$	17.6	(100)	53.0	(100)
$\lvert d_0\mathrm{significance}\rvert < 1.5$	16.1	(92)	50.2	(95)
$\lvert z_0 \sin\theta\rvert < 0.5$ mm	16.1	(100)	50.2	(100)
$p_{\mathrm{T}}^{\mathrm{cone40}}/p_{\mathrm{T}} < 0.04$	14.9	(93)	47.7	(95)
Highest-p_{T} among isolated pixel-tracks	14.9	(100)	46.8	(98)
$\Delta R(\mathrm{jets}) > 0.4$	14.9	(100)	46.8	(100)
$\Delta R(\mathrm{MStrack}) > 0.4$	14.8	(100)	46.4	(99)
Quality > 0.1	14.8	(100)	45.6	(98)
$0.1 < \lvert\eta\rvert < 1.9$	13.7	(93)	43.1	(95)
$E_{\mathrm{T}}^{\mathrm{topoclus20}} < 5.0$ GeV	13.7	(100)	42.9	(99)

Table 11: Summary of event selection cuts for EWK production for the signal samples which are normalized to 136.3 fb^{-1}.

	Observed (136.3 fb^{-1})		SM background (MC)	
Requirement	Events	Efficiency [%]	Events	Efficiency [%]
All events	4.50×10^9	-	$(1.86 \pm 0.02) \times 10^{12}$	-
GRL and event cleaning	2.05×10^9	46	$(1.13 \pm 0.01) \times 10^{12}$	61
$E_{\mathrm{T}}^{\mathrm{miss}}$ trigger	5.59×10^8	27	$(6.17 \pm 0.32) \times 10^{10}$	5
Lepton VETO	5.26×10^8	94	$(6.12 \pm 0.32) \times 10^{10}$	99
$E_{\mathrm{T}}^{\mathrm{miss}} > 250$ GeV	2.45×10^6	0	$(1.57 \pm 1.40) \times 10^8$	0
1st jet $p_{\mathrm{T}} > 100$ GeV	2.42×10^6	99	$(1.57 \pm 1.40) \times 10^8$	100
2nd jet $p_{\mathrm{T}} > 20$ GeV	2.14×10^6	89	$(1.56 \pm 1.40) \times 10^8$	99
3rd jet $p_{\mathrm{T}} > 20$ GeV	1.62×10^6	75	$(1.70 \pm 0.04) \times 10^6$	1
$\Delta\phi_{\mathrm{min}}^{\mathrm{jet-E_T^{miss}}} > 0.4$	1.06×10^6	65	$(1.03 \pm 0.00) \times 10^6$	61
low-p_T pixel-track	1.22×10^4	1	$(1.33 \pm 0.01) \times 10^4$	1
$N_{\mathrm{GangedFlaggedFakeHits}}^{\mathrm{Pixel}} = 0$	1.02×10^4	83	$(1.09 \pm 0.01) \times 10^4$	82
$N_{\mathrm{SpoiltHits}}^{\mathrm{Pixel}} = 0$	4.66×10^4	46	$(4.80 \pm 0.05) \times 10^3$	44
$N_{\mathrm{Outliers}}^{\mathrm{Pixel}} = 0$	4.64×10^4	100	$(4.77 \pm 0.05) \times 10^3$	99
$\lvert d_0\mathrm{significance}\rvert < 1.5$	1.79×10^3	39	$(2.18 \pm 0.04) \times 10^3$	46
$\lvert z_0 \sin\theta\rvert < 0.5$ mm	1.75×10^3	98	$(2.14 \pm 0.04) \times 10^3$	98
$p_{\mathrm{T}}^{\mathrm{cone40}}/p_{\mathrm{T}} < 0.04$	86	5	159 ± 9.8	7
Highest-p_{T} among isolated pixel-tracks	86	100	157 ± 9.8	99
ΔR(jets) > 0.4	85	99	148 ± 9.6	94
ΔR(MStrack) > 0.4	70	82	114 ± 8.6	77
Quality > 0.1	67	96	112 ± 8.5	98
$0.1 < \lvert\eta\rvert < 1.9$	64	96	93.0 ± 8.1	83
$E_{\mathrm{T}}^{\mathrm{topoclus20}} < 5.0$ GeV	1	2	2.40 ± 0.84	3

Table 12: Summary of event selection cuts for the strong production for data and SM background MC samples normalized to 136.3 fb^{-1}.

	Signal MC							
$(m_{\tilde{g}}, m_{\tilde{\chi}_1^\pm})$	(1400 GeV, 1100 GeV)				(1800 GeV, 900 GeV)			
$\tau_{\tilde{\chi}_1^\pm}$	0.2 ns		1.0 ns		0.2 ns		1.0 ns	
Requirement	Events at 136.3 fb^{-1} (Efficiency [%])							
All events	3.50×10^3	(100)	3.51×10^3	(100)	394	(100)	394	(100)
GRL and event cleaning	3.44×10^3	(98)	3.45×10^3	(98)	390	(99)	389	(99)
$E_{\mathrm{T}}^{\mathrm{miss}}$ trigger	3.25×10^3	(94)	3.26×10^3	(94)	384	(98)	383	(98)
Lepton VETO	3.23×10^3	(100)	3.25×10^3	(100)	380	(99)	380	(99)
$E_{\mathrm{T}}^{\mathrm{miss}} > 250$ GeV	1.82×10^3	(56)	1.85×10^3	(57)	342	(90)	342	(90)
1st jet $p_{\mathrm{T}} > 100$ GeV	1.82×10^3	(100)	1.85×10^3	(100)	342	(100)	342	(100)
2nd jet $p_{\mathrm{T}} > 20$ GeV	1.82×10^3	(100)	1.85×10^3	(100)	342	(100)	342	(100)
3rd jet $p_{\mathrm{T}} > 20$ GeV	1.81×10^3	(99)	1.83×10^3	(99)	342	(100)	341	(100)
$\Delta\phi_{\mathrm{min}}^{\mathrm{jet-E_T^{miss}}} > 0.4$	1.56×10^3	(86)	1.58×10^3	(86)	268	(78)	267	(78)
pixel-track	55.2	(4)	258	(16)	14.4	(5)	44.6	(17)
$N_{\mathrm{GangedFlaggedFakeHits}}^{\mathrm{Pixel}} = 0$	51.0	(92)	255	(99)	13.6	(95)	44.0	(99)
$N_{\mathrm{SpoiltHits}}^{\mathrm{Pixel}} = 0$	43.3	(85)	242	(95)	12.0	(88)	41.9	(95)
$N_{\mathrm{Outliers}}^{\mathrm{Pixel}} = 0$	43.3	(100)	241	(100)	12.0	(100)	41.8	(100)
$\lvert d_0\mathrm{significance}\rvert < 1.5$	39.2	(91)	228	(95)	11.1	(93)	39.6	(95)
$\lvert z_0 \sin\theta\rvert < 0.5$ mm	39.2	(100)	228	(100)	11.1	(100)	39.6	(100)
$p_{\mathrm{T}}^{\mathrm{cone40}}/p_{\mathrm{T}} < 0.04$	27.5	(70)	190	(83)	8.6	(77)	34.2	(87)
Highest-p_{T} among isolated pixel-tracks	27.5	(100)	185	(97)	8.5	(99)	33.5	(98)
$\Delta R(\mathrm{jets}) > 0.4$	27.3	(99)	184	(99)	8.4	(99)	33.4	(100)
$\Delta R(\mathrm{MStrack}) > 0.4$	26.4	(97)	181	(98)	8.4	(99)	33.1	(99)
Quality > 0.1	26.1	(99)	179	(99)	8.3	(99)	32.7	(99)
$0.1 < \lvert\eta\rvert < 1.9$	23.3	(89)	166	(93)	7.4	(90)	29.8	(91)
$E_{\mathrm{T}}^{\mathrm{topoclus20}} < 5.0$ GeV	23.3	(100)	164	(99)	7.4	(99)	29.5	(99)

Table 13: Summary of event selection cuts for strong production for signal samples normalized to 136.3 fb^{-1}.

6.4 Background Estimation

As shown in Figure 39, the signal charginos have high-p_{T}, while the charged-particle backgrounds tend to have low-p_{T} due to the calorimeter-veto or other isolation requirements. So the p_{T} of a pixel-track is used as the final discriminant variable. In this analysis, backgrounds are strongly affected by detector conditions, so the p_{T} spectra of each background component must be estimated in a data-driven way. Then the p_{T} shape fitting is performed to the observed data to estimate the number of background events.

The estimation method of the p_{T} spectra is different for the charged-particle backgrounds and for the fake backgrounds. For the charged-particle backgrounds, transfer factors from standard objects (e.g. muon, electron) to disappearing tracks are measured, and then applied to the events in CRs to obtain the p_{T} spectra. Fake backgrounds arise from random combinations of pixel hits, so they tend to have large impact parameters compared to the charged-particle backgrounds. The p_{T} spectra of the fake backgrounds are directly obtained from the fake-rich large impact parameter region.

6.4.1 Muon Background

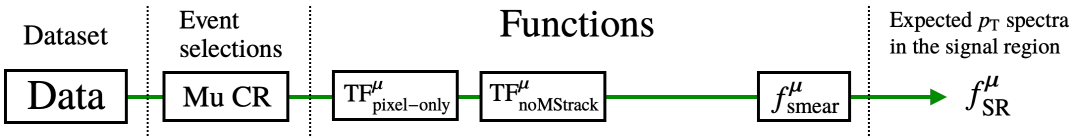

Figure 58: Overview for muon background estimation.

Muons can be classified as disappearing tracks due to energy loss by scattering in the inner detector material before reaching the SCT detector, or passing through inactive regions in the SCT modules or the muon spectrometers (MS). For the muon background template, first, the p_{T} spectrum of tracks is obtained by requiring almost the same selections as in the signal region except for a requirement of one muon instead of a disappearing track as single-muon control region (Mu-CR). Then transfer factors, which are factors of a muon being identified as a disappearing track, is applied. Finally, the muon p_{T} template distribution is obtained by smearing the track p_{T}.

- Definition of the Mu-CR

The Mu-CR is defined by the following requirements:

— The same kinematic-selection criteria are required as for the signal region, but exactly one muon is required. Here, $E_{\mathrm{T}}^{\mathrm{miss}}$ is calculated as if the leading muon was not identified.

— The ID track corresponding to the muon satisfies the same track selection requirements as in the signal region except for a track p_{T} threshold of 10 GeV instead of 20 GeV, and neither requiring $N_{\mathrm{SCT}} = 0$, the highest p_{T}, $\Delta R(\mathrm{muon}, \mathrm{IDtrack}) > 0.4$ nor $\Delta R(\mathrm{MStrack}, \mathrm{IDtrack}) > 0.4$.

- Measurements of $\mathrm{TF}^{\mu}_{\mathrm{pixel-only}}$ and $\mathrm{TF}^{\mu}_{\mathrm{noMStrack}}$

The transfer factor $\mathrm{TF}^{\mu}_{\mathrm{pixel-only}}$ is the factor that ID track of muon is identified as a disappearing track. The transfer factor $\mathrm{TF}^{\mu}_{\mathrm{noMStrack}}$ is the factor that the muon with a good ID track misses the MS track requirement. Transfer factors are measured by using $Z \to \mu\mu$ events with the tag and probe method. To enhance $Z \to \mu\mu$ events, the muon triggers, no identified electrons, at least one tag muon, at least one probe muon, and $|m_{\mathrm{tag,probe}} - m_Z| < 10$ GeV are required. The definitions of tag muon and probe muon are described as follows.

Definition of tag muons :

- Reconstructed muons matched to the trigger objects.
- Satisfying signal-muon criteria.
- $p_T > 30$ GeV.

Definition of probe muons for $\mathrm{TF}^{\mu}_{\mathrm{pixel-only}}$ measurement :

- MS track with associated ID track within $\Delta R < 0.2$.
- MS track with $p_{\mathrm{T}} > 10$ GeV and $|\eta| < 2.5$.
- Associated ID track which satisfies same track criteria as in the Mu-CR except for $p_{\mathrm{T}} > 10$ GeV.

Definition of probe muons for $\mathrm{TF}^{\mu}_{\mathrm{noMStrack}}$ measurement :

- ID track satisfies same track selections as in the Mu-CR except for $p_{\mathrm{T}} > 10$ GeV and additional requirement for $N_{\mathrm{SCT}} > 5$

Then the transfer factors $\mathrm{TF}^{\mu}_{\mathrm{pixel-only}}$ and $\mathrm{TF}^{\mu}_{\mathrm{noMStrack}}$ are obtained as

$$\mathrm{TF}^{\mu}_{\mathrm{pixel-only}}(p_{\mathrm{T}}, \eta) = N_{\mathrm{pixel-only}}(p_{\mathrm{T}}, \eta)/N_{\mathrm{muon}}(p_{\mathrm{T}}, \eta), \quad (22)$$

$$\mathrm{TF}^{\mu}_{\mathrm{noMStrack}}(\eta, \phi) = N_{\mathrm{noMStrack}}(\eta, \phi)/N_{\mathrm{MStrack}}(\eta, \phi), \quad (23)$$

where $N_{\mathrm{pixel-only}}$ is the number of probe muons satisfying $N_{\mathrm{SCT}} = 0$, N_{muon} is the number of probe muons identified as good muons, $N_{\mathrm{noMStrack}}$ is the number of probe ID tracks not having a MS track and N_{MStrack} is the number of probe ID tracks having a MS track. In order to subtract contributions from fake tracks, same sign (SS) events are subtracted from opposite sign (OS) events by using the sign of the tag muon and the probe track.

Figure 59 and Figure 60 show the reconstructed dimuon mass distributions for the $\mathrm{TF}^{\mu}_{\mathrm{pixel-only}}$ and $\mathrm{TF}^{\mu}_{\mathrm{noMStrack}}$ measurements, respectively. Only events satisfying $|m_{\mathrm{tag,probe}} - m_Z| < 10$ GeV are used for the calculation of the transfer factors. There is a Z mass peak in the SS pixel-only track category for $\mathrm{TF}^{\mu}_{\mathrm{pixel-only}}$ measurement because the probe track is short and the probability of charge flip is high. Figure 61 shows the transfer factor $\mathrm{TF}^{\mu}_{\mathrm{pixel-only}}$, it has only 10 bins due to the lack of statistics. Figure 62 (a) shows the mean value of the transfer factor $\mathrm{TF}^{\mu}_{\mathrm{noMStrack}}$ and Figure 62 (b) shows its statistical error. Since the $\mathrm{TF}^{\mu}_{\mathrm{noMStrack}}$ is almost independent of p_{T}, it is measured in the $\eta - \phi$ plane. The statistic uncertainty for the TF is evaluated by comparing PDF by using nominal TF values and 1σ shifted TF values. It is taken as an uncertainty for the normalization of muon background.

- Muon p_{T} template

Finally, the muon p_{T} template can be obtained by applying $\mathrm{TF}^{\mu}_{\mathrm{pixel-only}}$, $\mathrm{TF}^{\mu}_{\mathrm{noMStrack}}$, and the smearing function to the events in the Mu-CR. Figure 63 and Figure 64 show $N^{\mathrm{CR}}_{\mu,\mathrm{signal}}$ and f^{μ}_{SR} in the EWK and the strong channels, respectively.

6.4.2 Electron Background

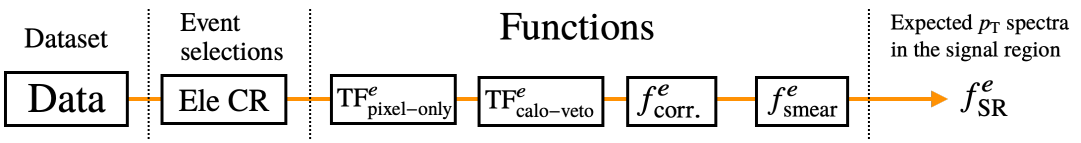

Figure 65: Overview for electron background estimation.

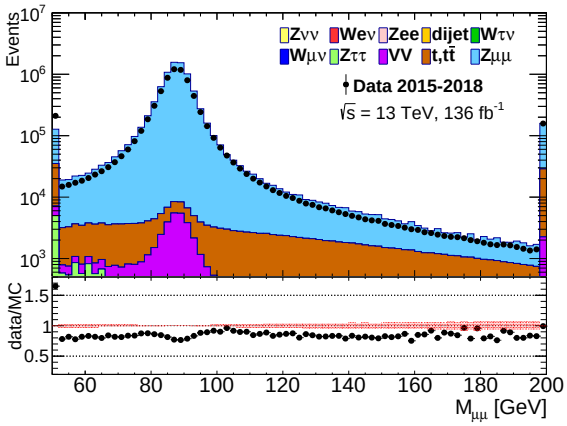

(a) Good muon category (OS)

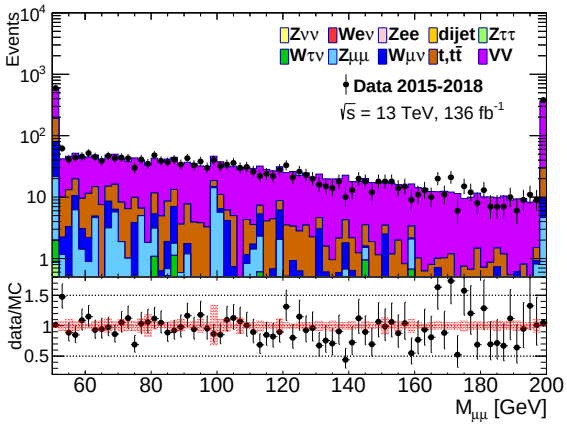

(b) Good muon category (SS)

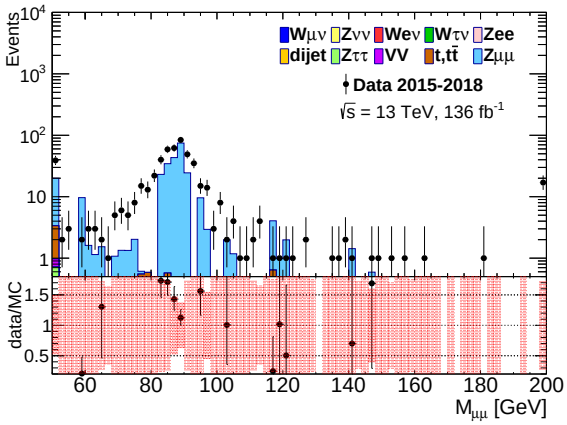

(c) Pixel-only track category (OS)

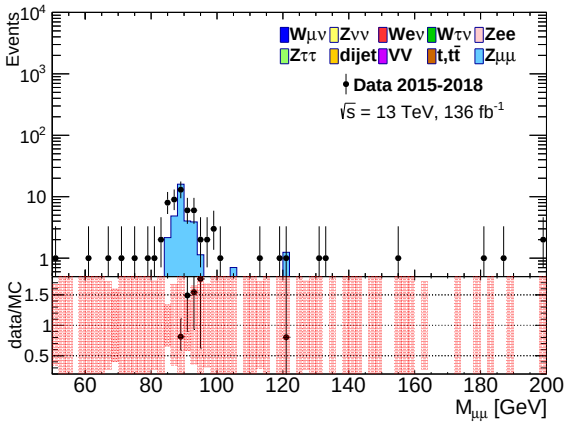

(d) Pixel-only track category (SS)

Figure 59: Reconstructed dimuon mass distribution for $\mathrm{TF}^{\mu}_{\mathrm{pixel-only}}$ measurement.

Electrons can be classified as disappearing tracks due to energy loss by bremsstrahlung, scattering in the inner detector material before reaching the SCT detector, or passing through inactive regions in the SCT modules. The basic strategy to obtain the p_{T} template for the electron background is the same as that for the muon background.

- Definition of the Ele-CR

The Ele-CR is defined by the following requirements:

— The same kinematic selection requirements as for the signal region, but requiring exactly one electron. Here, $E_{\mathrm{T}}^{\mathrm{miss}}$ is calculated as if the leading electron is not identified.

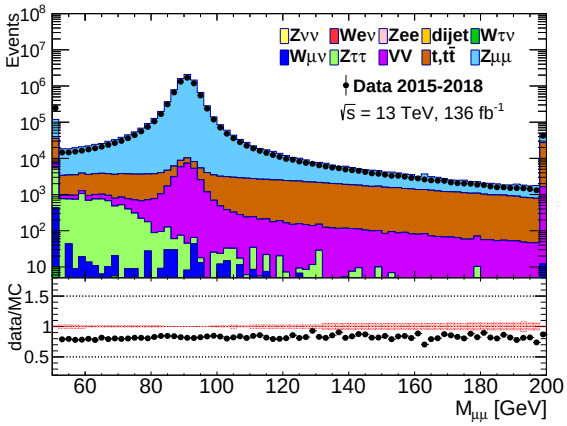

(a) MS track category (OS)

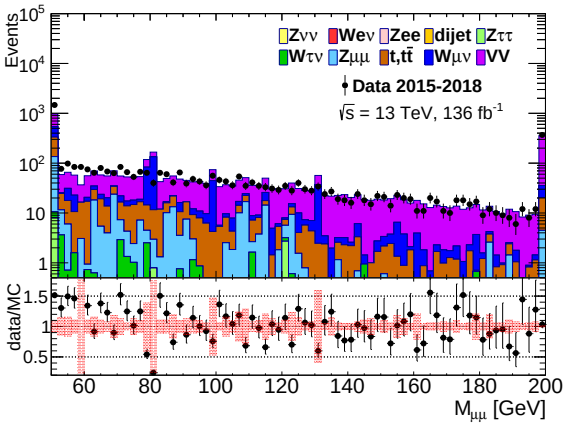

(b) MS track category (SS)

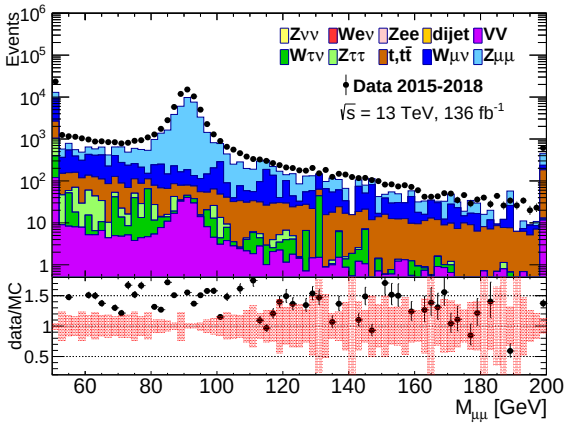

(c) No MS track category (OS)

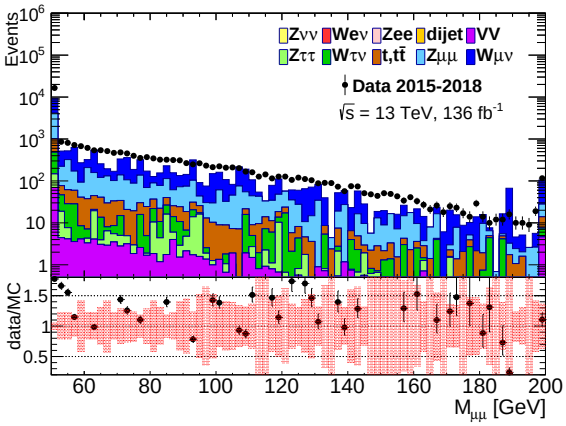

(d) No MS track category (SS)

Figure 60: Reconstructed dimuon mass distribution for $TF^{\mu}_{\text{noMStrack}}$ measurement.

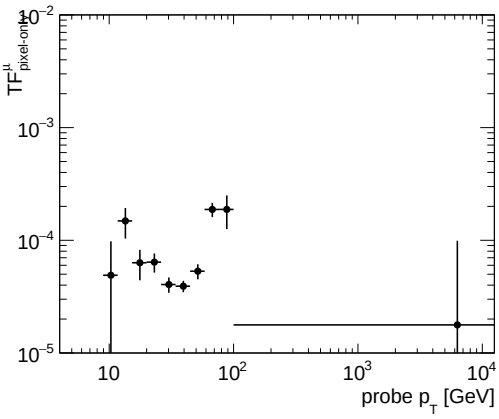

Figure 61: Transfer factor $TF^{\mu}_{\text{pixel-only}}$ for muon backgrounds

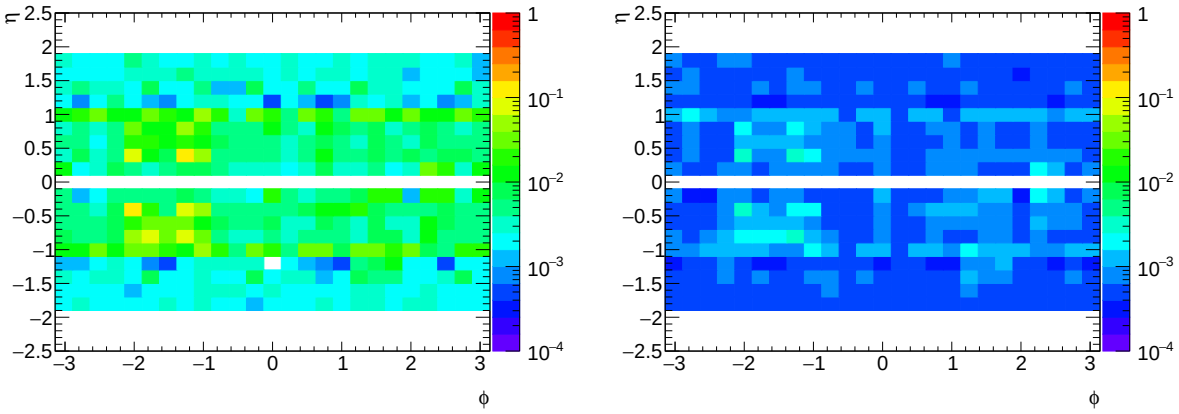

(a) Mean value (b) Statistical error

Figure 62: Transfer factor $\mathrm{TF}^{\mu}_{\mathrm{noMStrack}}$ for muon backgrounds

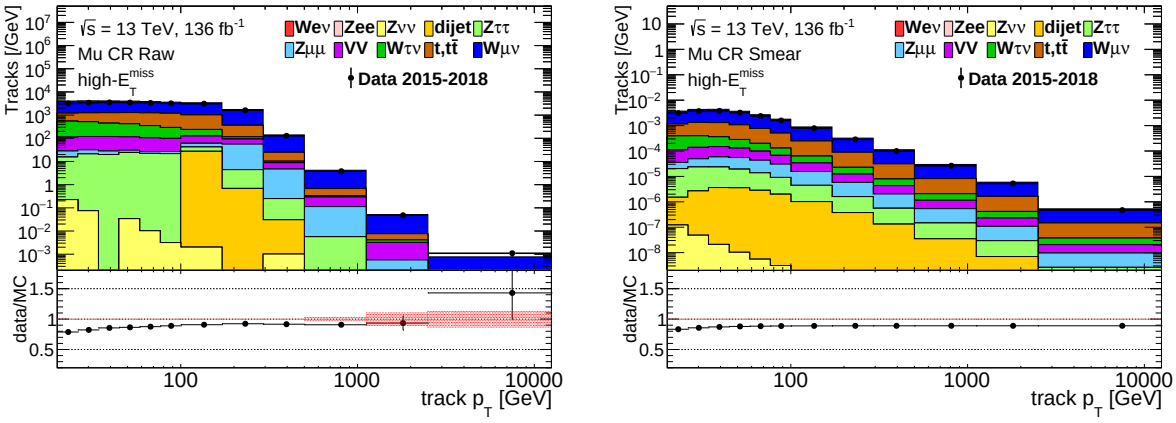

(a) $N^{\mathrm{CR}}_{\mu,\mathrm{signal}}$ (b) f^{μ}_{SR} after smearing

Figure 63: The p_{T} spectrum in the Mu-CR and the muon p_{T} template for the EWK channel.

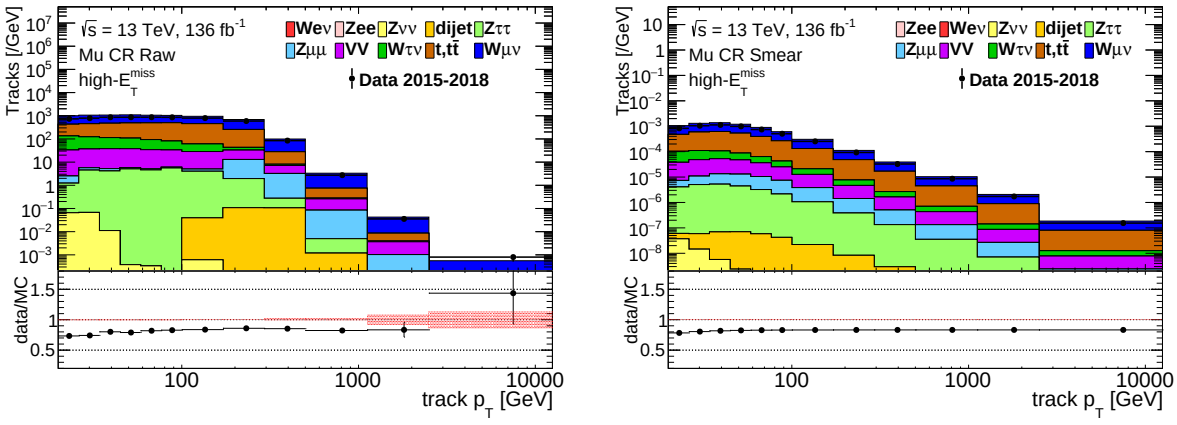

(a) $N^{\mathrm{CR}}_{\mu,\mathrm{signal}}$ (b) f^{μ}_{SR} after smearing

Figure 64: The p_{T} spectrum in the Mu-CR and the muon p_{T} template for the strong channel.

— The track corresponding to the electron satisfies the same track selection requirements as in the signal region except for a track p_{T} threshold of 10 GeV instead of 20 GeV, and neither requiring $N_{\mathrm{SCT}} = 0$, the highest p_{T} nor $\Delta R(\mathrm{electron}) > 0.4$.

- Measurements of $\mathrm{TF}^{e}_{\mathrm{pixel-only}}$ and $\mathrm{TF}^{e}_{\mathrm{calo-veto}}$

The transfer factor $\mathrm{TF}^{e}_{\mathrm{pixel-only}}$ is the factor that ID track of electron is identified as a disappearing track. The transfer factor $\mathrm{TF}^{e}_{\mathrm{calo-veto}}$ is the factor that the electron is isolated from calorimeter clusters. Transfer factors are measured by using $Z \to ee$ events with the tag and probe method same as the muon. To enhance $Z \to ee$ events, the electron triggers, no identified muons, at least one tag electron, at least one probe electron, and $|m_{\mathrm{tag,probe}} - m_Z| < 10$ GeV are required. The definitions of tag electron and probe electron are described as follows.

Definition of tag electrons :

- Reconstructed electrons matched to the electron trigger objects.
- Satisfying signal electron criteria.
- $p_{\mathrm{T}} > 30$ GeV.

Definition of probe electrons for $\mathrm{TF}^{e}_{\mathrm{pixel-only}}$ measurement :

- Calorimeter cluster with associated track within $\Delta R < 0.2$.
- Calorimeter cluster $p_{\mathrm{T}} > 10$ GeV.

- Calorimeter cluster $|\eta| < 2.5$.
- Associated track which satisfies same track criteria as in the Ele-CR except for $p_{\mathrm{T}} > 10$ GeV.

Definition of probe electrons for $\mathrm{TF}^{e}_{\mathrm{calo-veto}}$ measurement :

- ID track satisfies same track criteria as in the Ele-CR (see end of Section 6.4.2) except for $p_{\mathrm{T}} > 10$ GeV and additional requirement for $N_{\mathrm{SCT}} > 5$.

Then the transfer factors $\mathrm{TF}^{e}_{\mathrm{pixel-only}}$ and $\mathrm{TF}^{e}_{\mathrm{calo-veto}}$ are obtained by

$$\mathrm{TF}^{e}_{\mathrm{pixel-only}}(p_{\mathrm{T}}, \eta) = N_{\mathrm{pixel-only}}(p_{\mathrm{T}}, \eta)/N_{\mathrm{electron}}(p_{\mathrm{T}}, \eta), \quad (24)$$

$$\mathrm{TF}^{e}_{\mathrm{calo-veto}}(p_{\mathrm{T}}, \eta) = N_{E_{\mathrm{T}}^{\mathrm{clus20}}<5\mathrm{GeV}}(p_{\mathrm{T}}, \eta)/N_{E_{\mathrm{T}}^{\mathrm{clus20}}>5\mathrm{GeV}}(p_{\mathrm{T}}, \eta), \quad (25)$$

where $N_{\mathrm{pixel-only}}$ is the number of probe electrons satisfying $N_{\mathrm{SCT}} = 0$, N_{electron} is the number of probe electrons identified as good electrons, $N_{E_{\mathrm{T}}^{\mathrm{clus20}}}$ is the number of probe electrons satisfying the requirement for $E_{\mathrm{T}}^{\mathrm{clus20}}$ which is the sum of cluster energies within $\Delta R < 0.2$.

In order to subtract contributions from fake tracks, SS events are subtracted from OS events using the sign of the tag electron and the probe track. Figs. 66 and 67 show reconstructed dielectron mass distributions for the $\mathrm{TF}^{e}_{\mathrm{pixel-only}}$ and $\mathrm{TF}^{e}_{\mathrm{calo-veto}}$ measurement respectively. Only events satisfying $|m_{\mathrm{tag,probe}} - m_Z| < 10$ GeV are used for the calculation of the transfer factors. Figure 68 shows the transfer factor $\mathrm{TF}^{e}_{\mathrm{pixel-only}}$ for electron backgrounds. Figure 69 shows the transfer factor $\mathrm{TF}^{e}_{\mathrm{calo-veto}}$ for electron backgrounds. The statistic uncertainty for TF is evaluated by comparing PDF by using nominal TF values and 1σ shifted TF values. It is taken as an uncertainty for the normalization of electron background.

- Correction factor for $\mathrm{TF}_{\mathrm{calo-veto}}$

The $\mathrm{TF}_{\mathrm{calo-veto}}$ is measured in data by using $Z \to ee$ events from standard tracks. Responses to calorimeter are different for electrons and hadrons, and also for standard tracks and pixel-tracks. So correction factors are calculated by using single particle MC. Figure 70 shows calorimeter veto efficiency as a function of truth p_{T} for both electron and pion, and also for both standard tracks and pixel-tracks. Correction factors should be a function of standard track p_{T} because these are applied to standard tracks. To convert from a function of truth p_{T} to a function of standard track p_{T}, truth p_{T} distribution for each standard track p_{T} is obtained. Figure 71 shows the truth p_{T} distribution for standard tracks in 20.0 GeV $< p_{\mathrm{T}} <$ 23.9 GeV. Then correction factors are calculated for each standard track p_{T} bin by using information of Figure 70 and Figure 71. Specifically, the ratio of (electron pixel-track)/(electron

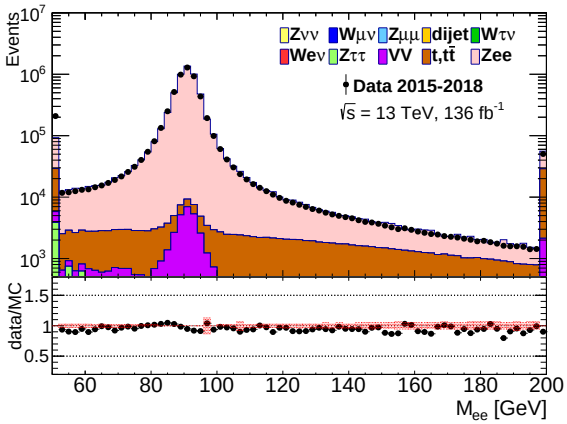

(a) Good electron category (OS)

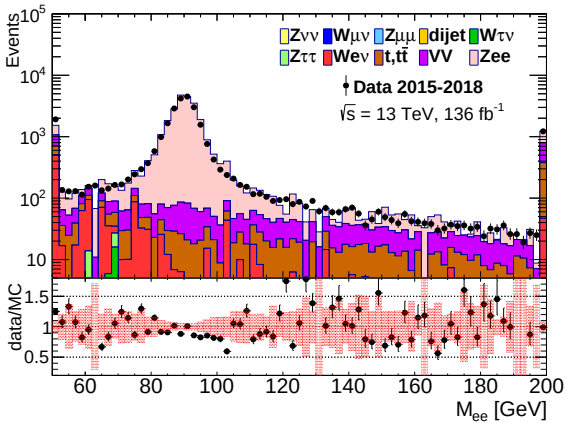

(b) Good electron category (SS)

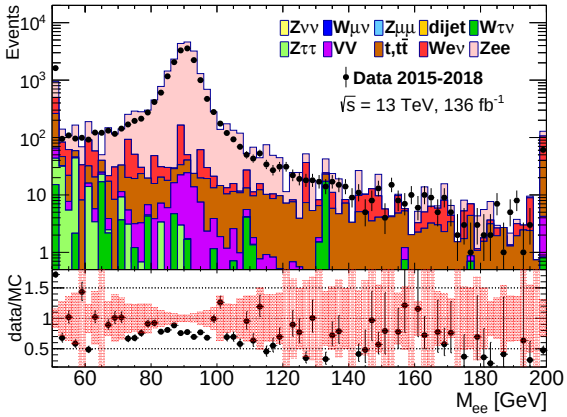

(c) Pixel-only track category (OS)

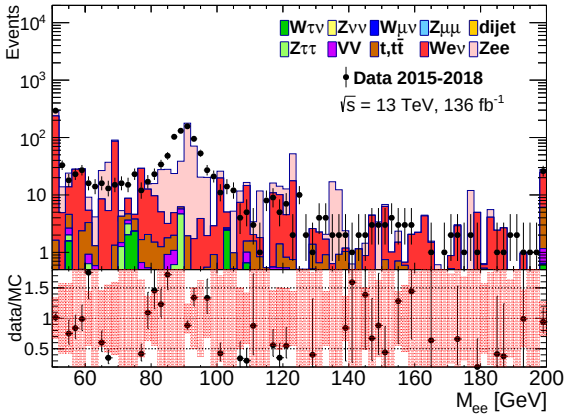

(d) Pixel-only track category (SS)

Figure 66: Reconstructed dielectron mass distribution for $\mathrm{TF}^{e}_{\mathrm{pixel-only}}$ measurement

std. track) in calo-veto efficiency is calculated for electron background and (hadron pixel-track)/(electron std. track) for hadron background. Figure 72 shows the correction factor as a function of standard track p_{T}. Nearly zero events are left after applying $\mathrm{TF}_{\mathrm{calo-veto}}$ in high-p_{T} region, so impact of correction factors in high-p_{T} region is negligible.

- Electron p_{T} template

Finally, the electron p_{T} template can be obtained by applying $\mathrm{TF}^{e}_{\mathrm{pixel-only}}$, $\mathrm{TF}^{e}_{\mathrm{calo-veto}}$, and smearing function to the events in the Ele-CR. Figure 73 and Figure 74 show $N^{\mathrm{CR}}_{e,\mathrm{signal}}$ and f^{e}_{SR} in the EWK and the strong channels, respectively.

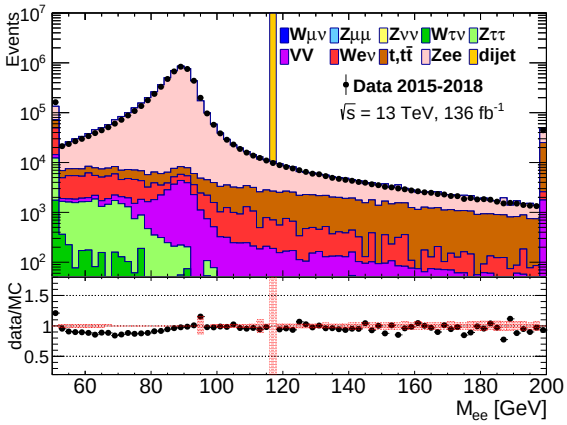

(a) Non isolated E_T^{clus20} category (OS)

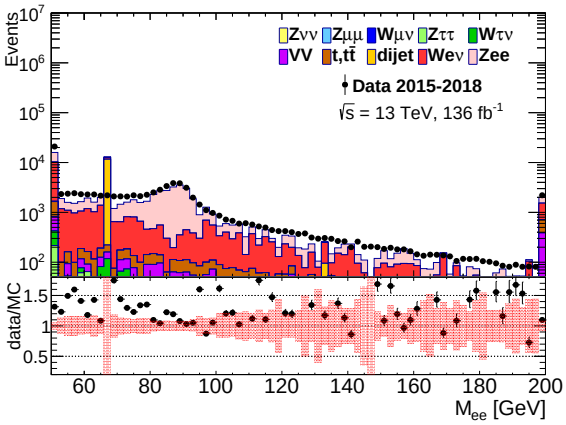

(b) Non isolated E_T^{clus20} category (SS)

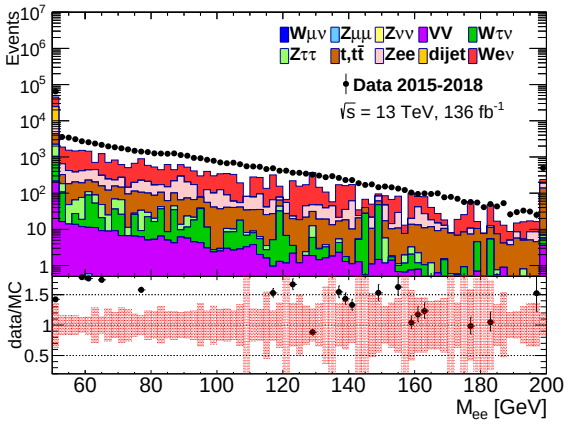

(c) Isolated E_T^{clus20} category (OS)

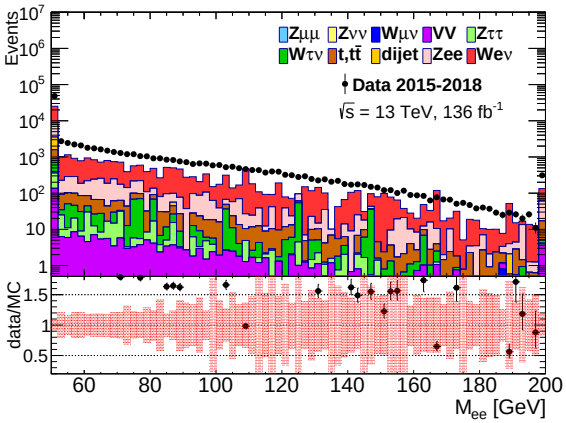

(d) Isolated E_T^{clus20} category (SS)

Figure 67: Reconstructed dielectron mass distribution for $TF^{e}_{calo-veto}$ measurement.

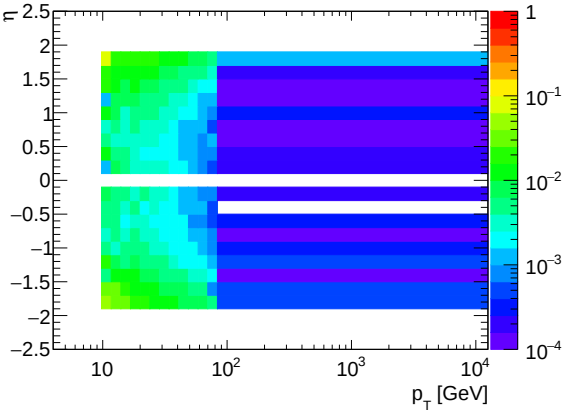

(a) Mean value

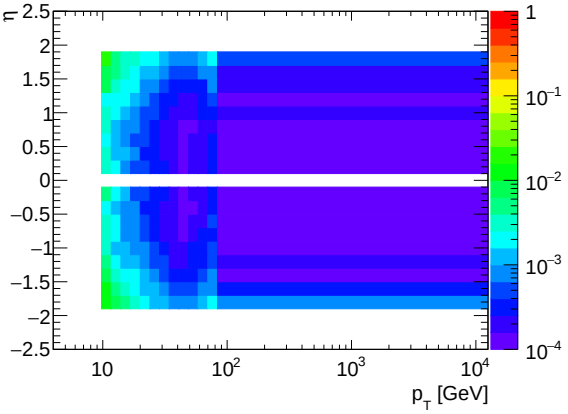

(b) Errors

Figure 68: Transfer factor $TF^{e}_{pixel-only}$ for electron backgrounds

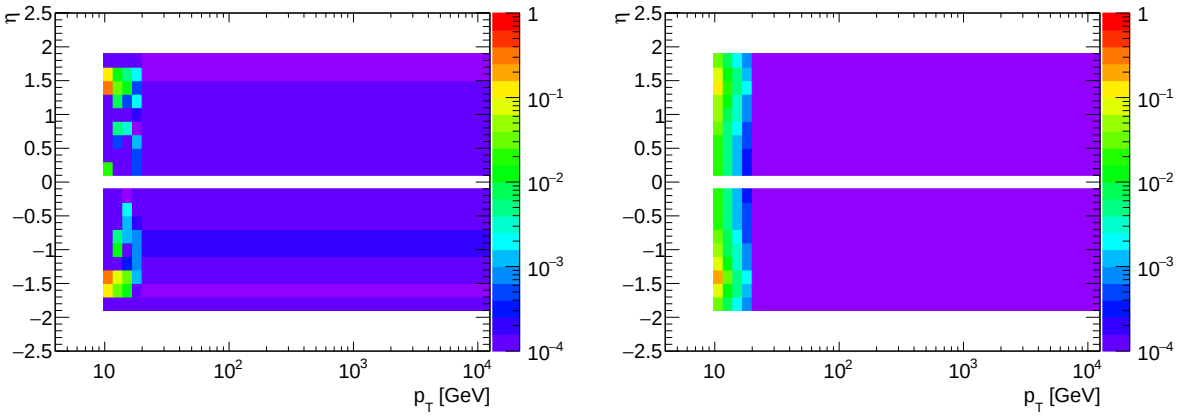

(a) Mean value

(b) Statistical error

Figure 69: Transfer factor $TF^{e}_{\text{calo}-\text{veto}}$ for electron backgrounds

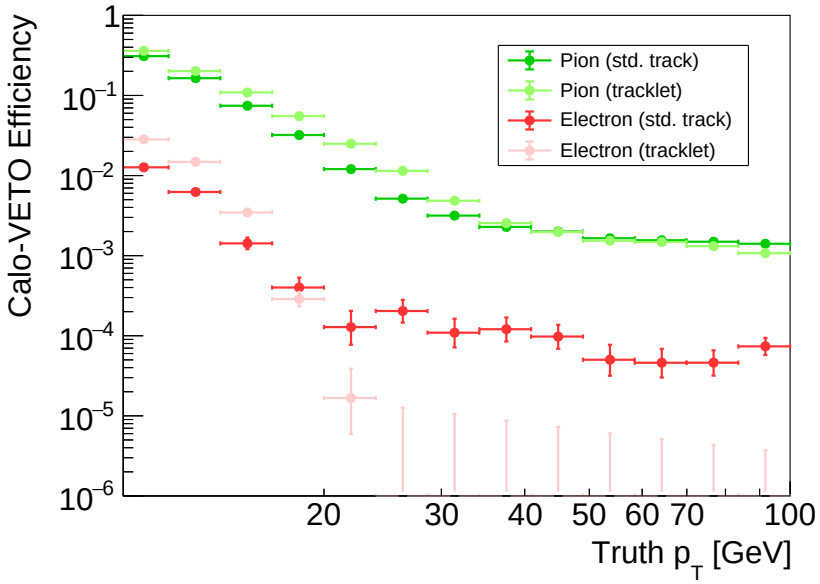

Figure 70: Calorimeter veto efficiency for electron and pion

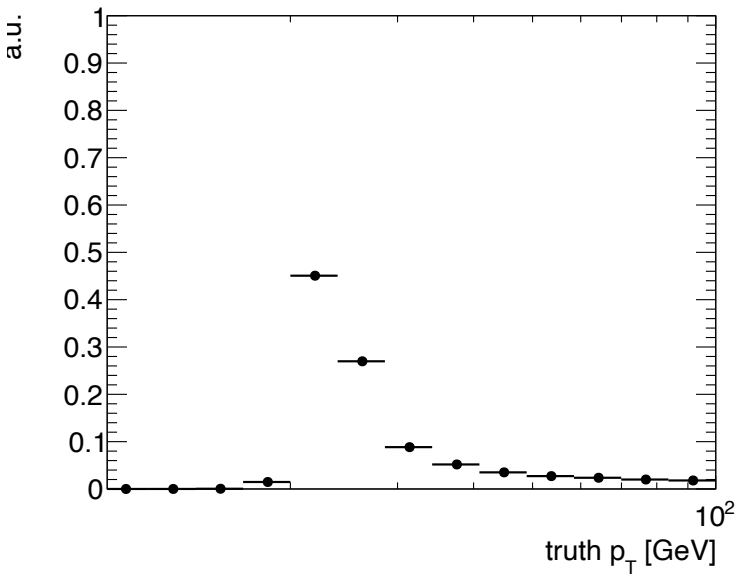

Figure 71: Truth p_T distribution for standard tracks (20.0GeV $< p_T <$ 23.9GeV)

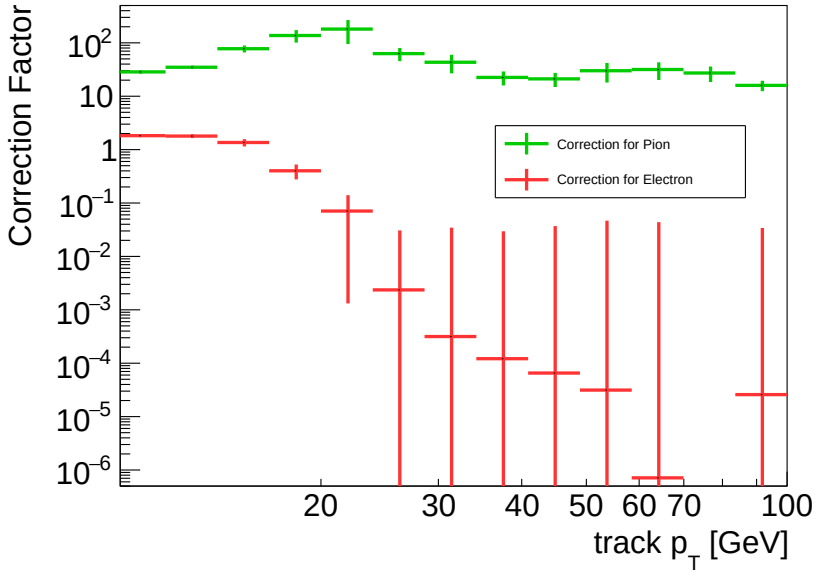

Figure 72: Correction factors for $TF_{calo-veto}$

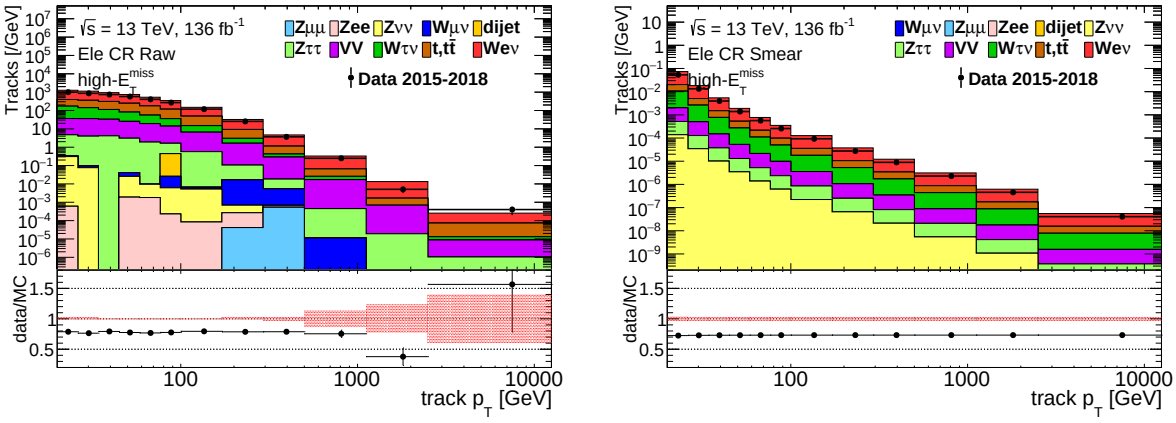

(a) $N^{\mathrm{CR}}_{e,\mathrm{signal}}$ (b) f^{e}_{SR} after smearing

Figure 73: The p_{T} spectrum in the Ele-CR and the electron p_{T} template for the EWK channel.

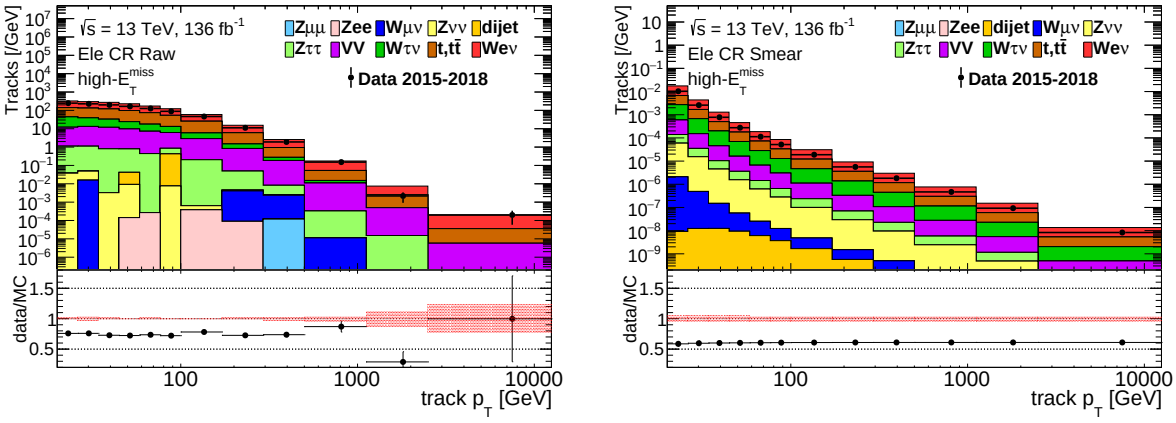

(a) $N^{\mathrm{CR}}_{e,\mathrm{signal}}$ (b) f^{e}_{SR} after smearing

Figure 74: The p_{T} spectrum in the Ele-CR and the electron p_{T} template for the strong channel.

6.4.3 Hadronic Background

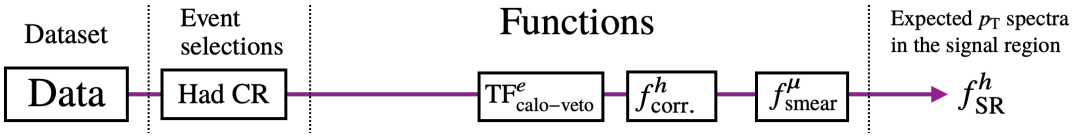

Figure 75: Overview for hadron background estimation.

Hadrons can be also classified as disappearing tracks mainly due to scattering in the detector materials. It is known that the bias to the shape in the p_T spectrum from hadron scattering is small and the p_T-spectrum of interacting hadron tracks is the same as that of non-interacting hadron tracks, so the p_T shape is estimated from non-interacting hadron tracks. The basic strategy to obtain the p_T template is the same as that for the lepton background.

- Definition of the Had-CR

The Had-CR is defined by the following requirements:

- The same kinematic selection requirements as for the signal region
- The leading track is required to have $N_{TRT} \geq 15$ and $N_{SCT} \geq 6$ for ensuring that charged particles penetrate the TRT detector without interactions.
- The associated calorimeter activities are required to the track with $E_T^{cone20} > 3$ GeV and $\sum_{\Delta R<0.4} E_T^{clus}/p_T^{track} > 0.5$, where E_T^{cone20} is the transverse calorimeter energy deposited in a cone of $\Delta R < 0.2$ around the track excluding E_T of its representing calorimeter cluster, and $\sum_{\Delta R<0.4} E_T^{clus}$ is the sum of cluster energies in a cone of $\Delta R < 0.4$ around the track, respectively.

- Transfer factor and correction factor

As already described in Section 6.4.2, the $TF_{calo-veto}$ is different between long tracks and pixel-tracks, and also between hadron and electron. Hence correction factors for hadron in Figure 72 are applied. Since the normalization of hadron background is a free parameter in the final fit, only the shape of the p_T spectrum is important. The impact of correction factors is negligible because its shape is almost flat compared to the track p_T spectrum itself.

- Hadron p_{T} template

Finally, the hadron-p_{T} template is obtained by smearing f_{SR}^{had}. Figures 76 and 77 show $N_{\mathrm{had}}^{\mathrm{CR}}$ and f_{SR}^{had} for the EWK channel and the strong channels, respectively.

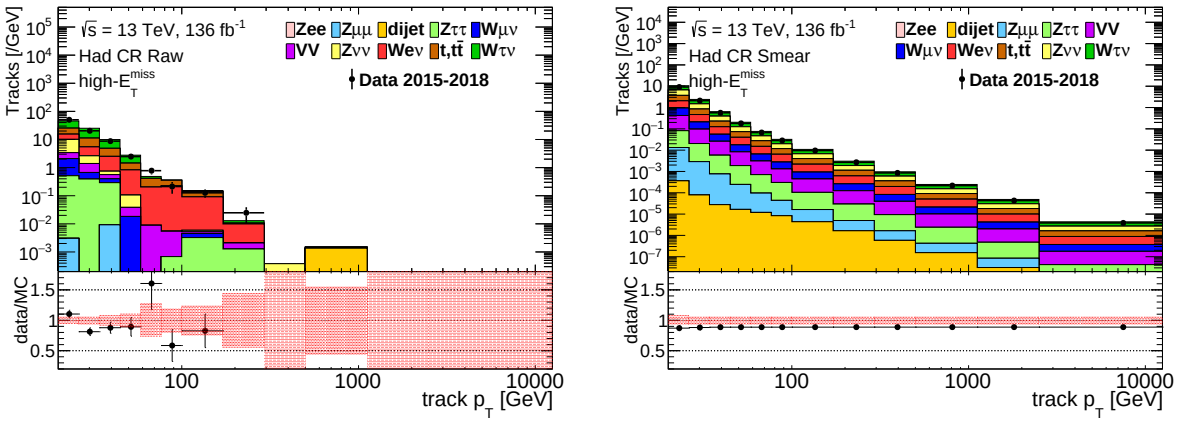

(a) $N_{\mathrm{had}}^{\mathrm{CR}}$ (b) f_{SR}^{had} after smearing

Figure 76: The p_{T} spectrum in the Had-CR and the hadron p_{T} template for the EWK channel.

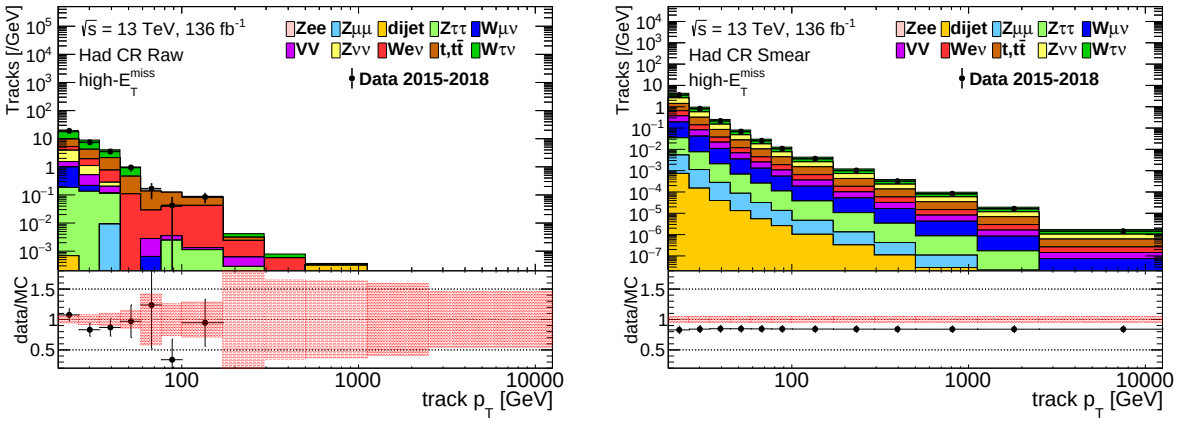

(a) $N_{\mathrm{had}}^{\mathrm{CR}}$ (b) f_{SR}^{had} after smearing

Figure 77: The p_{T} spectrum in the Had-CR and the hadron p_{T} template for the strong channel.

6.4.4 Fake Background

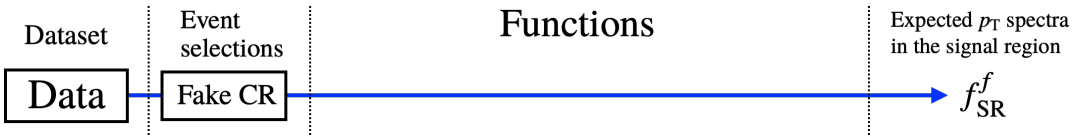

Figure 78: Overview for fake background estimation.

Fake tracks are most likely caused by a wrong combination of space points (wrong seed) or a wrong extension of pixel-seeded tracks (wrong extension). Using pixel-tracks helps to increase the acceptance of the decaying chargino tracks at small radii, but also leads to a non-negligible contribution of fake tracks in the signal search sample. The fake tracks could have anomalously high values of p_T and could mimic signal tracks, therefore, the understanding of their properties and a fair estimation of their contribution based on data are of particular importance. Fake tracks are most likely originating from a wrong combination of space-points hence their d_0 is broadly distributed, whereas the high-p_T chargino tracks have a good pointing resolution and the d_0 distribution clusters around zero. By applying a tight requirement on the impact parameter for the candidate tracks as described in Section 4.2, the contribution of fake tracks can be significantly suppressed. Furthermore, p_T and d_0 of fake tracks are (most likely) randomly distributed since they arise from randomly combined space-points. This feature is useful to define pure fake tracks control region (Fake-CR).

- Definition of the Fake-CR

The Fake-CR is defined by the exclusive requirement on the impact parameters as follows:

- Apply almost the same kinematic selection requirements as in the signal region, but without a E_T^{miss} selection applied, to increase statistics.
- Apply an exclusive cut on the impact parameter: $|d_0/\mathrm{err}(d_0)| < 1.5 \rightarrow |d_0/\mathrm{err}(d_0)| > 10$. Also apply the same disappearing track selection criteria except for this one.

- Fake p_T template

Figure 79 shows the p_T distribution of fake tracks with standard model BG MC samples. The fake background is strongly affected by detector condition, so it is hard to reproduce the p_T spectrum by MC. As shown in the figure, the SM background MC samples hardly reproduce the normalization of data. That is why data-driven background estimation is important, especially for the Fake background.

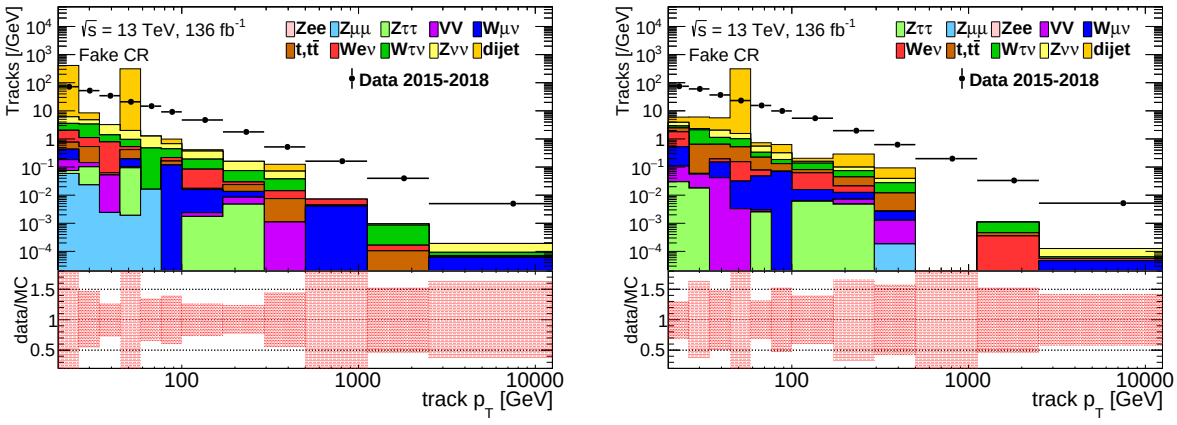

(a) EWK channel

(b) Strong channel

Figure 79: The p_{T} spectrum of fake background.

The p_{T} spectrum of fake tracks is modelled with the following functional form:

$$f\left(p_{\mathrm{T}}\right) = \exp\left(-p_0 \cdot \log(p_{\mathrm{T}}) - p_1 \cdot (\log(p_{\mathrm{T}}))^2\right), \tag{26}$$

where p_0 is fitting parameter, and p_1 almost satisfies following empirical relation $p_1 = 0.18 - 0.11 * p_0$.

The p_{T} shape fitting will be performed as described in Sec. 6.5. For the fake background, the value of (high-$E_{\mathrm{T}}^{\mathrm{miss}}$)/(low-$E_{\mathrm{T}}^{\mathrm{miss}}$) ratio is constrained by the value in Fake-CR. To consider $|d_0/\mathrm{err}(d_0)|$ dependence, the $|d_0/\mathrm{err}(d_0)|$ side-band region is also used. Figure 80 shows the definition of the $|d_0/\mathrm{err}(d_0)|$ side-band region. The number of fake events in (F/E)/(D/C) is used to constrain (B/A)/(D/C) during the fitting. Measured values are in below :

- EWK : 0.96 ± 0.20 (stat.)
- Strong : 1.14 ± 0.42 (stat.)

These values should be 1.0 if there is no dependence in $|d_0/\mathrm{err}(d_0)|$. So measured values indicate there is no d_0 dependence on the (high-$E_{\mathrm{T}}^{\mathrm{miss}}$)/(low-$E_{\mathrm{T}}^{\mathrm{miss}}$) ratio. Further detailed studies are performed for the fake background and summarized in Appendix D.

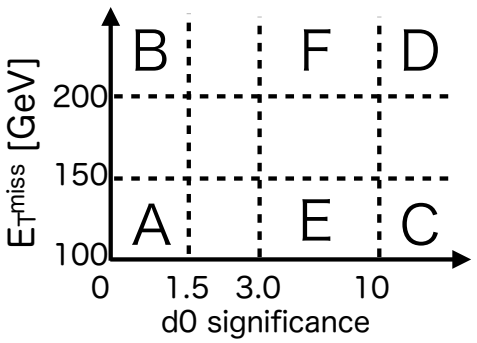

Figure 80: The definition of the $|d_0/\mathrm{err}(d_0)|$ side-band region for fake background

6.5 Fitting Method

To estimate the backgrounds in the SR, the pixel track p_{T} templates of the background events are fitted to the observed data in the high-$E_{\mathrm{T}}^{\mathrm{miss}}$ SR with simultaneously applying the low-$E_{\mathrm{T}}^{\mathrm{miss}}$ and the Fake-CR.

The middle-$E_{\mathrm{T}}^{\mathrm{miss}}$ region is also fitted instead of the high-$E_{\mathrm{T}}^{\mathrm{miss}}$ SR to validate the fitting procedure as well as the background estimation method. The p_{T} shape fitting is performed using the likelihood function for the high-$E_{\mathrm{T}}^{\mathrm{miss}}$ SR setup described in the following. For the VR fits, the high-$E_{\mathrm{T}}^{\mathrm{miss}}$ SR is replaced with the corresponding VR.

The likelihood function $\mathcal{L}$ for the pixel track p_{T} in a sample of observed events (N_{obs}) is defined as

$$\mathcal{L} = \mathcal{L}_{\mathrm{shape}} \times \mathcal{L}_{\mathrm{shape}}^{\text{Fake-CR}} \times \mathcal{L}_{\mathrm{syst}}. \tag{27}$$

The shape factors represent the probability to observe N_{obs} events in the low-$E_{\mathrm{T}}^{\mathrm{miss}}$ and high-$E_{\mathrm{T}}^{\mathrm{miss}}$ regions. The $\mathcal{L}_{\mathrm{shape}}$ term is defined as:

$$\mathcal{L}_{\mathrm{shape}} = \prod_{R}^{\text{low-/high-}E_{\mathrm{T}}^{\mathrm{miss}}} \mathcal{L}_{\mathrm{shape}}^{R},$$

with

$$\mathcal{L}_{\mathrm{shape}}^{R} = \frac{\exp\left(-\sum_{i}^{s,e,\mu,h,f} n_i^R\right)}{N_{\mathrm{obs}}^R\,!} \times \prod_{N_{\mathrm{obs}}^R} \left(\sum_{i'}^{s,e,\mu,h} \left(n_{i'}^R \cdot f_{i'}^R(p_{\mathrm{T}}; \sigma_{i'}, \alpha_{i'}) \right) + n_f^R \cdot f_f(p_{\mathrm{T}}; p_0, p_1) \right).$$

The $\mathcal{L}_{\mathrm{shape}}^{\text{Fake-CR}}$ term is defined as:

$$\mathcal{L}_{\mathrm{shape}}^{\text{Fake-CR}} = \frac{\exp\left(-n_f^{\text{Fake-CR}}\right)}{N_{\mathrm{obs}}^{\text{Fake-CR}}\,!} \times \prod_{N_{\mathrm{obs}}^{\text{Fake-CR}}} \left(n_f^{\text{Fake-CR}} \cdot f_f(p_{\mathrm{T}}; p_0, p_1) \right).$$

Here s, e, μ, h and f are subscripts of the signal process and the electron, muon, hadron and fake backgrounds respectively; N_{obs}^R is the number of observed events in each of the fitted regions, R = high-$E_{\mathrm{T}}^{\mathrm{miss}}$ or low-$E_{\mathrm{T}}^{\mathrm{miss}}$ region; n_i^R is the estimated number of events of process i in region R; $\sigma_{i'}$ and $\alpha_{i'}$ are the smearing parameters of process i'; p_0 and p_1 are the parameters for the fake background fit described in Section 6.4.4; f_i is the charged-particle scattering background-shape template for process

i; n_f^R is the estimated number of the fake events in region R and $n_f^{\text{low-}E_{\text{T}}^{\text{miss}}}$ is a free parameter in the likelihood fit. The parameter $n_f^{\text{high-}E_{\text{T}}^{\text{miss}}}$ is calculated from:

$$n_f^{\text{high-}E_{\text{T}}^{\text{miss}}} = r_{\text{CD}} \cdot \exp(r_{\text{ABCD}}) \cdot n_f^{\text{low-}E_{\text{T}}^{\text{miss}}},$$

with r_{CD} defined as:

$$r_{\text{CD}} = \frac{n_f^{\text{Fake-CR(high-}E_{\text{T}}^{\text{miss}})}}{n_f^{\text{Fake-CR(low-}E_{\text{T}}^{\text{miss}})}},$$

and r_{ABCD} defined as:

$$r_{\text{ABCD}} = \ln \frac{n_f^{\text{high-}E_{\text{T}}^{\text{miss}}} / n_f^{\text{Fake-CR(high-}E_{\text{T}}^{\text{miss}})}}{n_f^{\text{low-}E_{\text{T}}^{\text{miss}}} / n_f^{\text{Fake-CR(low-}E_{\text{T}}^{\text{miss}})}}. \tag{28}$$

Here r_{CD} and r_{ABCD} are terms to constrain the combinatorial fake-track background in the high-$E_{\text{T}}^{\text{miss}}$ SR relative to that in the low-$E_{\text{T}}^{\text{miss}}$ CR, and $n_f^{\text{Fake-CR}}$ is a free parameter estimating the number of events in the fake pixel-track control region. The r_{CD} is the ratio (high-$E_{\text{T}}^{\text{miss}}$/low-$E_{\text{T}}^{\text{miss}}$) for the fake background. The nominal value and uncertainty are estimated from the Fake-CR. While the r_{ABCD} is a d_0 dependence term of the ratio (high-$E_{\text{T}}^{\text{miss}}$/low-$E_{\text{T}}^{\text{miss}}$). As described in the previous section, no d_0 dependence has been observed between the Fake-CR and the $|d_0/\text{err}(d_0)|$ side-band region within statistical errors. So the nominal value is set to 0 and the statistical errors are assigned as an uncertainty.

The likelihood $\mathcal{L}_{\text{syst}}$ consists of a product of terms related to the systematic uncertainties in each background process and the signal process, $\mathcal{L}_{\text{syst}} = \mathcal{L}_{\text{syst}}^{s} \times \mathcal{L}_{\text{syst}}^{e} \times \mathcal{L}_{\text{syst}}^{\mu} \times \mathcal{L}_{\text{syst}}^{h} \times \mathcal{L}_{\text{syst}}^{f}$. Each likelihood component is defined as below:

$$
\begin{aligned}
\mathcal{L}^{s}_{\text{syst}} &= G\left(\sigma_s; \overline{\sigma_s}, \Delta\sigma_s\right) \times G\left(\alpha_s; \overline{\alpha_s}, \Delta\alpha_s\right) \times \prod_R G\left(n_s^R; \overline{n_s^R}, \Delta n_s^R\right), \\
\mathcal{L}^{\mu}_{\text{syst}} &= G\left(\sigma_\mu; \overline{\sigma_\mu}, \Delta\sigma_\mu\right) \times G\left(\alpha_\mu; \overline{\alpha_\mu}, \Delta\alpha_\mu\right) \times \prod_R G\left(n_\mu^R; \overline{n_\mu^R}, \Delta n_\mu^R\right), \\
\mathcal{L}^{e}_{\text{syst}} &= G\left(\sigma_e; \overline{\sigma_e}, \Delta\sigma_e\right) \times G\left(\alpha_e; \overline{\alpha_e}, \Delta\alpha_e\right) \times \prod_R G\left(n_e^R; \overline{n_e^R}, \Delta n_e^R\right), \\
\mathcal{L}^{h}_{\text{syst}} &= G\left(\sigma_h; \overline{\sigma_h}, \Delta\sigma_h\right) \times G\left(\alpha_h; \overline{\alpha_h}, \Delta\alpha_h\right), \\
\mathcal{L}^{f}_{\text{syst}} &= G\left(r_{\text{ABCD}}; 0, \Delta r_{\text{ABCD}}\right),
\end{aligned}
$$

where $G(a; b, f)$ represents a unit Gaussian function of a with a mean of b and a standard deviation f. The expected value and the uncertainty of a variable x are represented by $\overline{x}$ and Δx respectively.

The likelihood is maximised by minimising the negative log-likelihood function with the MINUIT [42] package in the RooFit framework [43]. The fit parameters are the normalisations of the hadron and the fake backgrounds (n_h^R and n_f^R), the p_0 and p_1 parameters of the function modelling the fake pixel-track p_{T} distribution described in Section 6.4.4, and nuisance parameters. Each nuisance parameter represents a source of systematic uncertainty and is allowed to float in the fit with a Gaussian constraint. The statistical uncertainty of the transfer factors for electrons and muons is propagated into the final template. The list of floating and constrained nuisance parameters is summarized in Table 14.

Nuisance parameter	Configuration
r_{CD}	free-floating
r_{ABCD}	allowed to vary within uncertainty
$n_f^{\text{Fake-CR}}$	free-floating
$n_f^{\text{low-}E_{\mathrm{T}}^{\mathrm{miss}}}$	free-floating
p_0	free-floating
p_1	free-floating
$n_h^{\text{low-}E_{\mathrm{T}}^{\mathrm{miss}}}$	free-floating
$n_h^{\text{high-}E_{\mathrm{T}}^{\mathrm{miss}}}$	free-floating
$n_e^{\text{low-}E_{\mathrm{T}}^{\mathrm{miss}}}$	allowed to vary within uncertainty
$n_e^{\text{high-}E_{\mathrm{T}}^{\mathrm{miss}}}$	allowed to vary within uncertainty
$n_\mu^{\text{low-}E_{\mathrm{T}}^{\mathrm{miss}}}$	allowed to vary within uncertainty
$n_\mu^{\text{high-}E_{\mathrm{T}}^{\mathrm{miss}}}$	allowed to vary within uncertainty
$\alpha_{\mathrm{h}}^{\text{smearing}}$	allowed to vary within uncertainty
$\sigma_{\mathrm{h}}^{\text{smearing}}$	allowed to vary within uncertainty
$\alpha_{\mathrm{e}}^{\text{smearing}}$	allowed to vary within uncertainty
$\sigma_{\mathrm{e}}^{\text{smearing}}$	allowed to vary within uncertainty
$\alpha_\mu^{\text{smearing}}$	allowed to vary within uncertainty
$\sigma_\mu^{\text{smearing}}$	allowed to vary within uncertainty
μ_{s}	free-floating
$n_s^{\text{low-}E_{\mathrm{T}}^{\mathrm{miss}}}$	allowed to vary within uncertainty
$n_s^{\text{high-}E_{\mathrm{T}}^{\mathrm{miss}}}$	allowed to vary within uncertainty
$\alpha_{\mathrm{s}}^{\text{smearing}}$	allowed to vary within uncertainty
$\sigma_{\mathrm{s}}^{\text{smearing}}$	allowed to vary within uncertainty

Table 14: List of fitting parameters

6.6 Systematic Uncertainties

6.6.1 Systematic Uncertainties in Backgrounds

The uncertainties in the normalization of electron and muon background are dominated by the uncertainties of the TFs, while the shape uncertainties for hadron, electron, and muon background are dominated by the uncertainties in the smearing parameters. The TF uncertainties are estimated by statistical uncertainty of the denominator and numerator of the TF itself. The uncertainties in the smearing function consist of its uncertainties of parameters σ and α for the muon, electron, and hadron background. The pile-up condition is the largest source of the uncertainty in the smearing parameters, especially for low-p_{T} pixel-track. The pile-up uncertainty is evaluated by taking the difference between the nominal values of the smearing parameters and the values obtained from events with different pile-up conditions. This is done by splitting the dataset into data taken in low ($\mu < 40$) and high ($\mu > 40$) pile-up conditions, and the full parameter-value differences between the datasets with low- and high- pile-up are assigned as the systematic uncertainties of the p_{T} dependent smearing parameters.

The uncertainties on r_{CD} and r_{ABCD} are assessed from statistical uncertainties in the control regions used to calculate these parameters. Since fake pixel-tracks are the dominant background in the signal regions, variations of these parameters are the leading source of uncertainty in both the EWK and the strong channels. Similarly, the p_0 and p_1 parameters are varied up and down by their statistical uncertainties obtained from the fit.

Table 15 shows an impact of each systematic uncertainties which are included in the fitting. The impacts are calculated by effects of the signal exclusion significant at $m_{\tilde{\chi}_1^\pm} = 600$ GeV for the EWK channel, and $m_{\tilde{g}} = 1400$ GeV and $m_{\tilde{\chi}_1^\pm} = 1100$ GeV for the strong channel.

6.6.2 Systematic Uncertainties in Signal

A breakdown of the systematic uncertainties in the expected number of signal events at the signal region is shown in Table 17 and 18 for the EWK and the strong signal respectively.

Theoretical uncertainties in the signal cross-section are estimated by computing the changes in the cross-section when the renormalization and factorization scales, the choice of PDFs, and the strong coupling constant, α_S, are varied independently. Renormalisation and factorization scales are varied by factors of 0.5 and 2 from their nominal value. The PDF uncertainty is estimated as the maximum of the uncertainty from the CTEQ6.6 [44] uncertainty band at 68% confidence level and the difference

	EWK channel [%]	Strong channel [%]
r_{ABCD}	5.2	0.9
r_{CD}	3.2	0.6
σ parameter in signal p_{T} smearing function	2.9	0.1
α parameter in signal p_{T} smearing function	1.7	0.2
p_0 parameter in the fake background p_{T} function	0.3	<0.1
p_1 parameter in the fake background p_{T} function	0.3	0.2
Normalisation of muon background	0.6	<0.1
Normalisation of electron background	<0.1	<0.1
α parameter in muon p_{T} smearing function	<0.1	<0.1
σ parameter in muon p_{T} smearing function	<0.1	<0.1
α parameter in electron p_{T} smearing function	<0.1	<0.1
σ parameter in electron p_{T} smearing function	<0.1	<0.1
α parameter in hadron p_{T} smearing function	0.5	0.2
σ parameter in hadron p_{T} smearing function	0.6	0.2

Table 15: Effects of systematic uncertainties on the signal exclusion significance for a representative signal point with $m_{\tilde{\chi}_1^\pm} = 600$ GeV for the EWK channel and $m_{\tilde{g}} = 1400$ GeV and $m_{\tilde{\chi}_1^\pm} = 1100$ GeV for the strong channel.

between the results for the CTEQ6.6 and MSTW2008 NLO PDF [45] sets. Each uncertainty is varied independently and their effects are added in quadrature.

Uncertainties in the modeling of ISR and final-state radiation (FSR) are estimated by varying the renormalization, factorization, and merging scales from 0.5 to 2 times their nominal values. Jet modeling uncertainties related to the jet energy scale (JES), jet energy resolution (JER), and jet vertex tagging (JVT) uncertainty are estimated by comparing simulated events and data as described in Ref. [46]. The pile-up modeling uncertainty is estimated by varying the number of collisions per bunch crossing in simulation by its uncertainty of 10% of the nominal value. The uncertainty in the $E_{\text{T}}^{\text{miss}}$ track soft-term (TST) modeling is considered by comparing data and simulated samples using $Z \to \mu\mu$ + jets events as described in Ref. [46]. Figure 81 and Figure 82 show relative variation for each parameters.

The estimation of the trigger efficiency function is described in section 6.3.1, where the efficiency is measured using $W \to \mu\nu$ data as a function of $E_{\text{T}}^{\text{miss}}$ subtracting the muon contribution and the leading jet p_{T}. The statistical uncertainty in the measurement is propagated to the uncertainty in the signal yield in the signal region. The signal yield after applying the kinematics selection is computed by applying two trigger-efficiency functions (nominal and shifted). The shifted trigger-efficiency function is obtained by shifting the efficiency of all ($E_{\text{T}}^{\text{miss}}$, leading-jet p_{T}) bins to the same direction (up or down) by 1 σ for a conservative estimation. The maximum difference from the nominal is used as a systematic uncertainty.

The uncertainty in the pixel-track selection efficiency is evaluated by comparing efficiencies for muons in the collision data and simulation. Events containing muons from Z boson decays are selected and muons are re-tracked using only pixel hits as described in Section 5.4. The breakdown of each pixel-

track selection efficiency is summarized in Table 16. The difference of the overall efficiency between data and MC, 5.9% is added as the uncertainty of selection efficiency.

The uncertainties in the integrated luminosity are ±2.1%, ±2.4%, and ±2.0% in 2015+2016, 2017, and 2018 respectively. The combined luminosity uncertainty is ±1.7%.

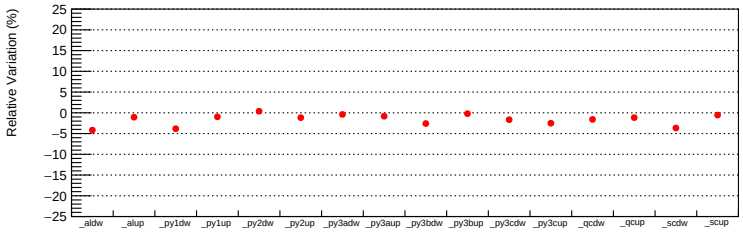

Figure 81: ISR/FSR systematics calculation at 700 GeV (EWK channel)

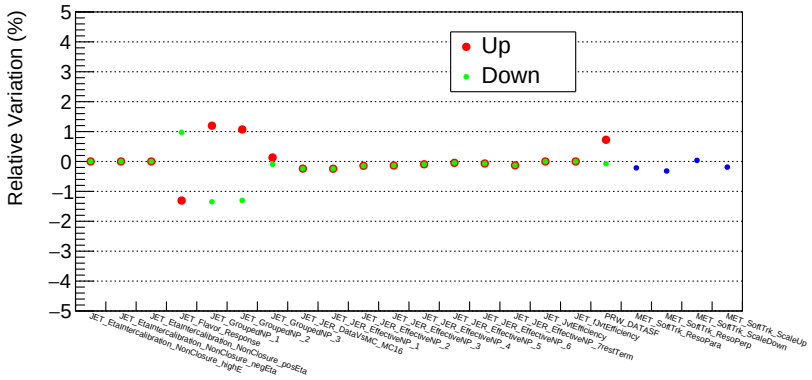

Figure 82: JES, JER, JVT, Pile-up and TST MET systematics calculation at 600 GeV (EWK channel)

Requirement	Data	Zmumu MC
4 pixel layers	98.58%	99.12%
nGangedFlaggedFake == 0	99.87%	99.91%
Pixel spoilt hits == 0	93.86%	95.34%
nPixel outliers == 0	99.68%	99.69%
Pixel dead module map	− − −	89.97%
$\lvert d_0\text{significance}\rvert < 1.5$	88.28%	91.12%
$\lvert z_0 \sin\theta\rvert < 0.5$ mm	99.92%	99.92%
$\Delta R(\text{jets}) > 0.4$	99.95%	99.96%
Quality > 0.1	95.22%	95.72%
$0.1 < \lvert\eta\rvert < 1.9$	90.64%	90.52%
$E_{\text{T}}^{\text{topoclus20}} < 5.0$ GeV	94.04%	93.02%
Total	67.47%	63.50%

Table 16: Track selection efficiency for data and MC

Source	Chargino mass (GeV) 91	200	300	400	500	600	700	800	900	1000
(**Theoretical uncertainty**)										
Cross-section ($\tilde{\chi}_1^+\tilde{\chi}_1^-$)	±2.6	±4.0	±4.9	±5.6	±6.3	±6.8	±7.3	±7.7	±8.6	±8.5
Cross-section ($\tilde{\chi}_1^\pm\tilde{\chi}_1^0$)	±4.1	±5.5	±6.3	±7.0	±7.6	±8.2	±8.9	±9.5	±8.5	±8.7
(**Uncertainties on the acceptance**)										
ISR/FSR	$^{+15.4}_{-5.4}$	$^{+3.5}_{-11.9}$	$^{+1.9}_{-11.1}$	$^{+0.2}_{-10.3}$	$^{+0.2}_{-9.4}$	$^{+0.2}_{-8.4}$	$^{+0.2}_{-7.4}$	$^{+2.6}_{-6.1}$	$^{+5.0}_{-4.8}$	$^{+7.5}_{-3.5}$
JES	$^{+3.6}_{-3.2}$	$^{+2.6}_{-2.2}$	$^{+2.4}_{-2.0}$	$^{+1.8}_{-2.1}$	$^{+2.3}_{-2.1}$	$^{+1.9}_{-2.3}$	$^{+2.1}_{-1.8}$	$^{+1.5}_{-2.0}$	$^{+1.8}_{-1.6}$	$^{+1.8}_{-1.7}$
JER	±2.1	±0.8	±1.3	±0.5	±0.7	±0.6	±0.4	±0.5	±0.9	±0.8
JVT	$^{+0.0}_{-0.0}$	$^{+0.0}_{-0.0}$	$^{+0.0}_{-0.0}$	$^{+0.0}_{-0.0}$	$^{+0.0}_{-0.0}$	$^{+0.0}_{-0.0}$	$^{+0.0}_{-0.0}$	$^{+0.0}_{-0.0}$	$^{+0.0}_{-0.0}$	$^{+0.0}_{-0.0}$
Pile-up reweighting	$^{+0.0}_{-0.9}$	$^{+0.0}_{-0.2}$	$^{+0.0}_{-0.6}$	$^{+0.0}_{-0.6}$	$^{+0.2}_{-0.1}$	$^{+0.7}_{-0.1}$	$^{+0.2}_{-0.7}$	$^{+0.1}_{-0.0}$	$^{+0.0}_{-0.1}$	$^{+0.3}_{-0.0}$
TST MET	$^{+0.9}_{-1.5}$	$^{+0.5}_{-0.6}$	$^{+0.3}_{-0.3}$	$^{+0.2}_{-0.4}$	$^{+0.3}_{-0.2}$	$^{+0.0}_{-0.4}$	$^{+0.2}_{-0.2}$	$^{+0.2}_{-0.3}$	$^{+0.2}_{-0.3}$	$^{+0.2}_{-0.3}$
Trigger efficiency					±0.3					
Signal selection efficiency					±5.9					
Luminosity					±1.7					
Sub-total	±17.2	±13.7	±13.0	±12.2	±11.5	±10.7	±9.9	±8.9	±8.2	±9.9

Table 17: Summary of systematic uncertainties [%] in the expectation of signal events.

Source	Signal point $m_{\tilde{g}}$ = 1400 GeV, $\tilde{\chi}_1^\pm$ = 1100 GeV
(**Theoretical uncertainty**)	
Cross-section	±14.4
(**Uncertainties on the acceptance**)	
ISR/FSR	$^{+3.2}_{-5.1}$
JES	$^{+1.4}_{-1.5}$
JER	±0.3
JVT	$^{+0.0}_{-0.0}$
Pile-up	$^{+0.0}_{-0.0}$
TST MET	$^{+0.0}_{-0.0}$
Trigger efficiency	±0.4
Signal selection efficiency	±5.9
Luminosity	±1.7
Sub-total	±8.1

Table 18: Summary of systematic uncertainties [%] in the expectation of signal events.

6.7 Results

6.7.1 Results in Validation Regions

First, the p_{T} shape fitting is performed in the middle-$E_{\mathrm{T}}^{\mathrm{miss}}$ validation regions (VRs) with the calo-veto requirement to validate the low-p_{T} region and with the calo-sideband requirement to validate the high-p_{T} region. Figure 83 and Figure 84 show the p_{T} spectra of the fitted pixel-tracks in the middle-$E_{\mathrm{T}}^{\mathrm{miss}}$ VRs for the EWK channel and the strong channel respectively. The numbers of expected and observed events in the VRs are summarized in Table 19. The calorimeter sideband region is for the validation of the fake background, and the low-p_{T} region is for the validation of the hadron background. The contamination of the signal events is negligible in these VRs. These are good agreements between the expected and the observed in all VRs, so the fitting method works fine.

	Electroweak channel		Strong channel	
	Calo. sideband $p_{\mathrm{T}} > 60$ GeV	Low p_{T} $p_{\mathrm{T}} < 60$ GeV	Calo. sideband $p_{\mathrm{T}} > 60$ GeV	Low p_{T} $p_{\mathrm{T}} < 60$ GeV
Fake	4.3 ± 2.2	5.5 ± 1.5	3.2 ± 1.5	3.5 ± 1.0
Hadron	1.0 ± 0.8	23 ± 6	0.36 ± 0.23	13 ± 4
Electron	0.8 ± 0.5	1.2 ± 1.3	0.29 ± 0.20	0.5 ± 0.5
Muon	0.023 ± 0.007	0.25 ± 0.06	0.012 ± 0.004	0.129 ± 0.032
Total Expected	6.1 ± 1.9	29 ± 5	3.8 ± 1.5	17 ± 4
Observed	5	30	3	18

Table 19: Expected and observed numbers of events and corresponding background predictions in the middle-$E_{\mathrm{T}}^{\mathrm{miss}}$ validation regions. The uncertainty in the total background prediction differs from the sum in quadrature of the individual components due to anti-correlation of fit parameters between the backgrounds.

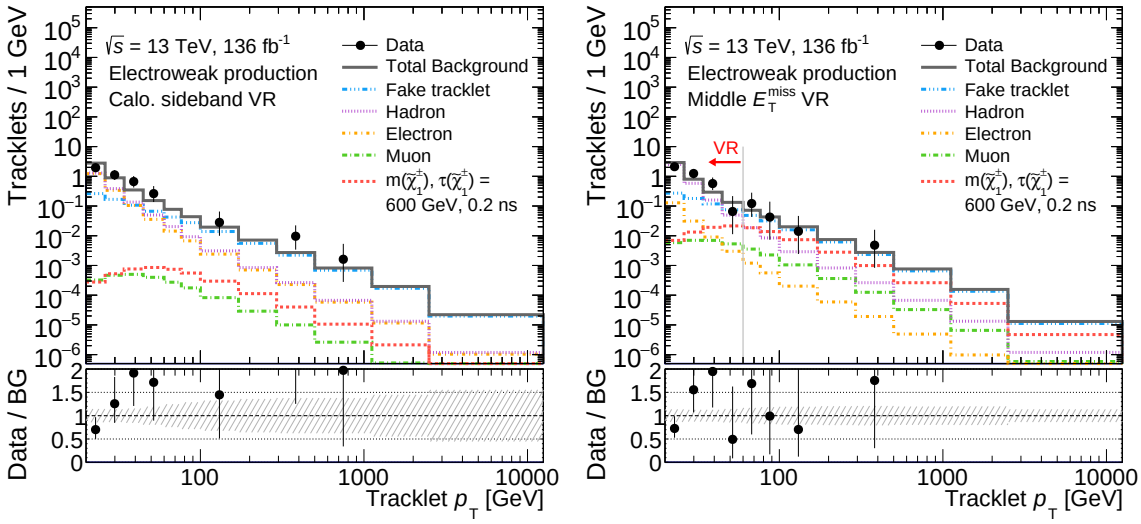

(a) Calo. sideband (b) Low p_T

Figure 83: Fitting results of pixel-track p_T spectrum in the middle-E_T^{miss} validation regions for the electroweak production channel. The fake, hadron, electron and muon templates are fitted to observed data events in a background-only fit. An example of the expected-signal prediction with $m_{\tilde{\chi}_1^\pm}$ = 600 GeV and $\tau_{\tilde{\chi}_1^\pm}$ = 0.2 ns is overlaid in red. The last bin includes overflow entries. The bottom panel shows the ratio of data to the background-only prediction.

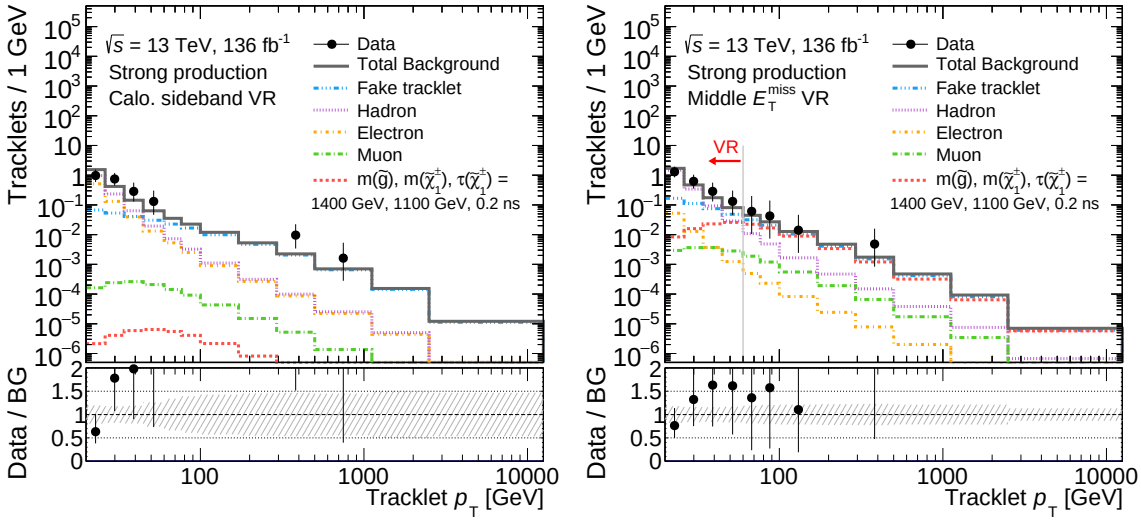

(a) Calo. sideband (b) Low p_T

Figure 84: Fitting results of pixel-track p_T spectrum in the middle-E_T^{miss} validation regions for the strong production channel. The fake, hadron, electron and muon templates are fitted to observed data events in a background-only fit. An example of the expected-signal prediction with $m_{\tilde{g}}$ = 1400 GeV, $m_{\tilde{\chi}_1^\pm}$ = 1100 GeV and $\tau_{\tilde{\chi}_1^\pm}$ = 0.2 ns is overlaid in red. The last bin includes overflow entries. The bottom panel shows the ratio of data to the background-only prediction.

6.7.2 Results in Signal Regions

Since the validation of the fitting method is done, the p_{T} shape fitting in the high-$E_{\mathrm{T}}^{\mathrm{miss}}$ SR is performed. Figure 85 and 86 show the p_{T} spectra of the fitted pixel-tracks in the low-$E_{\mathrm{T}}^{\mathrm{miss}}$ CR and the high-$E_{\mathrm{T}}^{\mathrm{miss}}$ SR for the EWK channel and the strong channel respectively. The numbers of expected and observed events in the SR are summarized in Table 20. Figure 87 and Figure 88 show the pull and the correlation matrix of fitting parameters in the EWK channel respectively. The best fit values of nuisance parameters are also summarized in Table 21. Unfortunately, there is no significant excess above the background predictions in both channels. Therefore, the probability of a background-only experiment being more signal-like than observed (p_0), its equivalent formulation in terms of the number of standard deviations (Z), and the upper limit on the model-independent visible cross-section at 95% confidence level (CL) using the CLs technique are calculated and also summarized in Table 20. For the evaluation of these model-independent quantities, the number of events in the high-p_{T} region is counted.

Model-dependent exclusion limits at 95% CL are calculated for the various signal models. Figure 89 shows the observed exclusion limit for the wino search in the EWK channel. The expected lower limit on the mass of a chargino with $\tau_{\tilde{\chi}_1^\pm}$ = 0.2 ns is improved from 450 GeV in the previous search to 680 GeV in this search, while a simple scaling from the integrated luminosity of 136 fb^{-1} gives an expected mass limit of 530 GeV. The observed limit excludes chargino masses up to 660 GeV on the theoretical pure-wino prediction line shown with the grey dashed line.

For the higgsino search in the EWK channel, the observed exclusion limit as a function of the chargino mass and the chargino lifetime is shown in Figure 90 (a), and as a function of the chargino mass and

	Electroweak channel	Strong channel
Fake	2.6 ± 0.8	0.77 ± 0.33
Hadron	0.26 ± 0.13	0.024 ± 0.031
Electron	0.021 ± 0.023	0.004 ± 0.004
Muon	0.17 ± 0.06	0.049 ± 0.018
Total Expected	3.0 ± 0.7	0.84 ± 0.33
Observed	3	1
p_0 (Z)	0.5 (0)	0.38 (0.30)
Observed $\sigma_{\mathrm{vis}}^{95\%}$ [fb]	0.037	0.028
Expected $\sigma_{\mathrm{vis}}^{95\%}$ [fb]	$0.038\ ^{+0.014}_{-0.009}$	$0.024\ ^{+0.009}_{-0.003}$

Table 20: Expected and observed number of events and corresponding background predictions in the high-$E_{\mathrm{T}}^{\mathrm{miss}}$ signal regions with transverse momenta above 60 GeV. The uncertainty in the total background prediction differs from the sum in quadrature of the individual components due to anti-correlation of fit parameters between the backgrounds.

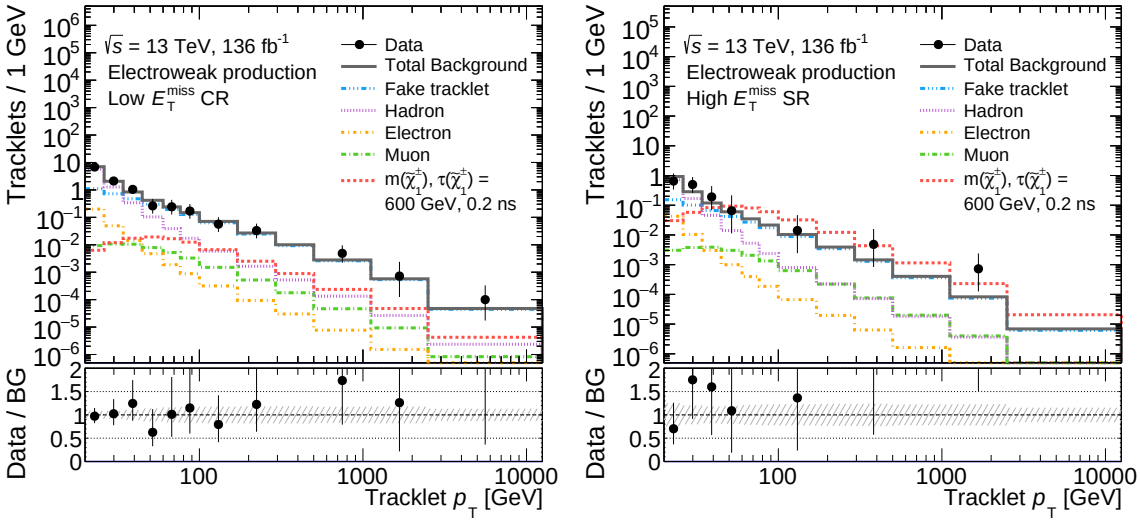

(a) Low-$E_{\mathrm{T}}^{\mathrm{miss}}$ CR (b) High-$E_{\mathrm{T}}^{\mathrm{miss}}$ SR

Figure 85: Fitting results of pixel-track p_{T} spectrum in the low-$E_{\mathrm{T}}^{\mathrm{miss}}$ CR and the the high-$E_{\mathrm{T}}^{\mathrm{miss}}$ SR for the electroweak production channel. The fake, hadron, electron and muon templates are fitted to observed data events in a background-only fit. An example of the expected-signal prediction with $m_{\tilde{\chi}_1^{\pm}} = 600$ GeV and $\tau_{\tilde{\chi}_1^{\pm}} = 0.2$ ns is overlaid in red. The last bin includes overflow entries. The bottom panel shows the ratio of data to the background-only prediction.

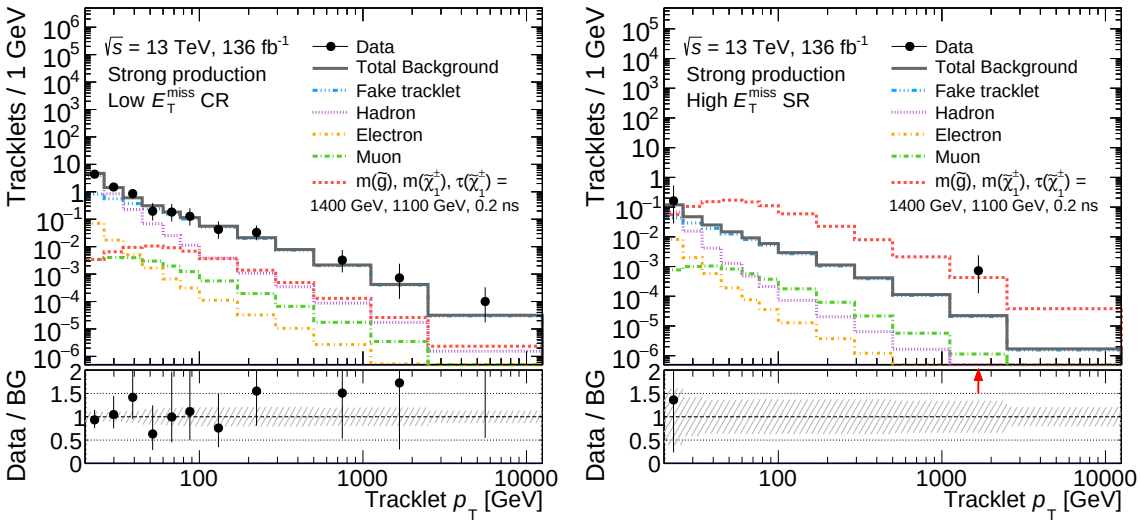

(a) Low-$E_{\mathrm{T}}^{\mathrm{miss}}$ CR (b) High-$E_{\mathrm{T}}^{\mathrm{miss}}$ SR

Figure 86: Fitting results of pixel-track p_{T} spectrum in the low-$E_{\mathrm{T}}^{\mathrm{miss}}$ CR and the high-$E_{\mathrm{T}}^{\mathrm{miss}}$ SR for the strong production channel. The fake, hadron, electron and muon templates are fitted to observed data events in a background-only fit. An example of the expected-signal prediction with $m_{\tilde{g}} = 1400$ GeV, $m_{\tilde{\chi}_1^{\pm}} = 1100$ GeV and $\tau_{\tilde{\chi}_1^{\pm}} = 0.2$ ns is overlaid in red. The last bin includes overflow entries. The bottom panel shows the ratio of data to the background-only prediction.

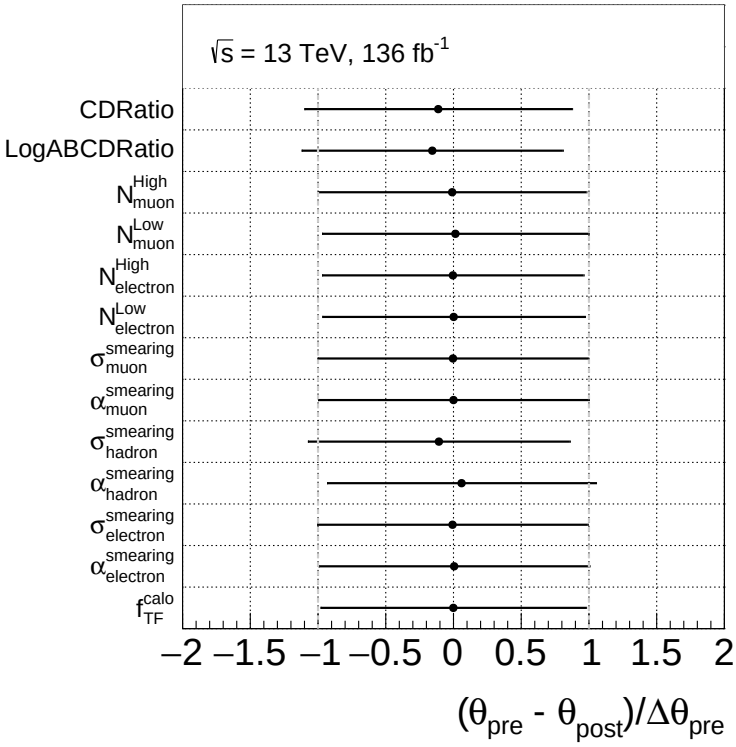

Figure 87: Pull of background-only fitting parameters (EWK channel)

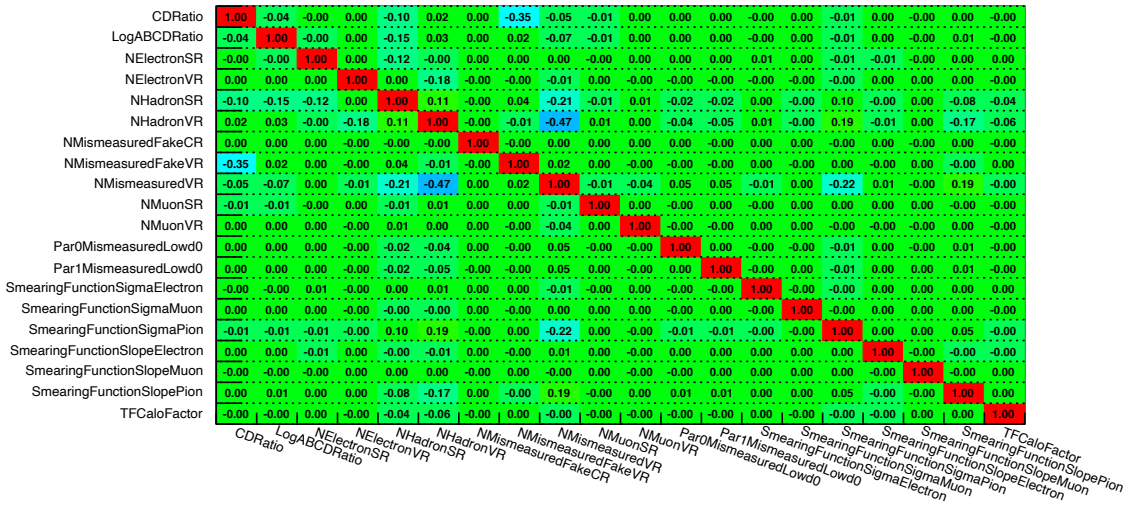

Figure 88: Correlation matrix of fitting parameters (EWK channel)

	EWK channel	Strong channel
CDRatio	0.14 ± 0.02	0.05 ± 0.01
LogABCDRatio	-0.012 ± 0.176	0.080 ± 0.324
$N_{electron}^{high-MET}$	0.41 ± 0.41	0.08 ± 0.08
$N_{electron}^{low-MET}$	1.95 ± 1.89	0.69 ± 0.67
$N_{hadron}^{high-MET}$	6.71 ± 3.39	0.62 ± 0.95
$N_{hadron}^{low-MET}$	52.52 ± 10.10	34.86 ± 8.19
$N_{fakeCR}^{verylow-MET}$	2155 ± 46	2611 ± 51
$N_{fakeCR}^{low-MET}$	494 ± 22	385 ± 20
$N_{fake}^{low-MET}$	40.62 ± 8.96	31.75 ± 7.77
$N_{muon}^{high-MET}$	0.31 ± 0.10	0.09 ± 0.03
$N_{muon}^{low-MET}$	0.79 ± 0.37	0.30 ± 0.13
p_0^{fake}	1.172 ± 0.113	0.996 ± 0.110
p_1^{fake}	0.171 ± 0.002	0.171 ± 0.002
$\sigma_{electron}^{smearing}$	0.00 ± 0.08	0.00 ± 0.08
$\sigma_{muon}^{smearing}$	0.00 ± 0.08	0.00 ± 0.08
$\sigma_{hadron}^{smearing}$	0.01 ± 0.08	0.01 ± 0.08
$\alpha_{electron}^{smearing}$	0.00 ± 0.12	0.00 ± 0.12
$\alpha_{muon}^{smearing}$	0.00 ± 0.09	0.00 ± 0.09
$\alpha_{hadron}^{smearing}$	-0.01 ± 0.09	-0.01 ± 0.09
f_{TF}^{calo}	0.00 ± 0.34	0.00 ± 0.31

Table 21: Summary of best fitted nuisance parameter values

the mass difference is shown in Figure 90 (b). The observed limit excludes chargino masses up to 210 GeV on the theoretical pure-higgsino prediction line shown with the grey dashed line.

For the wino search in the strong channel, the observed exclusion limit as a function of the gluino mass and the chargino mass is shown in Figure 91 (a) with $\tau_{\tilde{\chi}_1^\pm}$ = 0.2 ns and in Figure 91 (b) with $\tau_{\tilde{\chi}_1^\pm}$ = 1.0 ns. The maximum reach is 1.4 TeV (1.8 TeV) in the chargino mass and 2.1 TeV (2.18 TeV) in the gluino mass with $\tau_{\tilde{\chi}_1^\pm}$ = 0.2 ns (1.0 ns).

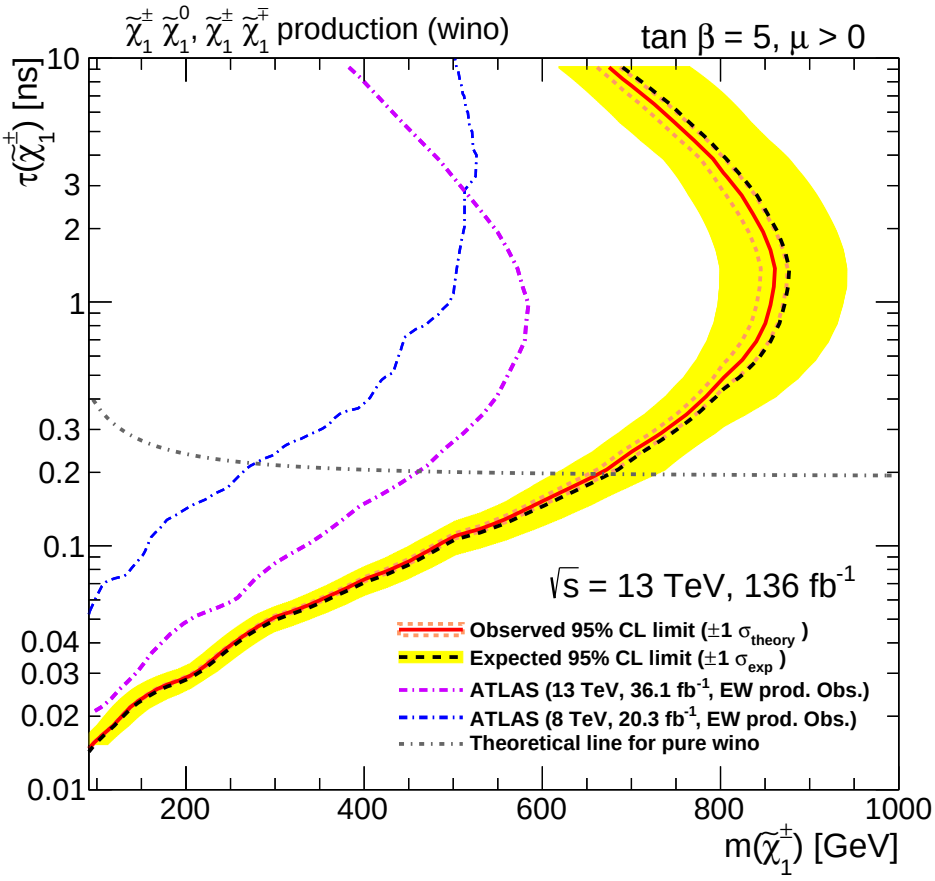

Figure 89: Exclusion limits at 95% CL obtained in the electroweak production channel with the pure-wino scenario. The limits are shown as a function of the chargino lifetime and mass. The black dashed line shows the median expected value, and the yellow band shows the 1σ uncertainty band around the expected limits. The red line shows the observed limits and the red dotted lines show the 1σ uncertainty from the signal cross-section. The blue and violet broken lines show the observed limits from the ATLAS results in Refs. [47] and [48] respectively.

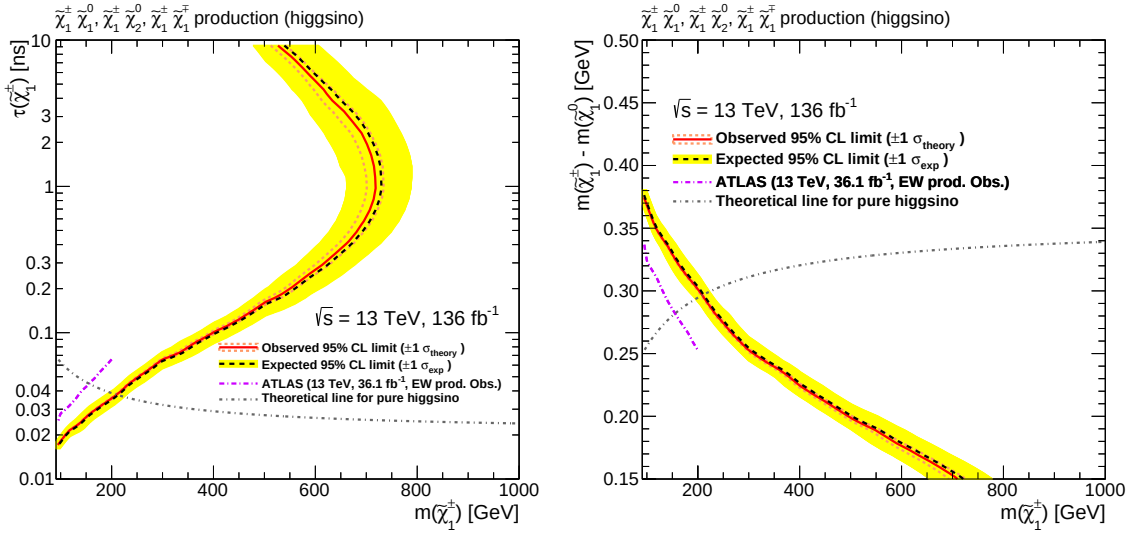

(a) (b)

Figure 90: Exclusion limits at 95% CL obtained in the electroweak production channel with the pure-higgsino scenario. The limits are shown separately for the higgsino lifetime or mass splitting as a function of the chargino mass. The black dashed line shows the median expected value, and the yellow band shows the 1σ uncertainty band around the expected limits. The red line shows the observed limits and the red dotted lines show the 1σ uncertainty from the signal cross-section. The violet broken line shows the observed limits from the previous ATLAS result [49].

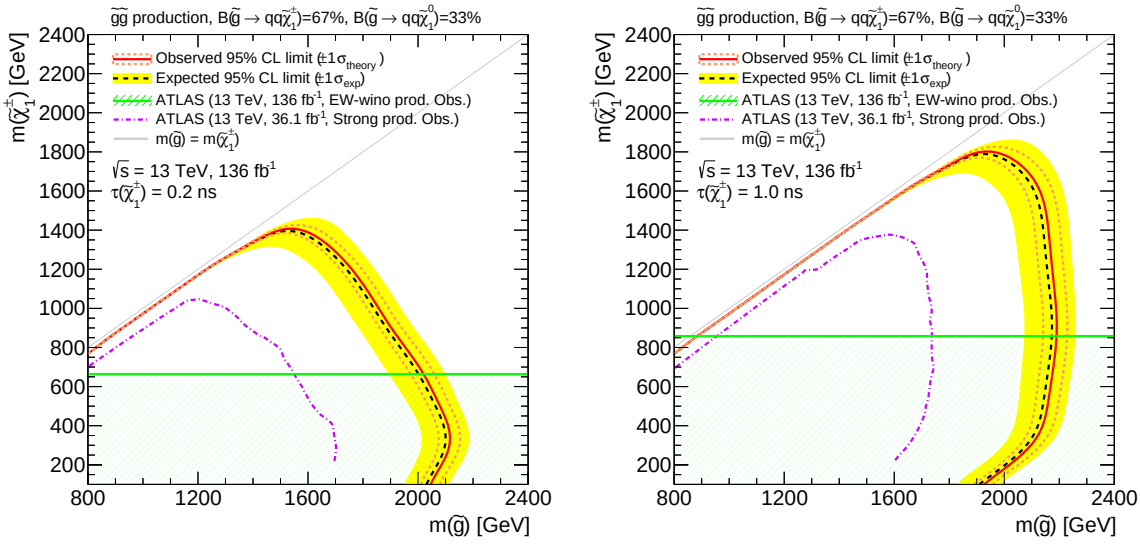

(a) (b)

Figure 91: Exclusion limits at 95% CL obtained in the strong production channel. The limits are shown as a function of the lightest chargino's mass versus the gluino's mass, for chargino lifetimes of (a) 0.2 ns and (b) 1.0 ns. The black dashed line shows the median expected value, and the yellow band shows the 1σ uncertainty around the expected limits. The red line shows the observed limits and the red dotted lines show the 1σ uncertainty from the signal cross-section. The observed exclusion limits from this search in the direct electroweak wino production channel in the minimal AMSB model with (a) $\tau_{\tilde{\chi}_1^\pm}$ = 0.2 ns and (b) $\tau_{\tilde{\chi}_1^\pm}$ =1.0 ns are overlaid in green. The violet broken line shows the observed limits from the previous ATLAS result [47].

7 Discussions and Prospects

In this chapter, the results of the search performed in the previous chapter are compared with the past and other analyses' results. Then possible improvements that could be achieved in the future search are discussed and summarized. Finally, preliminary results of some ideas are shown.

7.1 Discussions and Comparisons

7.1.1 Result of Wino Search in Electroweak Channel

Compared to the previous analysis, the observed limit for the chargino mass on the theoretical pure-wino line is improved from 460 GeV to 660 GeV. The difference in signal production cross-sections is about a factor of 5. The integrated luminosity increased from 36.1 fb^{-1} to 136.3 fb^{-1}, but it contributes only a factor of 2 by simple approximation. Other contributions come from kinematic selections and calorimeter veto. The threshold for $E_{\text{T}}^{\text{miss}}$ and leading jet p_{T} is 140 GeV for each in the previous analysis, while it has changed to 200 GeV and 100 GeV respectively in this analysis. As a result, the signal and background yields decrease to about 80% and 40% respectively, and then the significance of the signal improved by a factor of 25%. Calorimeter veto requirement strongly suppresses background events, especially the electron and the hadron backgrounds. As shown in the cut-flow tables 10 and 12, it reduces the background by more than 95% in the hadron background dominant low-p_{T} region. These optimizations improve the sensitivity than statistical gain.

Figure 92 shows the observed limit overlaid with the result of the full Run-2 disappearing track analysis in the CMS experiment. Compared to the CMS result, this work has higher sensitivity in the short lifetime region, such as $\tau_{\tilde{\chi}_1^\pm}$ = 0.2 ns, while has lower sensitivity in the long lifetime region. There are some possible reasons. One big difference between this analysis and the CMS analysis is the sensitive volume. In this analysis, only 4-layer tracks are used for the search, however, in the CMS analysis, 4-layer tracks, 5-layer tracks, and more than 6-layer tracks are used. Therefore, the CMS analysis has higher sensitivity in the long lifetime region. It is not obvious that the ATLAS analysis could achieve similar sensitivity in the long lifetime region by using longer tracks. The coverage of the inner tracker is almost the same in both ATLAS and CMS experiments in a range of about R < 1.1 m, but it consists of full silicon trackers in the CMS while silicon trackers cover about only R < 0.5 m in the ATLAS. The TRT detector has higher activities compared to silicon trackers in a high pile-up environment and needs to figure out a way to be used as a disappearing track condition. This is an advantage for the CMS to search for the long lifetime region. In contrast, for the short lifetime region, the 4-th layer locates at R = 122 mm in the ATLAS while it locates at R = 160 mm in the CMS. Hence, the 4-layer track in the

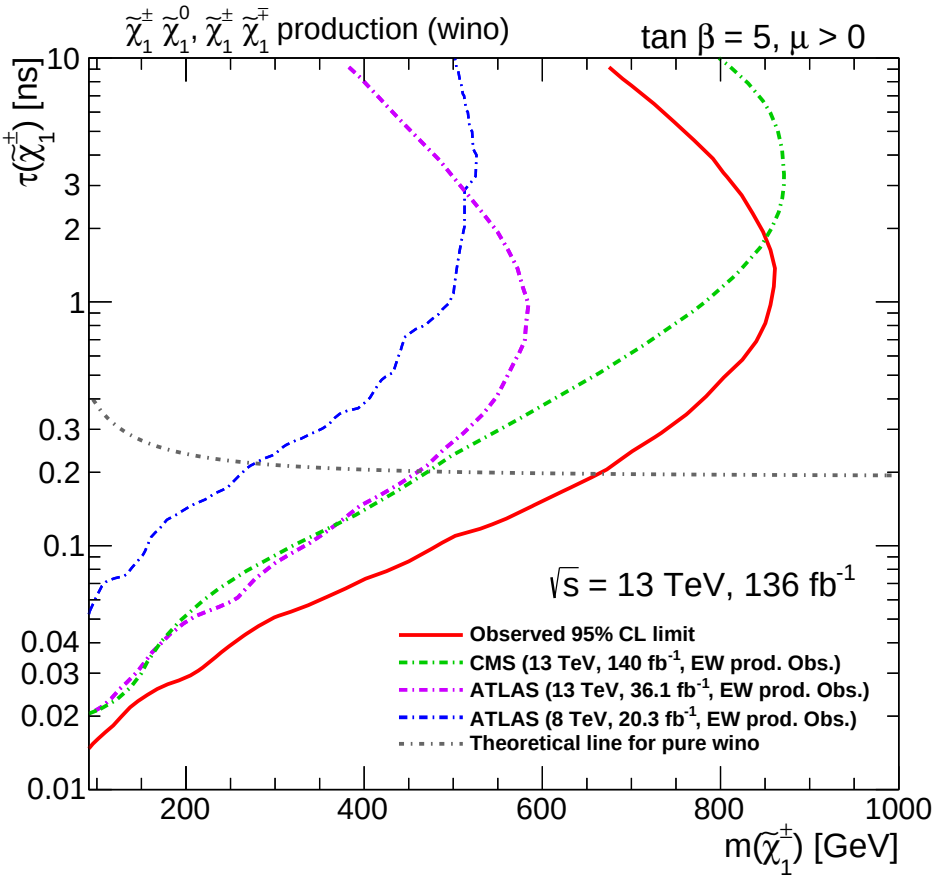

Figure 92: Exclusion limits for the wino search in the EWK channel with the result of disappearing track search in CMS experiment [50].

ATLAS is geometrically shorter than the one in the CMS. This is an advantage for the ATLAS to search for the short lifetime region.

According to the hepdata [51], it is expected that 1.73 (2.85) events in the 4-layer track category (sum of all categories) for the signal at ($m_{\tilde{\chi}_1^{\pm}}$, $\tau_{\tilde{\chi}_1^{\pm}}$) = (700 GeV, 0.3 ns) in the CMS analysis at 41.5 fb^{-1}, while 2.2 events are expected in this analysis with the same signal point and integrated luminosity. The observed number of events is 33 in the CMS 4-layer track category with the 2017+2018 dataset [50], while it is 3 events in this analysis with the full Run-2 dataset. The thresholds of $E_{\mathrm{T}}^{\mathrm{miss}}$ and the leading jet p_{T} are 120 GeV and 110 GeV respectively in the CMS, while there are 200 GeV and 100 GeV in this analysis. Tight $E_{\mathrm{T}}^{\mathrm{miss}}$ cut loses signal efficiency to some extent, but it has a strong background rejection power. These factors might cause differences in sensitivity.

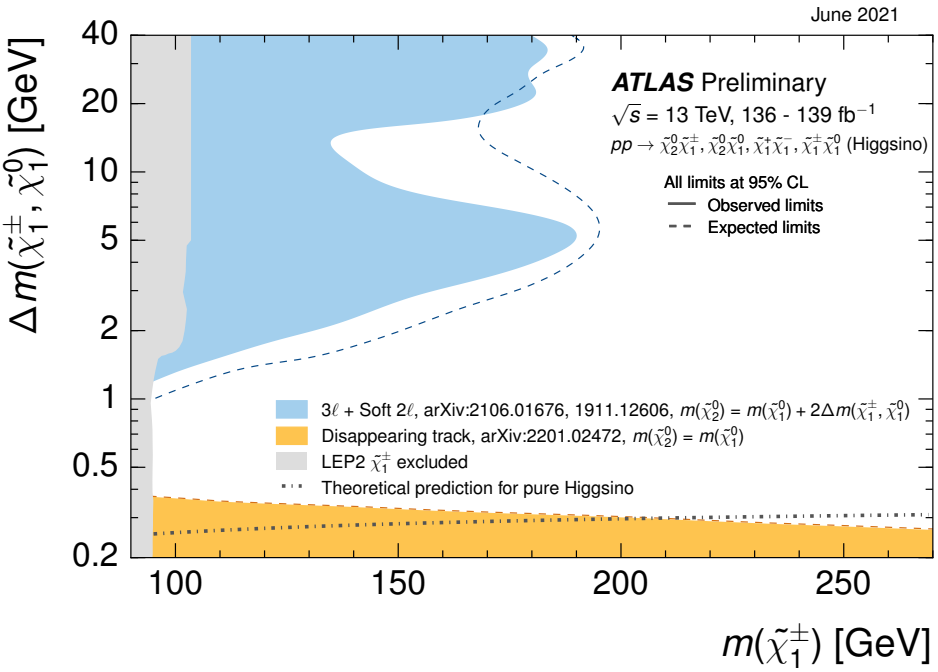

Figure 93: Summary plot for higgsino search in the ATLAS experiment [52]. The production cross-section assumes pure higgsinos.

7.1.2 Result of Higgsino Search in Electroweak Channel

Figure 93 shows a summary plot for higgsino search in the ATLAS experiment. The orange area is the result of this work and covers a short lifetime region up to 210 GeV at the pure-higgsino prediction line. The multi-lepton analysis, which focuses on the leptonic decay of charginos, covers a region of $\Delta m_{\tilde{\chi}_1}$ > 1 GeV. Along with $\Delta m_{\tilde{\chi}_1}$, lifetime $\tau_{\tilde{\chi}_1^\pm}$ becomes shorter and decay products of the charginos become higher momentum. Lifetime is $\tau_{\tilde{\chi}_1^\pm}$ < 1 ps at $\Delta m_{\tilde{\chi}_1}$ = 1 GeV, so charginos decay instantly in this region. There is an uncovered region between the disappearing track analysis and the multi-lepton analysis. In this region, charginos are too short to reconstruct track and also decay products are too soft to identify particle type. Therefore, it is important to develop a new approach to prove this region.

7.1.3 Result of Wino Search in Strong Channel

Figure 94 shows a comparison of results between the disappearing track search in the strong channel and an inclusive SUSY search in the 0-lepton channel at the ATLAS experiment. The inclusive 0-lepton search is performed by using multi-jets and $E_{\mathrm{T}}^{\mathrm{miss}}$. The same signal as the disappearing track search in the strong channel can be also explored by the 0-lepton analysis because if charginos are missed they are observed as missing energy. Furthermore, the chargino mass is almost the same as the neutralino mass

in the disappearing track analysis, so the kinematics of signal topology is the same. Compared to the 0-lepton analysis, the maximum mass reach for the gluino is low, while the maximum mass reach for the chargino is high, especially near the diagonal region. There are some possible reasons. In this analysis, kinematical requirements for the strong channel are optimized to the diagonal region by relaxing the threshold for jets p_{T}, while the 0-lepton analysis prepared many signal regions and chose the optimal kinematical chain for each phase space. In addition to the difference in kinematical requirements, the disappearing track analysis loses some efficiency by requiring a disappearing track object. That is why the 0-lepton analysis has better sensitivity in high gluino mass with low LSP mass region. In contrast, the 0-lepton analysis is not so good in the diagonal region because the mass difference between the gluino and the LSP is low and it results in a low jet activity. Loose jet requirements bring up many background events, but a disappearing track object has a strong power of background reduction. Hence, this analysis has good sensitivity in the diagonal region. Of course, the degree depends on the

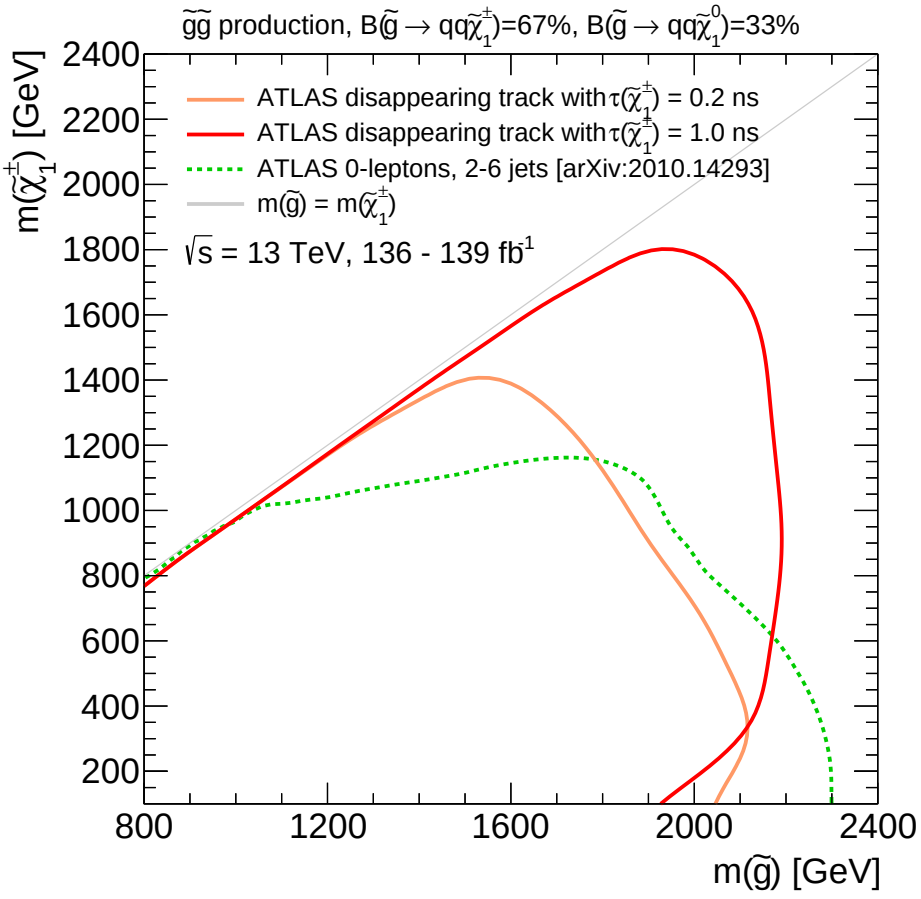

Figure 94: Summary plot of search for gluinos decaying to the LSPs in the ATLAS experiment. The inclusive 0-lepton search [53] assumes $B(\tilde{g} \to qq\tilde{\chi}_1^0) = 100\%$, but the sensitivity should be the same for $B(\tilde{g} \to qq\tilde{\chi}_1^{\pm}) = 67\%$ and $B(\tilde{g} \to qq\tilde{\chi}_1^0) = 33\%$ because charginos are observed as missing energy if the lifetime of chargino is short enough.

lifetime.

The CMS also performed the search for gluinos with disappearing track objects [54]. The analysis method is similar to the 0-lepton analysis rather than this analysis. They just include disappearing track objects as a variable to categorize signal regions in the multi-bin analysis. The benchmark signal points are different from this analysis, so a fair comparison is difficult. It seems the sensitivity in the diagonal region with a low lifetime (e.g. $\tau_{\tilde{\chi}_1^\pm} = 0.2$ ns) is similar to this analysis, however, they have better sensitivities in other phase spaces.

7.2 Possible Items for Improvements of Sensitivity

The sensitivity of the search for long-lived charginos has been improved by increasing the statistics nearly four times and implementing the additional requirement for the background reduction. However, there is still much room for improvement in this analysis. In this section, several ideas and on-going efforts for future disappearing track search are discussed.

Improvements in the sensitivity are achieved by increasing signal efficiency and decreasing the number of background events. There are limited ways to increase signal efficiency: to improve trigger efficiency or track efficiency.

Disappearing Track Trigger The special trigger which is a combination of $E_{\mathrm{T}}^{\mathrm{miss}}$ and disappearing track object is developed for the disappearing track analysis in Run-3. The boosted decision tree (BDT) is used to distinguish signal tracks and background tracks. Figure 95 shows the integrated signal efficiency with respect to the L1 trigger ($E_{\mathrm{T}}^{\mathrm{miss}} > 50$ GeV) selection. It is expected to improve trigger efficiency within an acceptable trigger rate of 10 Hz at HLT. However, it needs further study to discuss the exact gain because $E_{\mathrm{T}}^{\mathrm{miss}}$ is one of the strong variables of background reduction, and relaxing the $E_{\mathrm{T}}^{\mathrm{miss}}$ threshold brings up many background events.

Track Reconstruction The disappearing track search reported in this thesis has been performed by using only 4-layer pixel-tracks. Therefore, simply by using more shorter or longer, i.e. 3-layer pixel-tracks or pixel+SCT tracks, wider phase spaces can be explored. Expected sensitivity by using various lengths of tracks is discussed in the next sub-section.

In contrast with signal efficiency, there are several ideas to reduce background events.

Vertex Constraint One of the main issues with a short track is poor momentum resolution. Since the signal track should come from the beam origin, recalculating track parameters with primary vertex as an additional hit improves momentum resolution. Figure 96 shows the residual distribution of p_{T} for 3-layer tracks and 4-layer tracks with and without vertex constraint. Signal charginos have high p_{T} while background tracks derived from charged particles tend to have low p_{T}, so the improvement of momentum resolution gives better background separation.

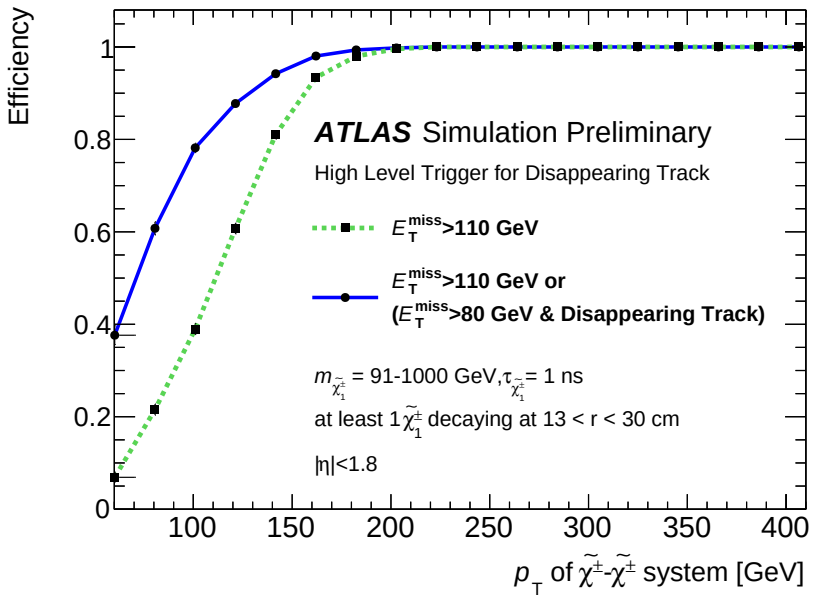

Figure 95: An integrated HLT trigger efficiencies w.r.t. L1 $E_{\mathrm{T}}^{\mathrm{miss}}$ trigger for the chargino-pair events [55].

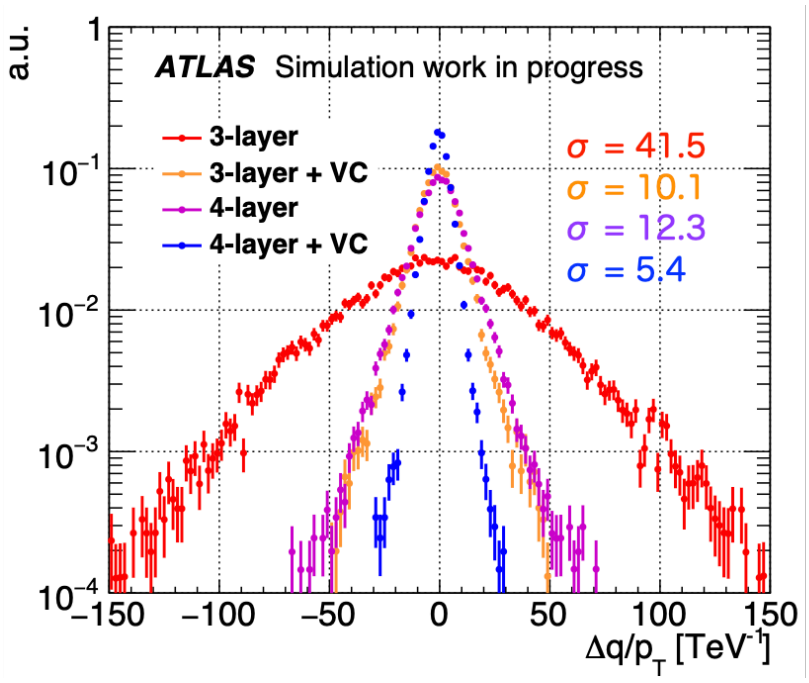

Figure 96: The residual distribution of q/p_{T} for the signal charginos with various tracks.

Pixel dE/dx Since the target signal is a massive charged particle, its β (=v/c) is relatively low and tends to have high dE/dx. As a chargino with a long lifetime ($\tau_{\tilde{\chi}_1^\pm} > 4.0$ ns) is searched by using dE/dx, the dE/dx is useful for chargino search and its technique is already established. Furthermore, the dE/dx is calculated from only pixel detectors, so no special treatment is required for the 4-layer track. Additional study is required for the 3-layer or 2-layer track, though. Figure 97 shows the dE/dx distribution of pixel-tracks for the signal MC (wino) with $\tau_{\tilde{\chi}_1^\pm} = 1.0$ ns and background events. As shown in Figure 97(a), heavier charginos tend to have large dE/dx. Figure 97(b) shows the comparison to background events. The signal charginos have larger dE/dx than background events. It is known that the dE/dx value in data is lower than the simulated value due to the mismodeling of radiation damages to pixel sensors, but the difference is expected to be an order of 10%. Only the fake background has broad tails, while other background components have narrow and similar shapes with each other. Figure 98 shows the efficiencies with a lower limit for dE/dx values. Even setting just a loose lower limit is expected to reduce the background events. Since the charginos with low lifetime like higgsinos need to be boosted to reconstruct tracks, the dE/dx value becomes low along with increasing β.

Soft Pion Tagging The fake track tends to be isolated from other objects and can accidentally pass requirements for event selections. Hence, there is a very limited way to reduce the fake background. Because the fake tracks arise from random combinations of pixel hits, the number of fake backgrounds increases dramatically as tracks get shorter. If the soft pion, the decay product of charginos, can be tagged, the signal track can be identified as a kinked track which consists of chargino's short track with p_{T} of O(100 GeV) and pion's large radius track with p_{T} of O(100 MeV). Therefore, it can reduce background events, including fake tracks.

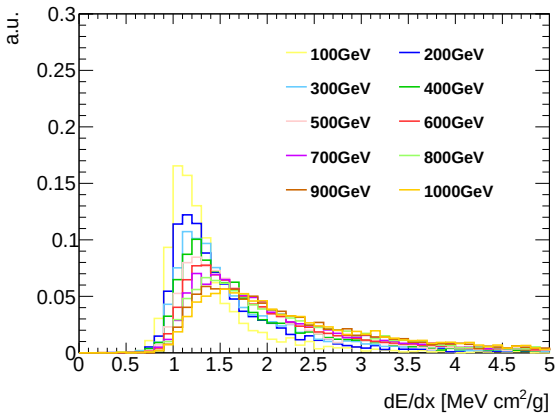

(a) Mass dependence of signal charginos

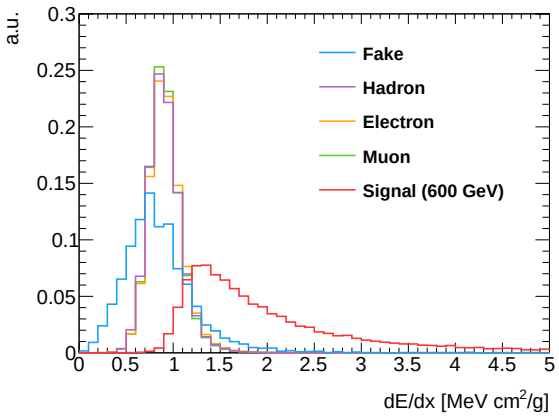

(b) Comparison between signal and backgrounds

Figure 97: The dE/dx distribution of pixel-tracks.

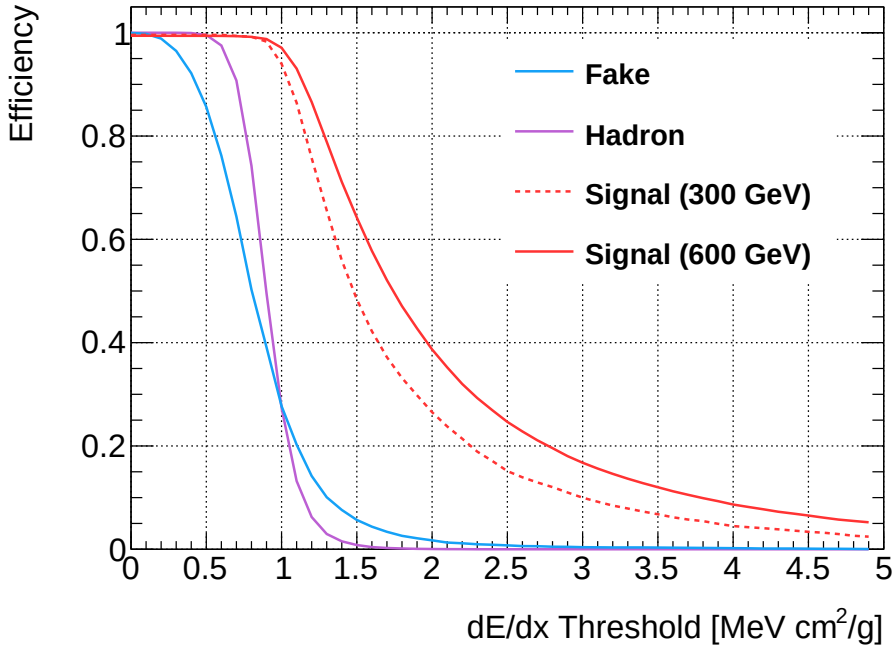

Figure 98: Efficiency with a lower limit for dE/dx value.

Figure 99(a) shows reconstruction efficiency for the soft pion as a function of the truth p_{T}. Performance is evaluated by using the higgsino MC samples. The efficiency achieved 40 - 50 % at p_{T} = 300 MeV. To reconstruct the large radius soft pion track, combinations of three SCT space points are required to have a p_{T} > 200 MeV within ΔR < 0.8 from the pixel-track as a seed. Then track seeds are extended into tracks with at least 6 hits. Figure 99(b) shows vertex reconstruction efficiency as a function of the soft pion production vertex position. Both denominator and numerator are considered only truth-matched tracks. A two-track vertex fit is performed for all combinations of pixel tracks and large radius tracks within ΔR < 1.5. The fitting procedure is described in Ref. A, and vertex radius is required to be 85 mm < r < 300 mm. The tagging efficiency achieved 80 - 90 % for the signal tracks. As described in Section 2.5, the pion p_{T} is correlated with the mass difference $\Delta m_{\tilde{\chi}_1}$, soft pion tagging is useful for the higgsino search rather than the wino search. Since many large radius tracks are originating from hadronic interactions with detector materials, the study of background rate is important to evaluate the gain of this technique.

7.3 Expected Sensitivity in Future Search

In this sub-section, the expected sensitivity of future searches with various lengths of tracks is discussed. The dependences of track length, such as the momentum resolution and the tracking efficiency are not

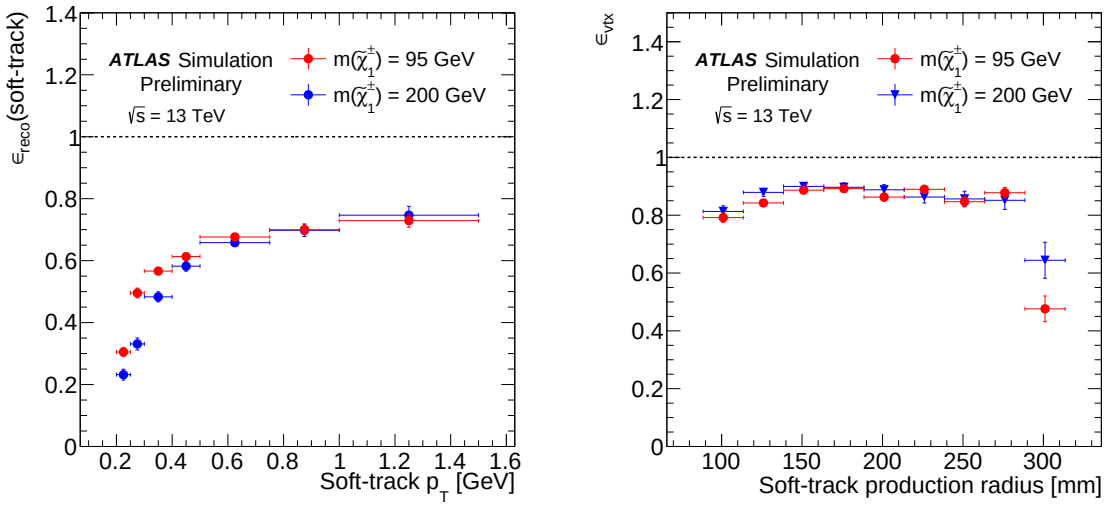

(a) Soft pion track efficiency as a function of the truth p_T

(b) Vertex efficiency as a function of the production radius of the pion

Figure 99: Reconstruction efficiency for (a) soft pion tracks and (b) vertex of the chargino and pion [56].

considered and the overall track efficiency including selection efficiency is assumed to be 50%. An increase in the number of backgrounds is also not considered by assuming the background can be removed by using ideas in the previous sub-section. So only the signal gain by using the various lengths of tracks is considered. These assumptions might be conservative for long tracks. Because current track efficiency is already higher than 50% and the charged particle background decreases thanks to the higher momentum resolution. Moreover, the fake background also decreases along with an increasing number of hits constituting a track. For the opposite reasons, the assumptions might be optimistic for short tracks. But these are not unfeasible assumptions by future efforts.

For Run-2 or Run-3 detectors, it is promising to use the 3-layer track (R = 88.5 mm) to the 7-layer track (R = 443 mm) as a disappearing track. In order to use the longer track, i.e. the 8-layer track, further study of a disappearing track condition is required because the SCT veto is not available anymore and the TRT veto is not strong as the SCT veto. To use the shorter track, i.e. the 2-layer track, further ideas to reduce background events need to be considered in addition to the ideas listed in the previous sub-section. The disappearing track is required to be consisting of only barrel layers. If an end-cap layer is included the length of the lever arm is not determined and treatment becomes difficult because the momentum resolution is changing. Figure 100 shows the distribution of the chargino decay position. The red dotted lines indicate the detector position of the Pixel and the SCT. The chargino tends to fly toward the central region, so requiring only barrel layers does not lose acceptance so much. Figure

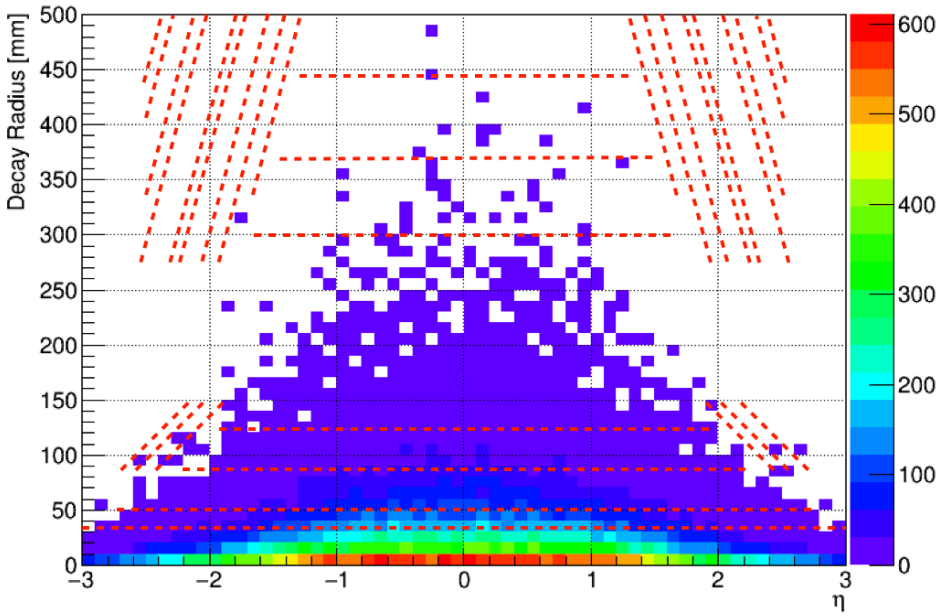

Figure 100: Decay position of the signal chargino. The red dotted lines indicate the detector position of the Pixel and the SCT detectors.

101 shows how much the signal efficiency increases as a function of the lifetime. The green line is a promising scenario and it is expected to increase twice for the various lifetime regions and 4 times for the short lifetime region. The orange line is an aggressive scenario and the statistics in the short lifetime region increase dramatically. Figure 102 shows the expected sensitivity by using various lengths of tracks with the same statistics as the Run-2. Improvements of more than 100 GeV in any lifetime region are expected even the promising configuration. The expectation of the aggressive scenario in the short lifetime region is not accurate due to a lack of signal samples.

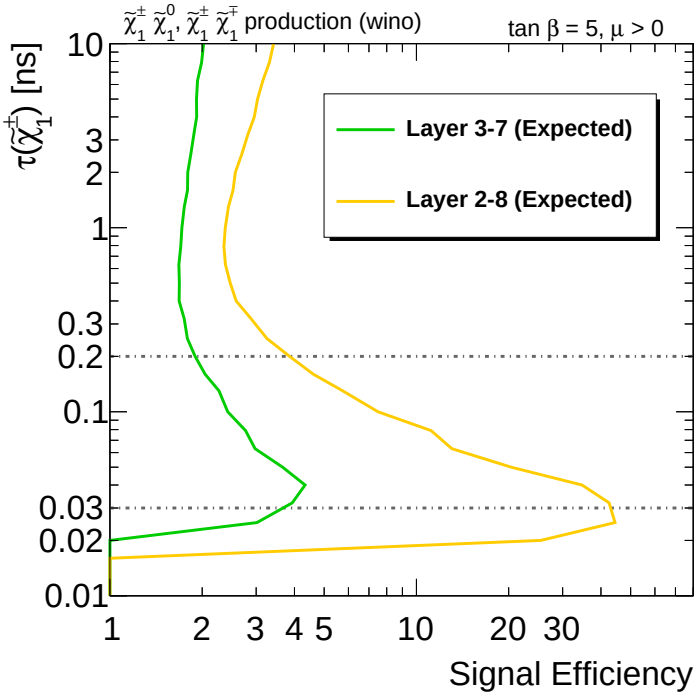

Figure 101: Expected signal increases by using various lengths of tracks. The green line is using 3-layer tracks to 7-layer tracks, and the orange line is using 2-layer tracks to 8-layer tracks. Gray dotted lines show $\tau_{\tilde{\chi}_1^{\pm}}$=0.2 ns and 0.03 ns, which are representative lifetimes for wino and higgsino respectively.

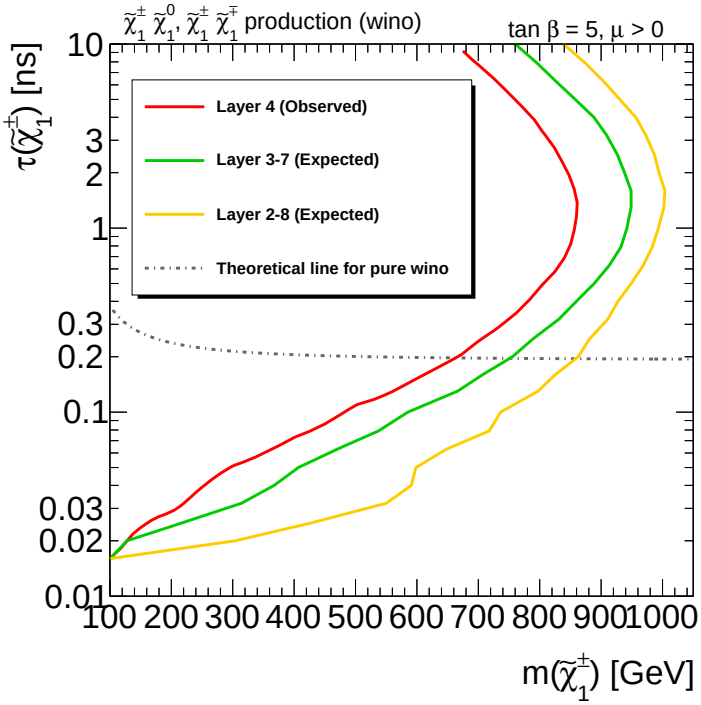

Figure 102: Expected sensitivity in future search with various lengths of tracks. The green line is an expected limit by using 3-layer tracks to 7-layer tracks with the Run-2 dataset, while the orange line is an expected limit with 2-layer tracks to 8-layer tracks. The red line is the observed limit performed in this paper. The gray dotted line shows the theoretical line for pure wino.

7.4 Chargino Mass Reconstruction

After the discovery of the signal, it is important to determine the mass of charginos. Since the mass of the lightest chargino and the lightest neutralino are highly degenerate in the scenario of this analysis, the measurement of the chargino mass corresponds to the measurement of the dark matter mass.

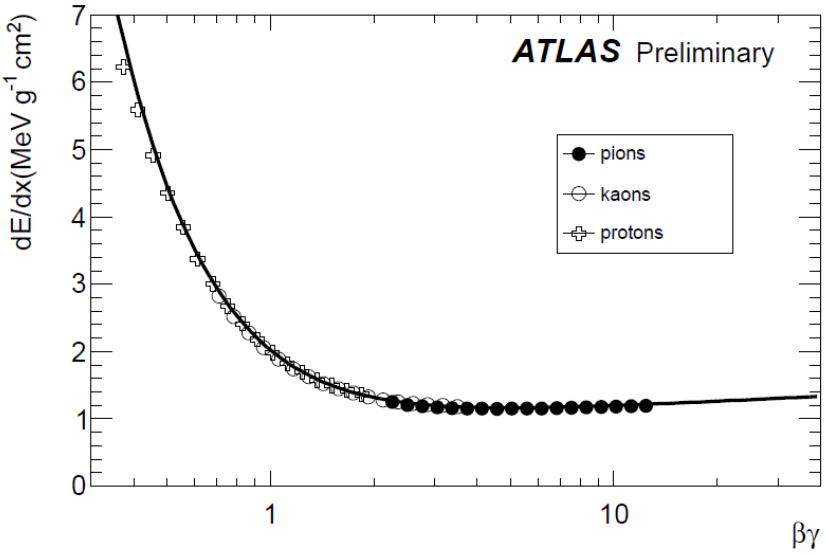

Figure 103: The Pixel $\mathrm{d}E/\mathrm{d}x$ for standard particles [57].

The energy loss of a charged particle is described by the Bethe-Bloch formula. Figure 103 shows the Pixel $\mathrm{d}E/\mathrm{d}x$ as a function of $\beta\gamma$ for pions, kaons, and protons, where γ is the Lorentz factor defined as $\gamma = 1/\sqrt{1-\beta^2}$. Since the $\mathrm{d}E/\mathrm{d}x$ follows the function of $\beta\gamma$ and also particle mass M can be expressed as $M = p/(\beta\gamma)$, the chargino mass can be reconstructed from the $\mathrm{d}E/\mathrm{d}x$ and its momentum p. However, a poor momentum resolution is the one of main issues for disappearing track searches. Figure 104 shows the $\mathrm{d}E/\mathrm{d}x$ as a function of the track momentum for the disappearing track candidates of the $(m_{\tilde{\chi}_1^\pm}, \tau_{\tilde{\chi}_1^\pm})$ = (600 GeV, 1.0 ns) signal sample . The lower cut for $\mathrm{d}E/\mathrm{d}x > 1.0$ [MeV $\cdot$ cm^2/g] is applied to reduce the contamination of background tracks. Due to a poor momentum resolution, the $\mathrm{d}E/\mathrm{d}x$ seems to be independent of the p_T.

To solve this issue, two disappearing tracks are required so that their p_T can be mathematically calculated from the directions of charginos and the $E_\mathrm{T}^\mathrm{miss}$. This method is called the collinear approximation and is used to reconstruct the invariant mass in $\tau\tau$ decays of a higgs boson. The same strategy is also used in Ref.[58] to reconstruct the momenta of charginos and the mass. In Ref.[58], the measurement at FCC (Future pp Circular Collider) with $\sqrt{s}$ = 100 TeV is assumed, and the track β is assumed to be measured by the timing-capable sensors instead of the pixel $\mathrm{d}E/\mathrm{d}x$. Figure 105 illustrates the principle of chargino

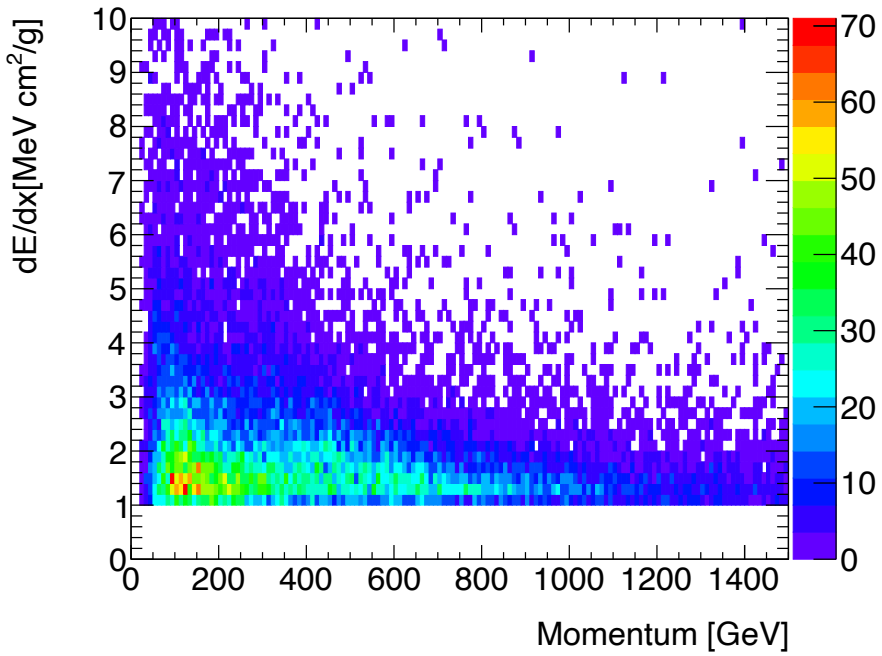

Figure 104: The $\mathrm{d}E/\mathrm{d}x$ vs momentum plot for the reconstructed disappearing track candidates.

mass reconstruction. In an ideal situation, the $E_{\mathrm{T}}^{\mathrm{miss}}$ corresponds to the vector sum of neutralinos' p_{T}. Since the p_{T} of neutralino is almost the same as the p_{T} of chargino due to the small mass splitting, the vector sum of charginos' p_{T} corresponds to the $E_{\mathrm{T}}^{\mathrm{miss}}$. Track momenta are calculated from the following

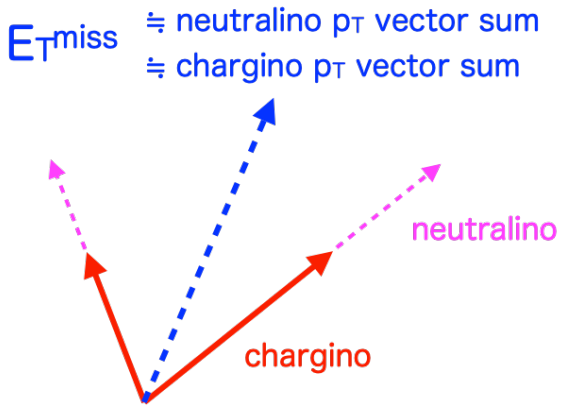

Figure 105: Mathematical reconstruction of chargino p_{T}.

formula :

$$p_{T,1} = + E_{\mathrm{T}}^{\mathrm{miss}} \cdot \frac{\cos\phi_0 \cdot \sin\phi_2 - \sin\phi_0 \cdot \cos\phi_2}{\cos\phi_1 \cdot \sin\phi_2 - \sin\phi_1 \cdot \cos\phi_2}, \tag{29}$$

$$p_{T,2} = - E_{\mathrm{T}}^{\mathrm{miss}} \cdot \frac{\cos\phi_0 \cdot \sin\phi_1 - \sin\phi_0 \cdot \cos\phi_1}{\cos\phi_1 \cdot \sin\phi_2 - \sin\phi_1 \cdot \cos\phi_2}, \tag{30}$$

where ϕ_0 is the direction of $E_{\mathrm{T}}^{\mathrm{miss}}$, ϕ_i and $p_{T,i}$ $(i = 1, 2)$ are track parameters for each track.

Figure 106 shows the residual distribution of $1/p_{\mathrm{T}}$ for various lengths of tracks and inclusive tracks with p_{T} calculated by the collinear approximation technique. By using the collinear approximation technique, better p_{T} resolution than standard tracks can be achieved for any track. The calculation fails when the direction of $E_{\mathrm{T}}^{\mathrm{miss}}$ is not inside the acute angle of the two tracks. The p_{T} reconstruction efficiency is 98% for the 600 GeV EWK signal sample. To estimate the number of events with the two disappearing tracks requirement, the following event selection is applied.

- The $E_{\mathrm{T}}^{\mathrm{miss}}$ triggers
- $E_{\mathrm{T}}^{\mathrm{miss}} > 100$ GeV
- $p_{\mathrm{T}} > 100$ GeV for the leading jet
- $\Delta\phi_{\mathrm{min}}^{\mathrm{jet-E_T^{miss}}} > 0.4$

Since background events can be reduced by $O(10^{-5})$ for each disappearing track, the applied event selection is loose. As a disappearing track, from 4-layer to 7-layer track is considered.

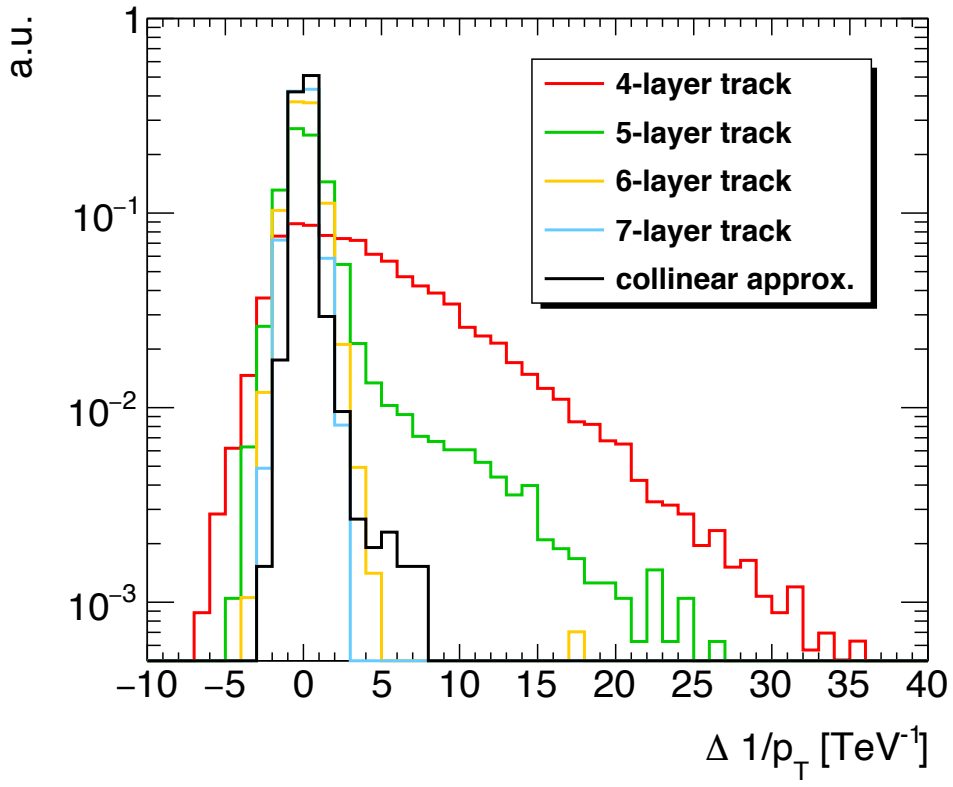

Figure 106: Comparison of the p_{T} resolution between the reconstructed track parameter and calculated by the collinear approximation.

Figure 107 shows the dE/dx as a function of the track momentum reconstructed by using the collinear approximation technique for the $(m_{\tilde{\chi}_1^\pm}, \tau_{\tilde{\chi}_1^\pm})$ = (600 GeV, 1.0 ns) signal sample. The lower cut for dE/dx > 1.0 [MeV $\cdot$ cm^2/g] is applied to reduce contamination of background tracks. The green dotted line is the expected line for proton and gray dotted lines are expected lines for $m_{\tilde{\chi}_1^\pm}$ = 91 GeV $\sim$ 1000 GeV by almost 100 GeV step. The red dotted line is a fitted line with the following function:

$$M_{\text{reco}} = p \cdot \left(\frac{dE/dx - \text{B}}{\text{A}} \right)^{\frac{1}{\text{C}}}, \tag{31}$$

where A = 0.9305 [MeV $\cdot$ cm^2/g], B = 1.039 [MeV $\cdot$ cm^2/g], and C = 2.074. This function is motivated by the Bethe-Bloch formula and constant parameters are measured with minimum-bias data [59]. The best-fit value is M_{reco} = 535 GeV and it is lower than the true value. Without the collinear approximation technique, the momentum resolution is too bad to reconstruct their particle mass.

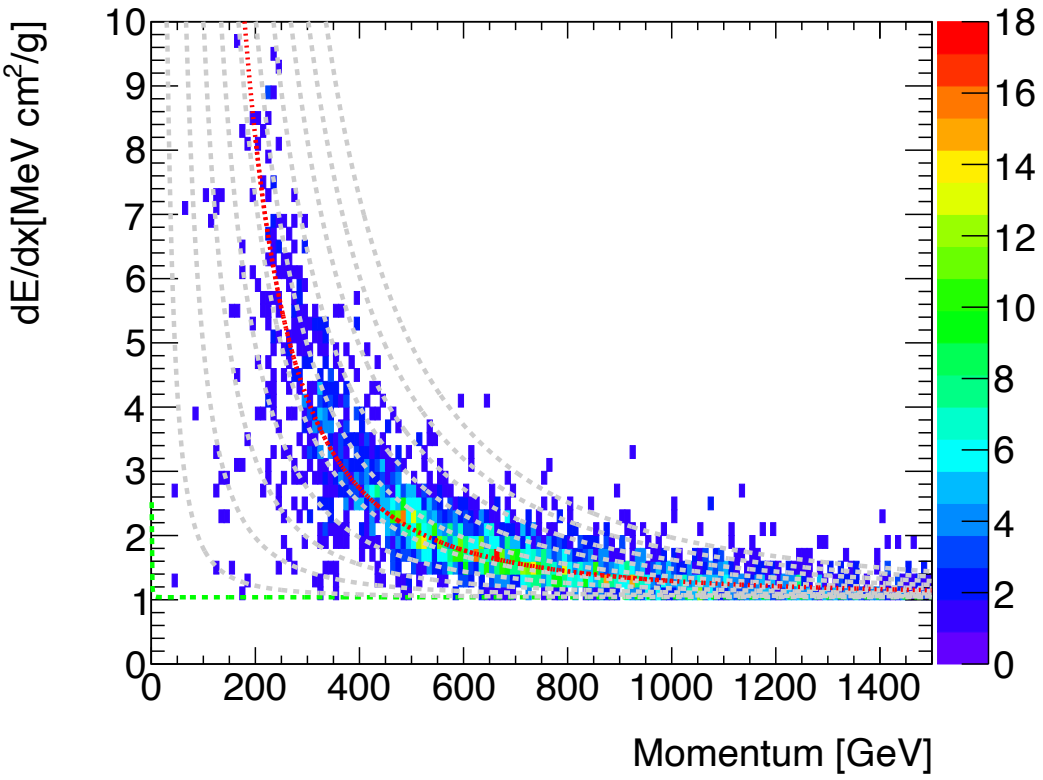

Figure 107: The dE/dx vs momentum plot for the $(m_{\tilde{\chi}_1^\pm}, \tau_{\tilde{\chi}_1^\pm})$ = (600 GeV, 1.0 ns) signal sample by using the collinear approximation to reconstruct the p_{T}. The green dotted line is the expected line for the proton and each gray dotted line is for the signal charginos with $m_{\tilde{\chi}_1^\pm}$ = 91 GeV $\sim$ 1000 GeV by almost 100 GeV step which is listed in Table 3. The red dotted line shows the best-fit value with the expected function.

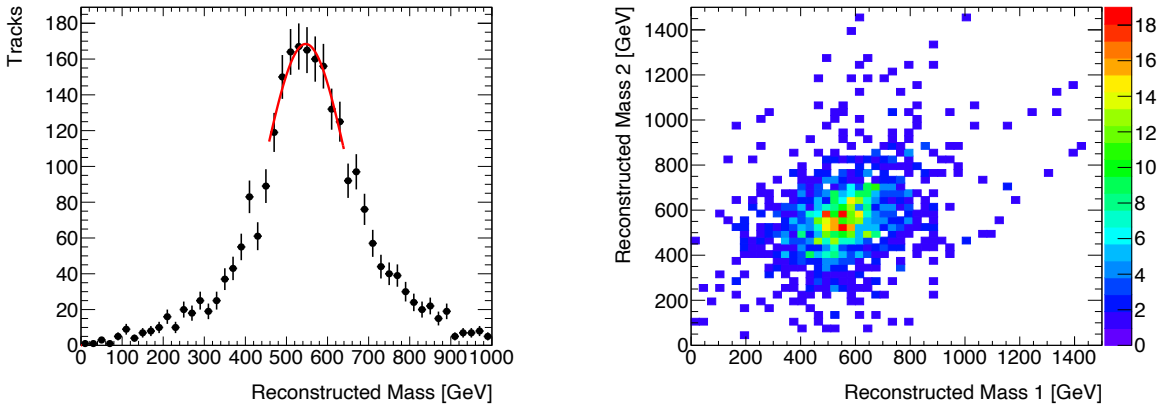

(a) Projection to the 1-D histogram

(b) Scatter plot in the 2-D histogram

Figure 108: Reconstructed chargino mass distribution.

Figure 108 shows the 1-D and 2-D histograms of the reconstructed mass distribution. This time, particle mass is measured by fitting the 1-D histogram with a gaussian in the range of $[\mu - \sigma, \mu + \sigma]$. Figure 109 shows the ratio of the reconstructed mass to the truth mass as a function of a chargino mass. Reconstructed masses tend to be estimated lower overall, and the ratio is almost flat up to 1 TeV. The current $\mathrm{d}E/\mathrm{d}x$ value is calculated using a truncated mean [57], and it is known that this method can cause the bias. This bias can be removed by improving the calculation of the $\mathrm{d}E/\mathrm{d}x$ value.

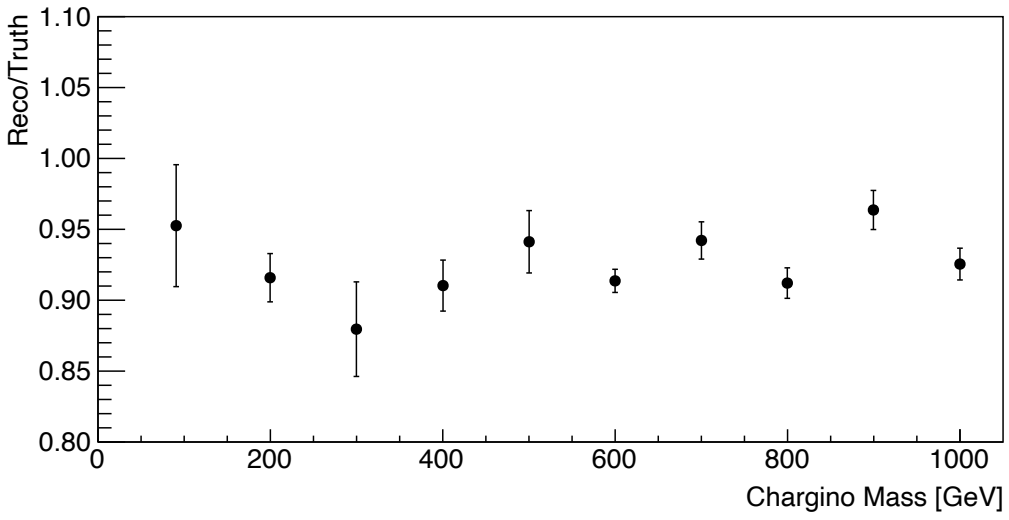

Figure 109: Chargino mass dependence of the mass reconstruction.

Finally, a precision of chargino mass measurement with limited statistics is estimated. Figure 110 shows the distribution of estimated chargino mass for each measurement. Each color shows the number of events used to estimate chargino mass and each entry means the result of each measurement with corresponding statistics. From this result, the probability that the measured mass is within 100 GeV of the truth chargino mass is more than 90% with 5 events, i.e. 10 entries of tracks. The expected number of signal events for 600 GeV chargino is 5 (116) events at $\tau_{\tilde{\chi}_1^\pm}$ = 0.2 ns ($\tau_{\tilde{\chi}_1^\pm}$ = 1.0 ns), and for 1000 GeV chargino is 0.4 (9) events at $\tau_{\tilde{\chi}_1^\pm}$ = 0.2 ns ($\tau_{\tilde{\chi}_1^\pm}$ = 1.0 ns) with an integrated luminosity of 3000 fb^{-1} in Run-2 environment. Since this method requires two disappearing tracks, the improvement in track reconstruction efficiency works as a square. Therefore, if the track efficiency becomes twice, the overall event selection efficiency improves by a factor of 4. For example, it can be achieved by using 3-layer tracks in the current detector geometry. Since this chargino mass reconstruction method is independent of track length, it even works for 2-layer tracks. By using 2-layer tracks, the track efficiency improves 4 times, so the number of events with two disappearing tracks increases 16 times. However, the second innermost layer of the HL-LHC inner tracker is aligned at R $\simeq$ 100 mm. It is very far compared to the current second innermost layer of R = 50.5 mm. Therefore, once the long-lived chargino is discovered, it is important to implement an inner layer to increase statistics for the mass measurement.

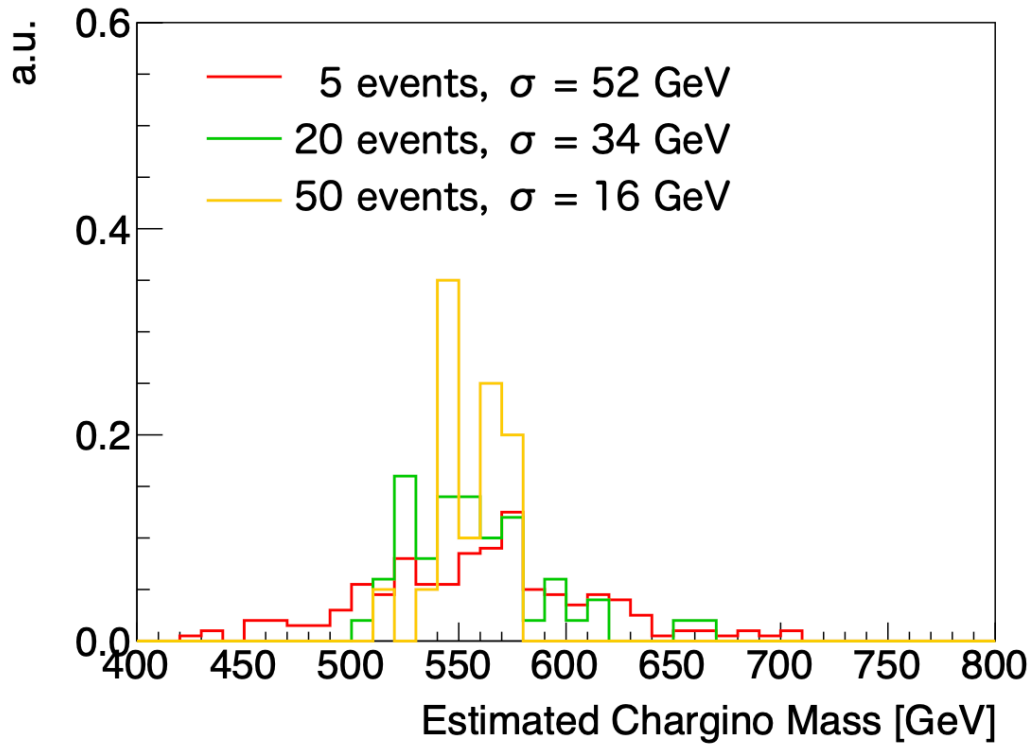

Figure 110: Expected precision of chargino mass measurement with certain statistics. Each color shows the number of events used to estimate chargino mass. The σ is the RMS value of each histogram.

8 Conclusions

This thesis presented the search results for long-lived charginos by using a disappearing track comprising four-pixel layer hits in pp collisions at $\sqrt{s}$ = 13 TeV with the full Run-2 ATLAS data. An important compressed mass region of the electroweak SUSY can be explored by using a disappearing track object. The search was performed for the pure-wino and -higgsino LSP scenarios in the electroweak channel and for the pure-wino LSP scenario in the strong channel. Thanks to the calorimeter veto, the background events can be reduced to a few events. No significant excess was found above the background predictions in both channels; hence, the new exclusion limits at 95% CL were calculated for each signal model. The observed limit in the electroweak channel excluded chargino masses up to 660 GeV on the theoretical prediction line for the pure-wino LSP scenario and 210 GeV for the pure-higgsino LSP scenario. The maximum reach in the strong channel was 1.4 (1.8 TeV) and 2.1 (2.18 TeV) TeV on the chargino and gluino masses, respectively, with $\tau_{\tilde{\chi}_1^\pm}$ = 0.2 ns (1.0 ns).

Compared to the previous analysis, sensitivity was improved by a factor of 5 in the signal production cross-section. The wino search result in the electroweak channel showed better sensitivity than the CMS full Run-2 result in the short-lifetime region. By contrast, worse sensitivity was observed in the long-lifetime region. As regards the higgsino search, only this analysis can explore the pure-higgsino prediction region in the ATLAS experiment. For the wino search in the strong channel, this analysis exhibited a better sensitivity than the inclusive search for the strong SUSY in the diagonal region, where the mass difference between the gluino and LSP masses was low.

Future disappearing track searches can employ several ideas to improve the sensitivity. By using various track lengths, the chargino mass reach is expected to improve to more than 100 GeV, even with the same dataset. Once the long-lived chargino is discovered, its mass might be reconstructed from $\mathrm{d}E/\mathrm{d}x$ and momentum. A sufficient momentum resolution for the chargino mass measurement is obtained by requiring two disappearing tracks and by calculating the momentum using collinear approximation. The chargino mass is expected to be measured within 100 GeV from the truth value with five events.

Acknowledgment

Finishing my Ph.D. thesis took time. Therefore, I am happy to be able to tell everyone about its completion. I am grateful to those who have helped me in my endeavor.

My greatest appreciation goes to Prof. Kohei Yorita, my supervisor. From him, I learned that all people are equal under this universe, and that the door of the quest for truth is open to everyone. He always shows me the ways of a physicist. I hope this thesis would return the favor for his support of over 11 years.

Next, I appreciate the reviewers of my Ph.D. thesis. Prof. Sachio Komamiya devoted his precious time to reading my draft and helping me improve the quality of my paper. Prof. Hiroyuki Abe gave me helpful advice from the theoretical aspect. Assoc. Prof. Ryu Sawada served as both a reviewer and a co-researcher of the analysis. He managed our analysis group and worked hard to publish our results.

My gratitude also goes to the members of the disappearing track team. Prof. Matthew Gignac and Dr. Masahiro Morinaga helped me prepare the necessary documents and clarify the publication requirements. Dr. Masahiko Saito gave me technical advice as a previous analyzer. James Smith helped me prepare reinterpretation materials, while Daiya Akiyama helped me create event displays.

I appreciate the FTK offline software team, especially Assoc. Prof. Jahred Adelman, Assoc. Prof. Stefan Schmitt, Dr. Daniel Britzger, and Dr. Tomoya Iizawa. The FTK termination was a bad news for us, but I will never forget our success in preparing the constants and patterns for real data collection. Dr. John Baines, who was working on the FTK online software, also worked hard to integrate FTK into the HLT.

Thank you to my officemates and housemates during my CERN stay. Naoki Kimura, Takashi Mitani, Tomoya Iizawa, Tatsumi Nitta, Stefan Guindon, Ryosuke Fuchi, Midori Fuchi, Kota Kasahara, and Masahiro Morinaga helped me achieve a fulfilling life at CERN.

My experience from the ANKOK experiment is irreplaceable. My physics life started with Assoc. Prof. Masashi Tanaka, who showed me how to efficiently proceed with studies from many aspects. I realized the importance of his guidance after moving to the ATLAS. I spent most of my time with Dr. Washimi Tatsuki and Masaki Kawamura. We worked hard, but it was an enjoyable time. My gratitude also goes to the Kohei Yorita Laboratory members, from whom I learned many things. Thank you for the shared experiences and knowledge. Secretary Mrs. Atsuko Sakamoto kindly supported me in many aspects. She is like a local oasis in the desert.

Finally, I would like to express my gratitude to my parents, Tadashi and Ryoko. They must have been worried but still let me do what I wanted to do.

References

[1] N. Aghanim et al., *Planck 2018 results*, Astronomy & Astrophysics **641** (2020) A6, ISSN: 1432-0746, URL: http://dx.doi.org/10.1051/0004-6361/201833910.

[2] C. MissMJ, *Standard Model of Elementary Particles*, (2019), http://en.wikipedia.org/wiki/File:Standard_Model_of_Elementary_Particles.svg.

[3] M. Tanabashi et al., *Review of Particle Physics*, Phys. Rev. D **98** (3 2018) 030001, URL: https://link.aps.org/doi/10.1103/PhysRevD.98.030001.

[4] S. P. MARTIN, "A SUPERSYMMETRY PRIMER," *Perspectives on Supersymmetry*, WORLD SCIENTIFIC, 1998 1, URL: https://doi.org/10.1142%2F9789812839657_0001.

[5] W. Beenakker et al., *Production of Charginos, Neutralinos, and Sleptons at Hadron Colliders*, Phys. Rev. Lett. **83** (19 1999) 3780, URL: https://link.aps.org/doi/10.1103/PhysRevLett.83.3780.

[6] G. Bozzi, B. Fuks, and M. Klasen, *Threshold resummation for slepton-pair production at hadron colliders*, Nuclear Physics B **777** (2007) 157, URL: https://doi.org/10.1016%2Fj.nuclphysb.2007.03.052.

[7] J. Debove, B. Fuks, and M. Klasen, *Threshold resummation for gaugino pair production at hadron colliders*, Nuclear Physics B **842** (2011) 51, URL: https://doi.org/10.1016%2Fj.nuclphysb.2010.08.016.

[8] B. Fuks, M. Klasen, D. R. Lamprea, and M. Rothering, *Gaugino production in proton-proton collisions at a center-of-mass energy of 8 TeV*, JHEP **10** (2012) 081, arXiv: 1207.2159 [hep-ph].

[9] B. Fuks, M. Klasen, D. R. Lamprea, and M. Rothering, *Precision predictions for electroweak superpartner production at hadron colliders with* Resummino, Eur. Phys. J. C **73** (2013) 2480, arXiv: 1304.0790 [hep-ph].

[10] B. Fuks, M. Klasen, D. R. Lamprea, and M. Rothering, *Revisiting slepton pair production at the Large Hadron Collider*, Journal of High Energy Physics **2014** (2014) 168, URL: https://doi.org/10.1007/JHEP01(2014)168.

[11] J. Fiaschi and M. Klasen,
Slepton pair production at the LHC in NLO+NLL with resummation-improved parton densities,
Journal of High Energy Physics **2018** (2018),
URL: https://doi.org/10.1007%2Fjhep03%282018%29094.

[12] J. Fiaschi and M. Klasen, *Neutralino-chargino pair production at NLO+NLL with resummation-improved parton density functions for LHC Run II*, Physical Review D **98** (2018),
URL: https://doi.org/10.1103%2Fphysrevd.98.055014.

[13] ATLAS Collaboration, *SUSY March 2022 Summary Plot Update*,
ATL-PHYS-PUB-2022-013 (2022), URL: https://atlas.web.cern.ch/Atlas/GROUPS/PHYSICS/PUBNOTES/ATL-PHYS-PUB-2022-013/.

[14] A. Arbey, M. Boudaud, F. Mahmoudi, and G. Robbins,
Robustness of dark matter constraints and interplay with collider searches for New Physics,
Journal of High Energy Physics **2017** (2017),
URL: https://doi.org/10.1007%2Fjhep11%282017%29132.

[15] M. Ibe, S. Matsumoto, and R. Sato,
Mass splitting between charged and neutral winos at two-loop level,
Physics Letters B **721** (2013) 252,
URL: https://doi.org/10.1016%2Fj.physletb.2013.03.015.

[16] C.-H. Chen, M. Drees, and J. F. Gunion, *Erratum: Nonstandard string-SUSY scenario and its phenomenological implications [Phys. Rev. D 55, 330 (1997)]*,
Phys. Rev. D **60** (3 1999) 039901,
URL: https://link.aps.org/doi/10.1103/PhysRevD.60.039901.

[17] ATLAS Collaboration, *Search for long-lived charginos based on a disappearing-track signature in pp collisions at* $\sqrt{s}$ = 13 *TeV with the ATLAS detector*, JHEP **06** (2018) 022,
arXiv: 1712.02118 [hep-ex].

[18] N. Nagata and S. Shirai, *Higgsino dark matter in high-scale supersymmetry*,
Journal of High Energy Physics **2015** (2015),
URL: https://doi.org/10.1007%2Fjhep01%282015%29029.

[19] ATLAS Collaboration, *SUSY May 2020 Summary Plot Update*,
ATL-PHYS-PUB-2020-013 (2020), URL: https://atlas.web.cern.ch/Atlas/GROUPS/PHYSICS/PUBNOTES/ATL-PHYS-PUB-2020-013/.

[20] J. T. Boyd, *LHC Run-2 and Future Prospects*, (2020),
URL: https://arxiv.org/abs/2001.04370.

[21] ATLAS Collaboration, *The ATLAS Experiment at the CERN Large Hadron Collider*, JINST **3** (2008) S08003.

[22] ATLAS Outreach, *ATLAS Fact Sheet : To raise awareness of the ATLAS detector and collaboration on the LHC*, ATLAS Brochures (2010), URL: https://cds.cern.ch/record/1457044.

[23] ATLAS Collaboration, *The ATLAS Experiment at the CERN Large Hadron Collider*, JINST **3** (2008) S08003. 437 p, Also published by CERN Geneva in 2010, URL: https://cds.cern.ch/record/1129811.

[24] S. van der Meer, *Calibration of the effective beam height in the ISR*, CERN-ISR-PO-68-31 (1968), URL: https://cds.cern.ch/record/296752.

[25] ATLAS Collaboration, *Study of the material of the ATLAS inner detector for Run 2 of the LHC*, JINST **12** (2017) P12009, URL: https://atlas.web.cern.ch/Atlas/GROUPS/PHYSICS/PAPERS/PERF-2015-07/.

[26] J. Weingarten, "System Test and Noise Performance Studies at The ATLAS Pixel Detector," Presented on 19 Sep 2007, 2007, URL: http://cds.cern.ch/record/1099748.

[27] ATLAS Collaboration, *Jet energy resolution in 2017 data and simulation*, JETM-2018-005, 2018, URL: https://atlas.web.cern.ch/Atlas/GROUPS/PHYSICS/PLOTS/JETM-2018-005/.

[28] ATLAS Collaboration, *Topological cell clustering in the ATLAS calorimeters and its performance in LHC Run 1*, The European Physical Journal C **77** (2017), URL: https://doi.org/10.1140%2Fepjc%2Fs10052-017-5004-5.

[29] S. M. Shaw and A. Collaboration, *The Run-2 ATLAS Trigger System*, (2016), URL: https://cds.cern.ch/record/2127944.

[30] M. Elsing, L. Goossens, A. Nairz, and G. Negri, **219** (2010) 072011, URL: https://doi.org/10.1088/1742-6596/219/7/072011.

[31] ATLAS Collaboration, *Public ATLAS Luminosity Results for Run-2 of the LHC*, URL: https://twiki.cern.ch/twiki/bin/view/AtlasPublic/LuminosityPublicResultsRun2.

[32] ATLAS Offline Software, *ATLAS Software Documentation*, URL: https://atlassoftwaredocs.web.cern.ch/.

[33] T. Cornelissen, M. Elsing, I. Gavrilenko, W. Liebig, E. Moyse, and A. Salzburger, *The new ATLAS track reconstruction (NEWT)*, Journal of Physics: Conference Series **119** (2008) 032014, URL: https://dx.doi.org/10.1088/1742-6596/119/3/032014.

[34] M. Cacciari, G. P. Salam, and G. Soyez, *The anti-k_t jet clustering algorithm*, JHEP **04** (2008) 063, arXiv: 0802.1189 [hep-ph].

[35] W. Lampl et al., *Calorimeter Clustering Algorithms: Description and Performance*, ATL-LARG-PUB-2008-002 (2008), URL: http://cds.cern.ch/record/1099735.

[36] ATLAS Collaboration, *Jet energy measurement with the ATLAS detector in proton-proton collisions at $\sqrt{s} = 7$ TeV*, The European Physical Journal C **73** (2013), arXiv: 1112.6426 [hep-ex], URL: https://doi.org/10.1140%2Fepjc%2Fs10052-013-2304-2.

[37] ATLAS Collaboration, *Measurement of the Transverse Momentum Distribution of W Bosons in pp Collisions at $\sqrt{s} = 7$ TeV with the ATLAS Detector*, Physical Review D **85** (2012) 012005, arXiv: 1108.6308 [hep-ex], URL: https://doi.org/10.1103%2Fphysrevd.85.012005.

[38] ATLAS Collaboration, *Muon reconstruction and identification efficiency in ATLAS using the full Run 2 pp collision data set at $\sqrt{s} = 13$ TeV*, The European Physical Journal C **81** (2021) 578, URL: https://doi.org/10.1140/epjc/s10052-021-09233-2.

[39] ATLAS Collaboration, *Electron reconstruction and identification in the ATLAS experiment using the 2015 and 2016 LHC proton-proton collision data at $\sqrt{s} = 13$ TeV*, The European Physical Journal C **79** (2019), URL: https://doi.org/10.1140%2Fepjc%2Fs10052-019-7140-6.

[40] ATLAS Collaboration, *ATLAS data quality operations and performance for 2015–2018 data-taking*, Journal of Instrumentation **15** (2020) P04003, URL: https://dx.doi.org/10.1088/1748-0221/15/04/P04003.

[41] S. Das, *A simple alternative to the Crystal Ball function*, 2016, arXiv: 1603.08591 [hep-ex].

[42] F. James and M. Winkler, *MINUIT User's Guide*, (2004), URL: http://seal.web.cern.ch/seal/documents/minuit/mnusersguide.pdf.

[43] W. Verkerke and D. Kirkby, *The RooFit toolkit for data modeling*, 2003, arXiv: physics/0306116 [physics.data-an].

[44] J. Pumplin et al., *New generation of parton distributions with uncertainties from global QCD analysis*, JHEP **07** (2002) 012, arXiv: hep-ph/0201195.

[45] A. D. Martin, W. J. Stirling, R. S. Thorne, and G. Wat, *Parton distributions for the LHC*, Eur. Phys. J. C **63** (2009) 189, arXiv: 0901.0002 [hep-ph].

[46] ATLAS Collaboration, *Jet energy scale and resolution measured in proton–proton collisions at $\sqrt{s}$ = 13 TeV with the ATLAS detector*, Eur. Phys. J. C **81** (2020) 689, arXiv: 2007.02645 [hep-ex].

[47] ATLAS Collaboration, *Search for long-lived charginos based on a disappearing-track signature in pp collisions at $\sqrt{s}$ = 13 TeV with the ATLAS detector*, (2017), arXiv: 1712.02118 [hep-ex].

[48] ATLAS Collaboration, *Search for charginos nearly mass degenerate with the lightest neutralino based on a disappearing-track signature in pp collisions at $\sqrt{s}$ = 8 TeV with the ATLAS detector*, Phys. Rev. D **88** (2013) 112006, arXiv: 1310.3675 [hep-ex].

[49] ATLAS Collaboration, *Search for direct pair production of higgsinos by reinterpretation of the disappearing track analysis with 36.1 fb^{-1} of $\sqrt{s}$ = 13 TeV data collected with the ATLAS experiment*, ATL-PHYS-PUB-2017-019, 2017, URL: https://atlas.web.cern.ch/Atlas/GROUPS/PHYSICS/PUBNOTES/ATL-PHYS-PUB-2017-019/.

[50] CMS Collaboration, *Search for disappearing tracks in proton-proton collisions at $\sqrt{s}$ = 13 TeV*, Physics Letters B **806** (2020) 135502, ISSN: 0370-2693, URL: https://www.sciencedirect.com/science/article/pii/S0370269320303063.

[51] CMS Collaboration, *Search for disappearing tracks in proton-proton collisions at $\sqrt{s}$ = 13 TeV*, HEPData (collection), https://doi.org/10.17182/hepdata.95354, 2021.

[52] ATLAS Collaboration, *SUSY Summary Plots March 2022*, tech. rep., All figures including auxiliary figures are available at https://atlas.web.cern.ch/Atlas/GROUPS/PHYSICS/PUBNOTES/ATL-PHYS-PUB-2022-013: CERN, 2022, URL: http://cds.cern.ch/record/2805985.

[53] ATLAS Collaboration, *Search for squarks and gluinos in final states with jets and missing transverse momentum using 139 fb^{-1} $\sqrt{s}$ = 13 TeV pp collision data with the ATLAS detector*, Journal of High Energy Physics **2021** (2021) 143, URL: https://doi.org/10.1007/JHEP02(2021)143.

[54] CMS Collaboration, *Searches for physics beyond the standard model with the M_{T2} variable in hadronic final states with and without disappearing tracks in proton–proton collisions at $\sqrt{s}$ = 13 TeV*,

The European Physical Journal C **80** (2020) 3,
URL: https://doi.org/10.1140/epjc/s10052-019-7493-x.

[55] ATLAS Collaboration, *High Level Trigger Run-3 Disappearing Track Trigger Performance*, URL: https://twiki.cern.ch/twiki/bin/view/AtlasPublic/HLTTrackingPublicResults.

[56] ATLAS Collaboration, *Performance of tracking and vertexing techniques for a disappearing track plus soft track signature with the ATLAS detector*, tech. rep., All figures including auxiliary figures are available at https://atlas.web.cern.ch/Atlas/GROUPS/PHYSICS/PUBNOTES/ATL-PHYS-PUB-2019-011: CERN, 2019, URL: http://cds.cern.ch/record/2669015.

[57] ATLAS Collaboration, *dE/dx measurement in the ATLAS Pixel Detector and its use for particle identification*, tech. rep., All figures including auxiliary figures are available at https://atlas.web.cern.ch/Atlas/GROUPS/PHYSICS/CONFNOTES/ATLAS-CONF-2011-016: CERN, 2011, URL: https://cds.cern.ch/record/1336519.

[58] S. Asai et al., *Studying gaugino masses in supersymmetric model at future 100 TeV pp collider*, Journal of High Energy Physics **2019** (2019) 179,
URL: https://doi.org/10.1007/JHEP05(2019)179.

[59] ATLAS Collaboration, *Search for heavy charged long-lived particles in proton-proton collisions at $\sqrt{s} = 13$ TeV using an ionisation measurement with the ATLAS detector*, Physics Letters B **788** (2019) 96,
URL: https://doi.org/10.1016%2Fj.physletb.2018.10.055.

Appendices

A Validation of Using Wino Samples for the Higgsino Search

Wino samples are validated by comparing CLs values between two conditions at 200 GeV mass point. One is expected from 200 GeV wino samples and another one is estimated by interpolation between 160 GeV and 240 GeV higgsino samples. Results are summarized in Table 22. The difference between them is too small so the wino samples are available for the higgsino sensitivity calculation.

	Lifetime	
	0.03 ns	0.04 ns
Estimated from wino	0.184	0.005
Higgsino interpolation	0.203	0.007

Table 22: CLs-value for 200 GeV higgsino

B Validation of Lifetime Reweighting

Lifetime reweighting method is validated by using ($m_{\tilde{g}} = 1400\text{GeV}, m_{\tilde{\chi}_1^\pm} = 1100\text{GeV}$) sample in the strong channel. Table 23 shows the cut-flow. First column is number of events with 0.2 ns signal sample. And second column is number of events for 0.2 ns from 1.0 ns signal sample by using lifetime reweighting. These numbers are good agreement within MC statistic errors.

Requirement	0.2 ns sample	Lifetime reweighted from 1.0 ns sample
All events	3498.3 ± 23.9	3506.9 ± 23.85
Trigger	3161.5 ± 22.3	3177.1 ± 22.29
Lepton VETO	3148.1 ± 22.2	3164.6 ± 22.25
$E_{\mathrm{T}}^{\mathrm{miss}} > 250$ GeV	1823.9 ± 17.3	1852.3 ± 17.38
1st jet $p_{\mathrm{T}} > 100$ GeV	1820.0 ± 17.3	1847.6 ± 17.36
2nd jet $p_{\mathrm{T}} > 20$ GeV	1819.9 ± 17.3	1847.3 ± 17.36
3rd jet $p_{\mathrm{T}} > 20$ GeV	1804.9 ± 17.2	1833.9 ± 17.31
$\Delta\phi_{\mathrm{min}}^{\mathrm{jet-E_T^{miss}}} > 0.4$	1558.4 ± 15.9	1578.2 ± 15.99
Pixel-Track	31.3 ± 2.0	32.8 ± 2.65
Quality cut	30.5 ± 2.0	30.0 ± 2.07
Isolation cut	22.0 ± 1.7	23.2 ± 1.88
Geometrical cut	19.8 ± 1.6	21.4 ± 1.79
Calo-veto	19.8 ± 1.6	21.4 ± 1.79
$p_{\mathrm{T}} > 60$ GeV	14.8 ± 1.2	16.0 ± 1.34

Table 23: Summary of kinematic and tracklet selection cuts for the strong production for signal sample normalized to 136 fb^{-1}.

C Signal Extraction Test

To validate the fitting procedure with signal excess, pseudo datasets are generated based on each BG component and signal. A number of produced events fluctuates to a Poisson distribution. Real data is used for each CRs to obtain background templates. Figure 111 shows the result of signal extraction test with signal at 700 GeV chargino mass. 100 trials are performed for each mu value, the signal strength. The signal is successfully extracted for each mu value.

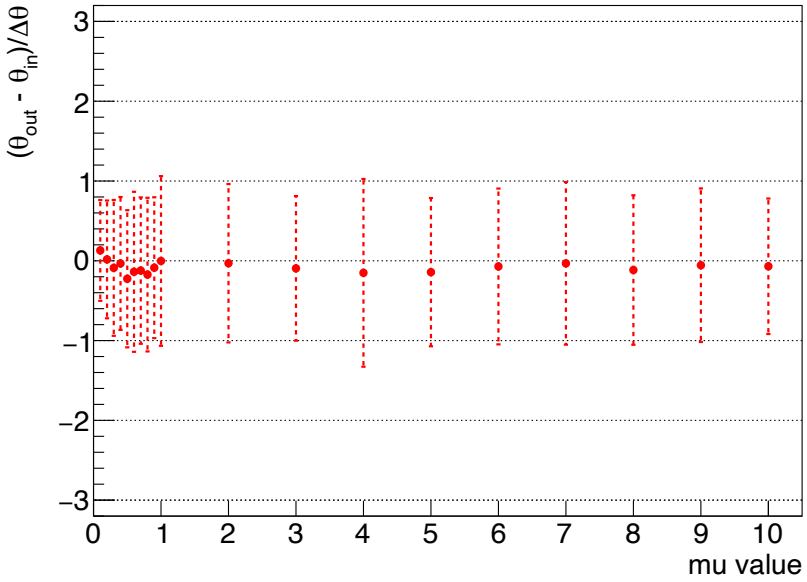

Figure 111: The impact of nuisance parameters on signal strength

D Properties of Fake Background

Several properties of the fake background are scrutinized for validation purposes.

D.1 $E_{\mathrm{T}}^{\mathrm{miss}}$ Dependence

Since a normalization of the fake-tracklet background is determined using low/middle-$E_{\mathrm{T}}^{\mathrm{miss}}$ control region, it is important to check the fake-tracklet p_{T} shape in several $E_{\mathrm{T}}^{\mathrm{miss}}$ regions. Figure 112 shows a comparison of the tracklet p_{T} shape of the fake background for each $E_{\mathrm{T}}^{\mathrm{miss}}$ regions. In the left figure, $E_{\mathrm{T}}^{\mathrm{miss}}$ region is divided into three to have enough statistics for each regions. In the right figure, $E_{\mathrm{T}}^{\mathrm{miss}}$ region is divided into four regions, i.e. very low-$E_{\mathrm{T}}^{\mathrm{miss}}$, low-$E_{\mathrm{T}}^{\mathrm{miss}}$, middle-$E_{\mathrm{T}}^{\mathrm{miss}}$ and high-$E_{\mathrm{T}}^{\mathrm{miss}}$ regions. The nominal p_{T} shape used in the signal region is shown in the blue broken line and p_{T} shapes of each $E_{\mathrm{T}}^{\mathrm{miss}}$ regions are shown in colored points. The center of x-value is a little bit shifted intentionally to make it easier to see error bars for each categories. The statistical error is a big in high-$E_{\mathrm{T}}^{\mathrm{miss}}$ region due to a lack of statistics, there is a 2155 events in very low-$E_{\mathrm{T}}^{\mathrm{miss}}$ region while high-$E_{\mathrm{T}}^{\mathrm{miss}}$ region has only 69 events. It looks that there is no clear dependency.

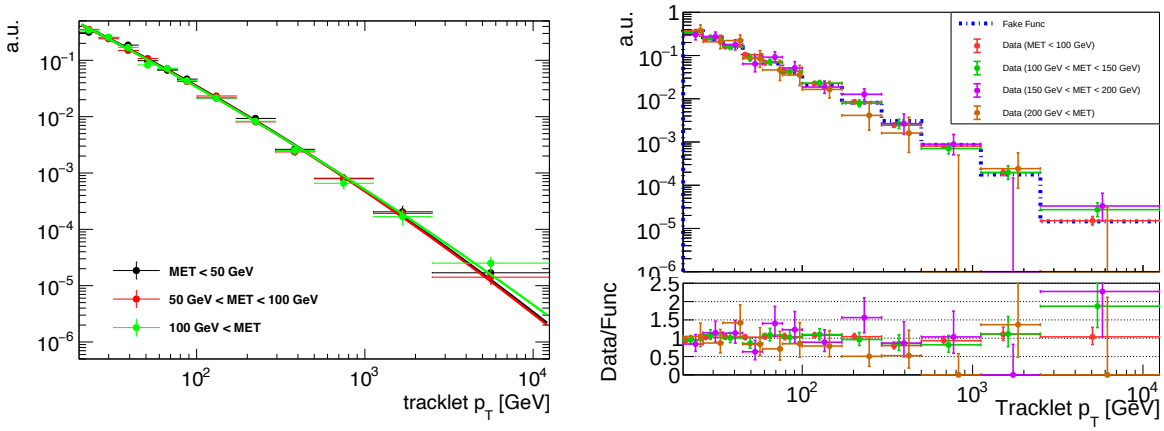

(a) (b)

Figure 112: The fake-tracklet background shapes in each $E_{\mathrm{T}}^{\mathrm{miss}}$ region

D.2 d_0 Dependence

In order to know the order of the impact by a possible fake-BG-shape dependence on the d0-significance, the fake p_{T} spectrum is estimated by using the d0-significance sideband region ($3 < d_0$ sig < 10) instead of the fake CR. Figure 113 shows the fake shape in different d_0 significance regions. The shape in the

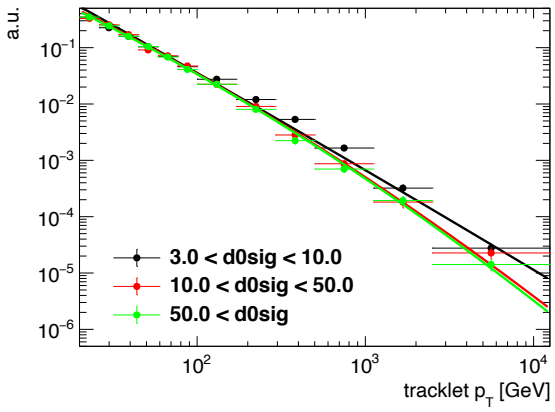

Figure 113: The d0-significance dependence of the fake BG shapes

sideband is clearly different because of non-fake components. Nevertheless, the conservative impact of the possible uncertainty in the fake-shape was calculated using the fit on the Asimov data where the signal μ=1 was assumed. The best-fit signal strength was changed by only $\Delta\mu = 0.03$ due to the difference in the fake-shape in the sideband and that in the fake CR. Since this impact is much smaller than other fake-related systematic uncertainties, this uncertainty can be ignored.

D.3 Pile-Up Dependence

Since the fake-tracklet is originating from mis-combination of hits from low-p_{T} track, which might be dominated by pile-up tracks, there might be a dependency against pile-up condition. Figure 114 shows a comparison of the fake-tracklet p_{T} shape between three $\langle\mu\rangle$ events. It looks there is no clear dependency among each pile-up events.

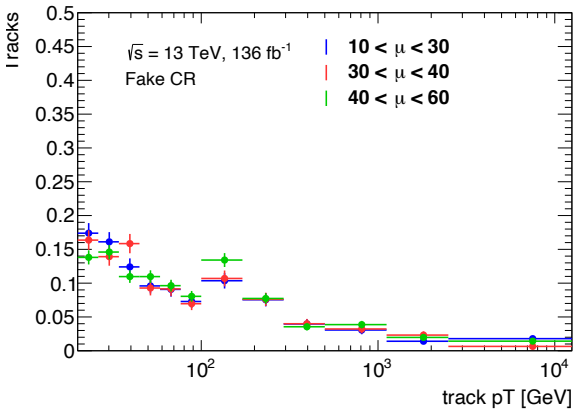

Figure 114: The pileup dependence of the fake BG shapes

Besides on pile-up dependency, a condition of the inner detector could be a source of dependency for the fake-tracklet background. Also the normalization of the fake-tracklet background is estimated by using an assumption of a ratio of high-$E_{\mathrm{T}}^{\mathrm{miss}}$ to low-$E_{\mathrm{T}}^{\mathrm{miss}}$ region, it is important to check this ratio as a function of pile-up and data taking period. Figure 115(a) and (b) shows a ratio of the number of events in high-$E_{\mathrm{T}}^{\mathrm{miss}}$ to low-$E_{\mathrm{T}}^{\mathrm{miss}}$ as a function of pile-up and data taking period respectively. There is no dependency against both pile-up condition and data taking period.

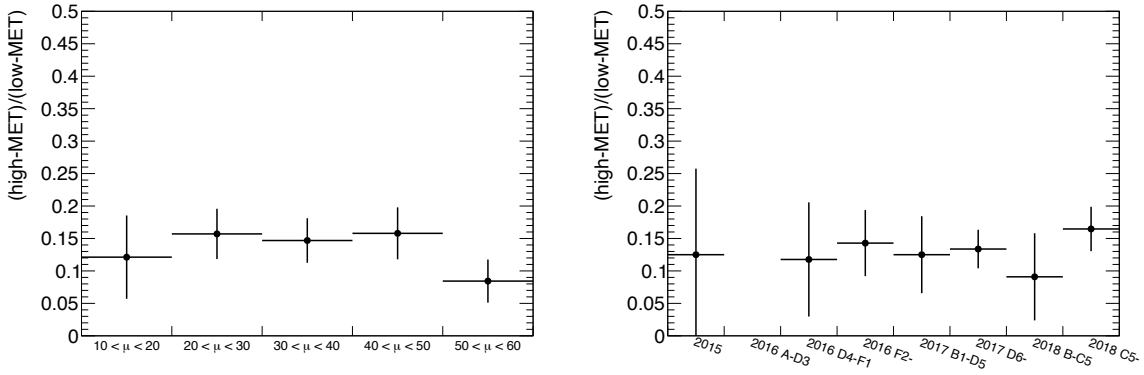

(a) As a function of pileup

(b) As a function of data taking period

Figure 115: The (high-$E_{\mathrm{T}}^{\mathrm{miss}}$)/(low-$E_{\mathrm{T}}^{\mathrm{miss}}$) ratio of fake-tracklet background

D.4 Parametrization of Fake Function

Originally, the parameters of the fake function p_0 and p_1 had an almost -100% correlation. So the new parametrization which do not correlate with each other is introduced.

Figure 116 shows a chi-square map of the fitting result of fake CR with fixed p_0 and p_1 values. Small chi-square values are distributed in linear, so the correlation can be suppressed by rotating parametrization. The rotated parameters can be defined in the following formula.

$$p_0 = p_0' \cos\theta - p_1' \sin\theta \tag{32}$$

$$p_1 = p_0' \sin\theta + p_1' \cos\theta \tag{33}$$

Figure 117 shows the correlation value as a function of rotation angle θ. As shown in Figure 88, the p_0 and p_1 are independent with rotated parametrization θ at -0.0973. The expected number of BG does not change with this modification. The impact of systematics on signal strength $\Delta\mu$ is calculated by using Asimov data, and it is less than 0.002.

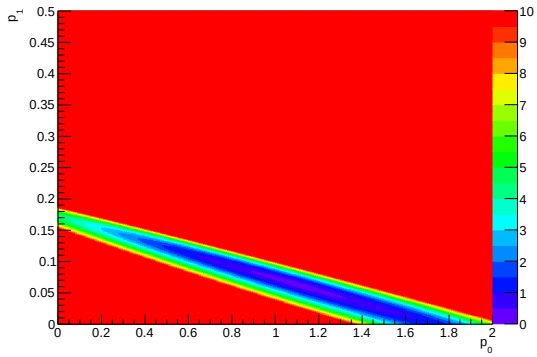

Figure 116: The chi-square map with fixed p0 and p1 values

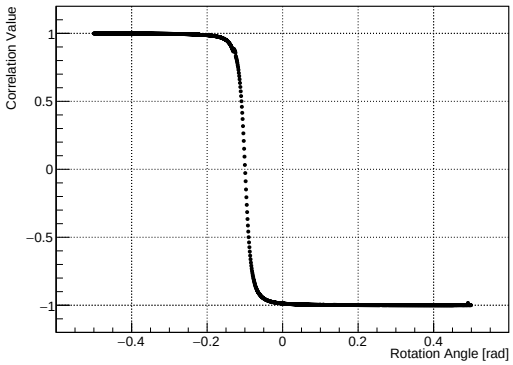

Figure 117: Correlation value vs rotation angle